Macrodiversity and Multiuser Detection: High Performance Tools in a DS-CDMA System

by

Lisa Welburn

M.Sc., University of Calgary, 1994

B.Sc., University of Calgary, 1992

A THESIS SUBMITTED IN PARTIAL FULFILLMENT
OF THE REQUIREMENTS FOR THE DEGREE OF
DOCTOR OF PHILOSOPHY
in the School
of
Engineering Science

SIMON FRASER UNIVERSITY
May 2001

APPROVAL

Name: Lisa Welburn

Degree: Doctor of Philosophy

Title of thesis: Macrodiversity and Multiuser Detection: High Performance Tools in a DS-CDMA System

Examining Committee: Dr. Mehrdad Saif
Chair

Dr. James K. Cavers, Senior Supervisor

Dr. Kevin W. Sowerby, Supervisor
Professor, University of Auckland, New Zealand

Dr. Jacques Vaisey, Supervisor

Dr. Ljiljana Trajkovic, Supervisor

Dr. Steve Hardy, Internal Examiner

Dr. David Brady, External Examiner
Professor, Northeastern University, Boston, MA

Date Approved: _____

Abstract

Macrodiversity, which involves the joint use of antennas at different base stations, has the ability to improve both the forward link and the reverse link performance of a wireless mobile communications system. When macrodiversity is combined with multiuser detection, the results are exceptionally promising. This thesis contains two main investigations. The first develops a multiuser-macrodiversity detector to be used within a group of base stations for improving reverse link performance, and the second regards a forward link power optimization of macrodiversity antennas.

The first investigation is a performance analysis for the reverse link of a wireless direct sequence code division multiple access (DS-CDMA) system that exploits macrodiversity reception while adopting the maximum likelihood (ML) multiuser detector for the basic detection. It appears to be the first analytical treatment of the ML multiuser-macrodiversity detector in Rayleigh fading channels. The analysis includes the effects of frequency selective fading, imperfect synchronization, and imperfect channel state information (CSI). In addition to the performance analysis, the thesis presents the Conditional Metric Merge (CMM) algorithm, which keeps the computational complexity of the ML multiuser-macrodiversity detector at a minimum. The CMM algorithm is a new algorithm and is the first of its kind as multiuser-macrodiversity detection is a new area of research. It is shown that the ML multiuser-macrodiversity detector is capable of reducing the bit error rate (BER) for many users by several orders of magnitude compared with multiuser detectors that operate on each antenna separately. This investigation is performed only for the reverse link, as the high computational complexity of multiuser detectors makes them most suitable for use at the base stations.

The second investigation optimizes the transmit power of macrodiversity antennas in an indoor DS-CDMA system. The results show that the power optimization significantly

increases forward link capacity. The treatment includes a global optimization strategy that allocates power at the various macrodiversity antennas so that the average of all users' BERs is minimized. In practice, the complexity of this global optimization problem is reduced as many of the links are extremely weak and can be removed from the optimization. Simulation results demonstrate that, when compared to traditional soft handoff power allocation, the optimization algorithm increases the forward link capacity for a given quality of service by 10-20%.

This thesis also includes other results that are of a secondary nature, but are nevertheless both novel and useful.

Acknowledgements

I wish to thank my senior supervisor, Dr. Jim Cavers, for his guidance and support throughout the course of this work. I consistently found my weekly meetings with Jim to be both informative and enlightening. During this degree, I learned far more than I previously thought possible as a direct result of having Jim as my senior supervisor.

I would also like to thank my co-supervisor, Dr. Kevin Sowerby, for his many helpful comments and suggestions regarding the research.

Financial support was provided by the Natural Sciences and Engineering Research Council of Canada (NSERC) and TELUS Mobility. This support was greatly appreciated.

Dedication

To my husband, Craig, for all of his love, support, and encouragement throughout our years together.

Contents

List of Tables

List of Figures

List of Abbreviations

AME	Asymptotic multiuser efficiency
AWGN	Additive white Gaussian noise
BER	Bit error rate
BPSK	Binary phase shift keying
CCI	Cochannel interference
CDMA	Code division multiple access
CMM	Conditional Metric Merge
CSI	Channel state information
dB	Decibel
DS	Direct sequence
FAF	Floor attenuation factor
FDMA	Frequency division multiple access
IC	Interference cancellation
IIR	Infinite impulse response
ILT	Inverse Laplace transform
ISI	Intersymbol interference
JD	Joint detection
LP	Left plane
MAI	Multiple access interference
MDM	Multiply-Detected Macrodiversity
ML	Maximum likelihood
MMSE	Minimum mean square error
MUMD	Multiuser-macrodiversity detection
PCS	Personal communication system
PIC	Parallel interference cancellation

PDF	Probability density function
PDP	Power delay profile
PN	Pseudonoise
PSAM	Pilot Symbol Assisted Modulation
QoS	Quality of service
RP	Right plane
SIC	Successive interference cancellation
SINR	Signal to interference and noise ratio
SNR	Signal to noise ratio
TDMA	Time division multiple access
TOA	Time of arrival
WSSUS	Wide sense stationary uncorrelated scattering

List of Symbols

A_k	User k's amplitude factor
$\mathcal{A}$	Active set
$b_k(n)$	The n^{th} BPSK information symbol of the k^{th} user
$\mathbf{b}$	Vector of information symbols
$\mathbf{B}_{\psi_l}$	Matrix of information symbols for the users in ψ_l
$c_{lkg}(n)$	Complex Gaussian channel gain for antenna l, user k, and path g
$\mathbf{c}_{\psi_l}$	Vector of complex Gaussian channel gains for the users in ψ_l
d_{ij}	Decision variable used in the detection scheme
$D(\mathbf{h})$	The CMM algorithm's tentative decisions
$D(\Gamma)$	Equivalent order of diversity for downlink optimization
$e_{lkg}(n)$	Channel estimation error for antenna l, user k, and path g
$\mathbf{E}_{\psi_l}$	The error sequence matrix for the users in ψ_l
f_D	Doppler spread
$\mathbf{f}$	Previously combined metrics in the CMM algorithm
$\mathbf{F}_{ij,l}$	Matrix of the quadratic form
g	An index variable which references the channel path
G	The number of resolvable channel paths is $G+1$
h	The index variable for the CMM algorithm
I_{ol}	An estimate of the interference power at antenna l
I_w	The relevant indices in $\Psi(\mathbf{h})$ of the elements in $\Psi(\mathbf{h}) - \Psi(w)$
J_o	Zeroth order Bessel function of the first kind
k	An index variable which references the user
K	The number of users in the system
K_{ψ_l}	The number of users included in the MUMD at antenna l

$\mathbf{K}_{\mathbf{y},\psi_l}$	Covariance matrix of matched filter outputs for the users in ψ_l
l	An index variable which references the antenna
L	The number of antennas in the system
$M(\Gamma)$	Multiplicative factor for downlink optimization
n	The n^{th} symbol
N	The total number of transmitted data symbols
N	Can also refer to the frame length for the multiuser channel estimator
N_o	The power spectral density of the AWGN
P_k	User k's average signal power
$P(\varepsilon)$	Probability of pairwise error
$\mathbf{P}_l(n)$	Cross-correlation between observation vector and channel gain vector
Q	The interpolator order for the multiuser channel estimator is $2Q+1$
$r_l(t)$	Received signal at antenna l
R	Data rate
$\mathbf{R}_{\mathbf{s},\psi_l}$	Transmitted signature waveform cross-correlation matrix for the users in ψ_l
$\mathbf{R}_{\mathbf{s},\psi_l,\phi_l}$	Transmitted signature waveform cross-correlation matrix between the users in ψ_l and the users in ϕ_l
$\mathbf{R}_{\theta_l}$	Auto-correlation matrix for the observation vector
$s_k(t)$	Transmitted signature waveform for user k
$\mathbf{s}_{\psi_l}$	Vector of transmitted signature waveforms for the users in ψ_l
T	Symbol duration
T_c	Chip duration
T_d	Delay spread
$\mathbf{U}_l(n)$	Matrix of weights for the multiuser channel estimation
$v_{lkg}(n)$	Estimate of the complex channel gain for antenna l, user k, and path g
$\mathbf{v}_{\psi_l}$	Vector of complex channel gain estimates for the users in ψ_l
$w(\varepsilon)$	Hamming weight of error sequence
x	Index variable which references the user
$\mathbf{y}_{\psi_l}$	Vector of matched filter outputs for the users in ψ_l
$z_l(t)$	The additive white Gaussian noise at antenna l
$\mathbf{z}_{\psi_l}$	The AWGN projected on to $\widehat{\mathbf{s}}_{\psi_l}$
α	The alphabet for a BPSK signal

$\beta_k(n)$	Set of indecomposable sequences with $\varepsilon_k(n) \neq 0$
Γ	Effective energy to interference and noise density ratio
Γ_t	Targeted effective energy to interference and noise density ratio
$\varepsilon_k(n)$	The individual elements in the error sequence
$\boldsymbol{\varepsilon}$	The error sequence
η_{lkg}	Correlation coefficient between the complex channel gain and the channel estimate for antenna l, user k, and path g
$\boldsymbol{\theta}_l$	Observation vector for the multiuser channel estimator
Θ	Tentative decision data symbol set
λ	Log-likelihood metric
$\Lambda(h)$	Set of log-likelihood metrics for all of the various data symbol values in $\Psi(h)$
$\boldsymbol{\xi}_{\mathbf{c},\mathbf{v},\psi_l}(m)$	Cross-correlation between $\mathbf{c}_{\psi_l}(n)$ and $\mathbf{v}_{\psi_l}(n-m)$
ρ_{xk}	Cross-correlation between user x's and user k's transmitted signature waveforms
$\sigma^2_{c,lkg}$	Variance of c for antenna l, user k, and path g
τ_{lk}	Transmission delay between the k^{th} user and the l^{th} antenna
Υ	Signal to noise ratio
ϕ_l	Users that are treated as MAI at antenna l
$\Phi(s)$	Characteristic function of d_{ij}
ψ_l	Users that are included in the MUMD at antenna l
$\Psi(h)$	Data symbol set for index variable, h
$\Omega_{\mathbf{c},\mathbf{v},\psi_l}$	Cross-correlation between $\mathbf{c}_{\psi_l}$ and $\mathbf{v}_{\psi_l}$

Chapter 1

Introduction and Background

With the ever increasing demand for wireless, personal, and portable communications, system planners for cellular systems and personal communication systems (PCS's) constantly strive to expand and improve upon their existing networks. While traditional cellular systems have provided people with the freedom to use mobile phones to verbally communicate with other users, PCS technologies augment mobile voice communication with other services such as mobile fax, image, and video.

In wireless communication systems, there are generally three different multiple access techniques. These are frequency division multiple access (FDMA), time division multiple access (TDMA), and code division multiple access (CDMA). FDMA systems divide the available spectrum into portions, and a number of mobiles are serviced by assigning each user a different portion of the spectrum. With TDMA, each radio channel is separated into a number of time slots, and each user is assigned a particular time/frequency slot combination. Unlike both FDMA and TDMA, CDMA enables a number of users to share the same space, time, and frequency with the use of spread spectrum techniques. The term spread spectrum refers to the fact that a bandwidth of W Hz is used to send data at a rate of R bits/sec, and W is much greater than R. The ratio W/R is commonly referred to as the processing gain, and the larger the processing gain, the better the CDMA system is at suppressing the multiple access interference (MAI). Unlike the more traditional multiple access techniques such as FDMA and TDMA, CDMA has no hard limit on capacity.

As the demand for wireless, mobile communications increases, capacity is a prime concern for both cellular and PCS providers. In addition to the need for increasing capacity, applications such as fax, image, and video require a higher quality of service (QoS) than

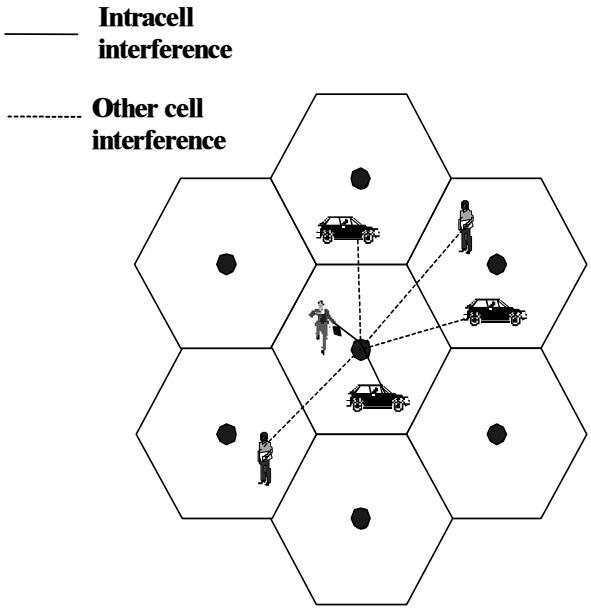

Figure 1.1: Typical layout for outdoor system.

that traditionally needed for voice communications. CDMA technology, with its noise-like signal waveforms, universal frequency reuse, and flexible architecture, is ideal for meeting increasing capacity requirements and various QoS levels. Since CDMA systems are inherently interference limited, the system's capacity and/or the QoS automatically increases with any reduction in interference [1].

The general layouts for outdoor and indoor wireless communications systems are shown in Figs. 1.1 and 1.2, respectively. The intracell interference in Figs. 1.1 and 1.2 is the interference that is generated from within the cell of interest, while other cell interference originates from the neighboring cells. CDMA systems use a number of techniques such as antenna sectorization, power control, and soft handoff to reduce the level of interference present at the receiver. These techniques along with their effect on capacity will be discussed in detail later in this chapter. Even though the overall level of interference can be reduced at the receiver, the performance of the traditional linear detector is still limited by the intracell and other cell interference. Typically, CDMA systems use linear detectors similar to that shown in Fig. 1.3. As can be seen in Fig. 1.3, the conventional detector consists of a bank of single-user matched filters followed by a symbol-rate sampler and a threshold device. The

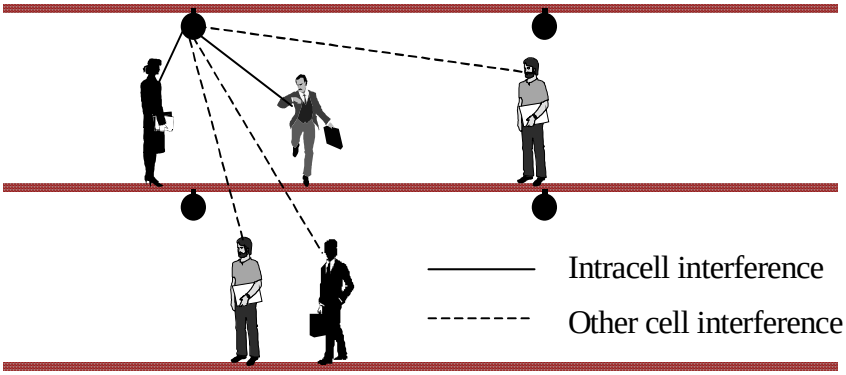

Figure 1.2: Typical layout for indoor system.

conventional detector performs very well when the thermal noise is dominant. However, it is far from optimum in the presence of MAI.

The optimum, maximum likelihood (ML), multiuser detector is proposed in [2], and it is shown that this detector is capable of nearly eliminating the effects of MAI. Multiuser detection is typically performed only for users within a cell of interest. With such a restriction, multiuser detection has the ability to nearly eliminate the intracell MAI. However, it does nothing to combat the other cell interference.

If the widely separated base stations shown in either Fig. 1.1 or Fig. 1.2 could share information about users, the other cell interference could be transformed into useful information. For example, a user's performance could be improved through macrodiversity reception, which occurs when the user's signal is detected at more than one base station. Further, if these signals were added to the multiuser detection at each base station, the ML multiuser detectors would now have the ability to combat both intracell and other cell interference. To summarize, CDMA users can benefit from the addition of macrodiversity to multiuser detection in two ways. The first way is by taking advantage of the diversity already present in the system, and the second way is through improved ML multiuser detection.

In this thesis, ML multiuser-macrodiversity detection is applied to both outdoor and indoor wireless communication systems. Consequently, the next section focuses on radio signal propagation in these environments.

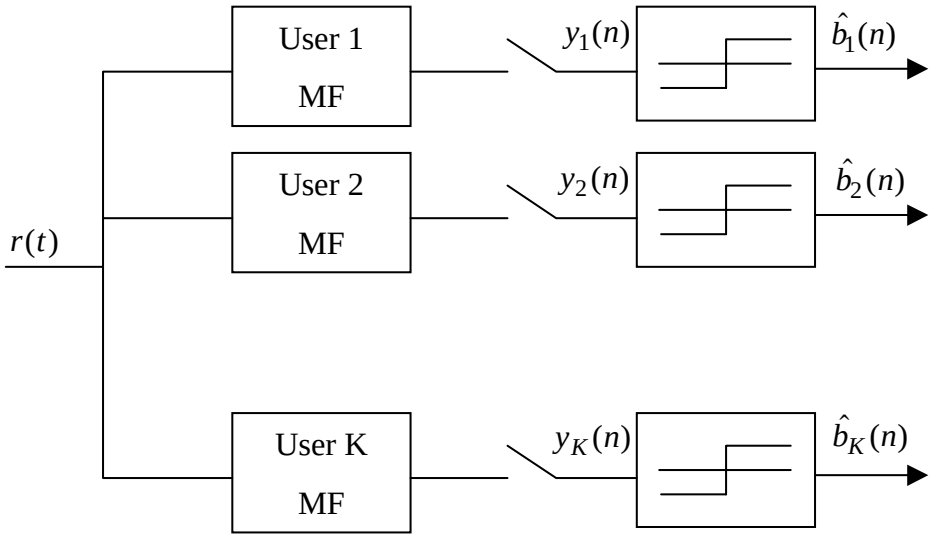

Figure 1.3: Traditional CDMA linear detector.

1.1 Outdoor and Indoor Propagation

Path loss plays an extremely important role in the design of both outdoor and indoor wireless systems. In general it determines a cell's coverage area, and it also determines the extent to which different cells interfere with each other. The simple plane earth model of path loss does not apply to mobile communications since additional interference occurs as a result of multiple diffractions around large objects [3].

The path loss exponent determines the rate at which path loss increases with increasing distance between the transmitter and the receiver. It has been shown that the path loss exponent typically ranges between 3 and 4 in urban and suburban environments [3]. A range of approximately 2.5 to 5 appears to be typical of the indoor environment [4], [5]. As illustrated in Fig. 1.4, large obstacles in the propagation path between the base station antenna and the mobile result in shadowing, which causes variability around the predicted path loss. Shadowing normally occurs over areas on the order of hundreds of wavelengths, and it is typically considered to be log-normally distributed with a standard deviation of 6 to 8 dB [3]. However, the range in standard deviations appears to be larger in the indoor environment, taking values from about 4 dB to 10 dB [4], [5]. Finally, fading occurs on a very small scale, when the mobile is surrounded by a number of reflectors, and causes power

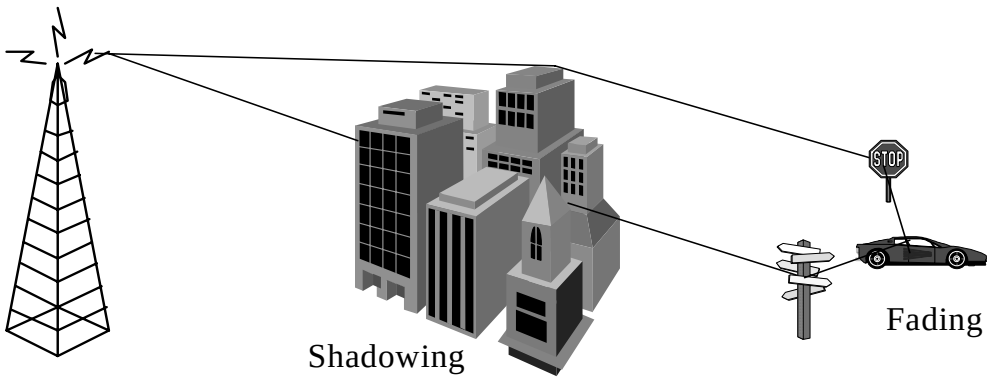

Figure 1.4: The physical basis of shadowing and fading.

fluctuations around the mean predicted by both path loss and shadowing. It is generally assumed that the fading has either a Rayleigh or a Rician distribution [3].

In a multipath fading environment, the received signal is composed of multiple reflections of the transmitted signal which each have their own direction of arrival, amplitude, phase, and delay [3]. A mobile experiences fading as it moves since the amplitude and phase of its composite signal changes, and the rate of change depends on the speed at which the mobile moves. If we assume that the scatterers are evenly distributed around the mobile, the power spectrum of the complex gain, i.e., the Doppler spectrum, attains a U-shape. The resulting autocorrelation function in time is given by the Bessel function of the first kind [3].

The fading experienced by a mobile can be either flat or frequency selective. The fading is flat if the range of delays (the delay spread) is small compared $1/W$, where W is the transmission bandwidth. However, if the delay spread is greater than $1/W$, the fading becomes frequency selective. In frequency selective fading, the power delay profile describes the distribution of the arrivals' mean-square values in the delay domain. It is common to assume an exponential power delay profile in an urban setting [3], and the authors of [6] found that an exponential power delay profile is also typical in indoor systems.

A great deal of the work performed to date on indoor wireless propagation has concentrated on wideband measurements that reveal the delay spread characteristics of the indoor wireless multipath propagation [6], [7], [8]. This work will be extremely useful for wideband

systems such as wideband CDMA. However, for the IS-95 specification, delay spread is currently not an issue in the indoor environment as it is typically less than the chip interval, where the chip interval is the inverse of the transmission bandwidth.

The indoor propagation studies at the University of Auckland have taken the focus off delay spread and placed it on overall path losses at various locations within a building [4]. These propagation measurements have identified a strong correlation in the signal strengths between floors of a building. This is due to the fact that the correlated paths share a number of common obstacles. The correlated shadowing that exists within a building has a strong influence on base station placement as is shown in [9]. The authors show that for a simple layout with one base station per floor, the positive correlation between floors suggests that the base stations should be aligned from floor to floor rather than offset. Some recent experiments at the University of Auckland involve measurements taken from simultaneous transmissions on multiple floors [4]. The authors measure the mean path losses and calculate correlation coefficients for different transmitter and receiver positions both across and between floors of a multi-story building. These experiments are directly applicable to the study of macrodiversity as they will identify the expected power at multiple base stations from a transmitting mobile.

Before addressing the issues of either macrodiversity or multiuser detection, the impact of using the traditional linear detector on CDMA system capacity is discussed in the following section.

1.2 CDMA System Capacity and Power Control

Typically, the forward link capacity exceeds the reverse link capacity in a CDMA system [10]. Therefore, in this section, system capacity refers to the reverse link capacity. For simplicity we initially concentrate on a single cell within the CDMA system.

If each user's transmitted power is controlled so that all of the signals arrive at the base station with equal power levels, the energy to interference and noise density ratio, Γ, is given as [1]

$$\begin{aligned} \Gamma &= \frac{E_b}{I_0 + N_0} \\ &= \frac{P_r/R}{(N-1)\,P_r/W + N_0} \end{aligned} \tag{1.1}$$

where E_b is the energy per bit, I_0 is the interference, and N_0 is the power spectral density of the thermal noise. The transmission bandwidth is given by W, R refers to the data rate, P_r is the received signal power of each user, and N is the number of users in the cell.

In the following capacity estimates, we have assumed that the MAI appears to be noise-like and random. However, in a realizable system the signals must be "pseudorandom" so that they can be generated at both the transmitter and the receiver. These pseudorandom sequences need to be well designed with good autocorrelation and cross-correlation properties for all possible delays between the sequences so that they do indeed resemble background noise [12]. By rearranging (1.1), we calculate the capacity for conventional receivers to be

$$N - 1 = \frac{W/R}{\Gamma} - \frac{N_0 W}{P_r}. \tag{1.2}$$

Assuming that the thermal noise is negligible compared to the interference from other users, we can estimate the capacity to be approximately

$$N \approx \frac{W/R}{\Gamma} \tag{1.3}$$

where Γ is the required value for adequate performance. However, this capacity estimate is optimistic as it does not account for the interference introduced by the other cells in the system. As shown in [10], the other cell interference is calculated to be approximately $f = 60\%$ of the interference generated by the given cell. Therefore, the capacity estimate in (1.3) must be reduced by a factor of $1 + f = 1.6$, and the capacity per cell of a multi-cell CDMA system becomes

$$N \approx \frac{W/R}{\Gamma\,(1+f)}. \tag{1.4}$$

However, as stated earlier, CDMA systems are interference limited, and any reduction in interference translates to an increase in capacity. One of the more popular methods in reducing the interference for voice communication includes suppressing transmission during a user's quiet period. Studies have shown that a user's voice is active only about 35% to 40% of the time [11]. Therefore, the voice activity factor, α, is typically taken to be $\alpha = 3/8$ [1], [10]. Another way to combat the level of MAI is through the use of directional antennas that isolate the desired user and suppress the interferers. If the users are uniformly distributed across the cell, the MAI can be reduced by using a sectored antenna. If the sectorization were perfect, the interference would be reduced by the number of sectors. However, if we

assume a loss of 1 dB from the ideal gain, the antenna gain factor, G_A, is approximately $G_A \approx 2.4$ for a three-sectored antenna [10].

By taking the voice activity and antenna gain factors into account, the capacity per cell of the CDMA system becomes

$$N \approx \frac{(W/R)\,(G_A)}{\Gamma\,(1+f)\,(\alpha)}. \tag{1.5}$$

Another way to interpret (1.5) is that for a given number of users the voice activity and antenna gain factors increase the energy to interference and noise density ratio, Γ, by approximately 8 dB. Therefore, any reduction in interference results in either an increase in capacity for a specific Γ or an increase in Γ for a given number of users.

As stated previously, the above calculations assume that the power of each mobile is perfectly controlled. However, perfect power control is difficult if not impossible to attain. Therefore, the following sections address methods used for both reverse link and forward link power control.

1.2.1 Reverse Link Power Control

The capacity estimates, (1.2) - (1.5), assume that the signals arrive at the base station with equal power. The equal power assumption is critical for maximizing the capacity in a CDMA system that uses conventional detectors. One of the major problems to date with DS-CDMA systems is the near-far problem. The near-far problem occurs when weak users cannot be detected at the receiver because they are overpowered by stronger users. It is the power control mechanism in a CDMA system that attempts to alleviate the near-far problem and equalize the received signal powers. Reverse link power control consists of both open-loop and closed-loop power control.

The wide dynamic range in signal levels is handled by the open-loop power control. The mobile measures its total received power, including the signal power, thermal noise, and interference. The reverse link open-loop power control ensures that the sum of the mobile's received power and the mobile's transmitted power in dB is kept at a specific constant [10]. If the forward link and reverse link carrier frequencies were similar, the channel would be symmetrical, and the open-loop power control would be sufficient. However, the separation between the forward and reverse link channel frequencies is 45 MHz for cellular systems and 80 MHz for PCS systems [13]. These large frequency separations result in different fading

processes between the forward and reverse link. Since the forward and reverse channels are not symmetrical, open-loop power control alone is insufficient, and closed-loop power control is required to "fine-tune" the open-loop estimate.

The closed-loop power control is initiated by the base station. The base station measures the received energy to interference and noise density ratio, Γ, and compares it to a set point. If the received Γ is above the set point, a "down" command is sent, and if Γ is below the set point, an "up" command is sent [13]. For each "up" or "down" command, received from the base station, the mobile adjusts its power by about 1 dB [13]. The base station can also send a "do nothing" command to keep the mobile transmitting at a constant power. The closed-loop power control sends 800 commands per second [13]. While this is very rapid control, it may not always be fast enough to track the Rayleigh fading. However, it should not have any difficulty tracking the path loss and shadowing effects [1]. The errors associated with the reverse link power control are approximately log-normal with a standard deviation of about 2 dB [13].

1.2.2 Forward Link Power Control

The requirements on forward link power control are generally less severe than those on the reverse link [13]. On the forward link, all of the intracell interference arises from the same base station. As a consequence, the desired and interfering signals vary together. Therefore, in a single cell system, the total signal level at the mobile must be adequate, but forward link power control by user is not required. In a multi-cell system, forward link power control becomes necessary as the neighboring cells' interference fades independently from that of the given cell. In order to perform forward link power control, each base station allocates power to a particular mobile user based on that mobile's SNR [1]. The mobile calculates its SNR by correlating to the strongest pilot signal and measuring its energy along with the total energy received [1]. Both of these measurements are transmitted to the base station with the strongest pilot so that this base station can provide the proper power allocation.

Thus far, the descriptions for both the reverse link and forward link power control have assumed that each user is communicating with only one base station. If a user is connected to more than one base station in soft handoff or macrodiversity, the power control mechanism will need to be adjusted accordingly. The following section addresses the general area of diversity, and macrodiversity is specifically addressed in 1.3.2.

1.3 Diversity

Diversity reception is one of the most effective methods for significantly decreasing a user's bit error rate (BER). In general there are four main sources of diversity: polarization, time, frequency, and space diversity. Polarization diversity can be obtained if signals are transmitted in both the vertical and horizontal electric fields since the vertical and horizontal polarizations are uncorrelated, or only weakly correlated [14]. Time diversity can be obtained if the transmissions exceed the coherence time of the channel, where the coherence time is defined as the time over which the channel's complex gain remains approximately constant [3]. In a CDMA system, time diversity is obtained through the use of powerful convolutional codes combined with interleaving. If the interleaving is of sufficient depth, the previously separated consecutive codeword symbols exceed the coherence time of the channel and thus experience independent fading. Frequency diversity can be obtained if the transmission bandwidth is greater than the coherence bandwidth of the channel, where the coherence bandwidth is termed the "distortion free bandwidth" in [3]. In spread spectrum communications, a RAKE receiver is the preferred method for obtaining frequency diversity [10]. In total the RAKE receiver can combine $G + 1$ resolvable paths, where $G = \lfloor WT_d \rfloor$, and T_d is the delay spread of the channel [15]. Finally, space diversity is obtained through the use of multiple antennas when the antennas are spaced far enough apart to ensure independent fading. In the following we discuss both microdiversity and macrodiversity. Since most of the previous research to date has focused on microdiversity, this issue is addressed first.

1.3.1 Microdiversity

Microdiversity occurs when the antennas are spaced close enough together to ensure that the signal's mean power level is the same at each antenna, but far enough apart to ensure independent, or close to independent, fading at each antenna.

Conceptually, the simplest type of diversity is selection diversity. For ideal selection diversity, the best signal is selected for reception. However, selection diversity is difficult to implement as the threshold for switching between branches is a floating threshold [14]. A more practical technique is known as switched diversity where the receiver switches branches only if the signal drops below a pre-determined threshold [14]. While ideal selection diversity outperforms the switch-and-stay variation, diversity performance can be further improved

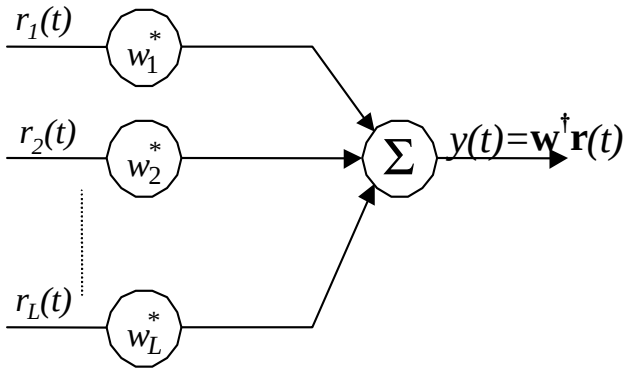

Figure 1.5: Conventional array.

by combining the signals rather than selecting them. The signals can be combined using a conventional array as shown in Fig. 1.5. In the figure there are L microdiversity antennas. The received signals are given by $\mathbf{r}(t) = [r_1(t), ..., r_L(t)]^{\mathrm{T}}$, and the weight vector is given by $\mathbf{w} = [w_1, ..., w_L]^{\mathrm{T}}$. The weights can be adjusted according to many different criteria such as minimum mean square error (MMSE), signal to interference and noise ratio (SINR), or maximum likelihood (ML).

J. Winters showed that "optimum" combining applied to antennas in space diversity is able to both reduce directional interference as well as combat fading of the desired signal [16]. He uses the maximization of output SINR as the performance measure for the antenna array. It is shown in [17] that the MMSE, SINR, and ML criteria applied to the conventional array shown in Fig. 1.5 are all closely related to each other, and they differ only by scale factors. These solutions all yield identical output SNRs, and they are often termed "optimal" since their solutions can be written in terms of the optimum Wiener solution [17]. However, even though MMSE combining is one of the "optimal" combining methods, [18] shows that the performance of multiuser, or joint, detection far exceeds that of MMSE combining.

As stated above, "optimum" combining combats the desired signal's fading and reduces directional interference. If the interference is negligible compared to the noise, MMSE combining reduces to maximal ratio combining. In contrast, if the noise is negligible compared to the interference, MMSE turns into zero forcing. Most often in practice, neither of these conditions is met, and both interference and noise are significant. When both interference and noise are present, MMSE combining outperforms both maximal ratio and zero forcing.

The authors of [19] study the high SNR case that results in the zero forcing solution. They show that a system operating with N antennas and $(K+1)$ users, where $N > K+1$, can cancel out K interferers leaving each user with $(N-K)$ order diversity. However, normally the interference does not need to be cancelled; it just needs to be suppressed into the noise. Therefore, these results actually provide an upper bound on the probability of error for the MMSE combining solution.

The results in [16] and [19] assume independent fading at each antenna. However, correlations in the antenna array cause diversity to become less effective. In [20] the authors study the effect of correlated fading on MMSE combining. They found that the correlated fading does not significantly affect the interference suppression capabilities of MMSE combining since cochannel interference (CCI) can be cancelled in all levels of correlation. However, the benefits resulting from diversity are reduced with an increase in correlation. The MMSE combining is less able to combat the desired signal's fading since all the antennas tend to experience a fade simultaneously if the correlation is high. However, even with correlations up to 0.5, there appears to be only a small degradation in performance. Now that we have discussed the issue of microdiversity, we will investigate the more general case of macrodiversity.

1.3.2 Macrodiversity

Antennas which have significant distances between them are said to be in macrodiversity reception. Unlike the microdiversity situation in Section 1.3.1, a signal's average power level will generally be different at each macrodiversity antenna. As a consequence, macrodiversity is used to combat both shadowing and fading. The most common form of macrodiversity in a CDMA system is soft handoff. A mobile is in soft handoff when it sends and receives information to and from more than one base station. The group of base stations that the mobile communicates with is defined as the mobile's Active Set. Similar to the concept of soft handoff, "softer" handoff occurs when the mobile communicates with two or more sectors of the same cell [21].

Since all users share the same bandwidth in a CDMA system, there is no need to switch frequencies when the mobile transfers from one base station to another. When a mobile enters soft handoff, it is typically in a transition region between base stations as shown in Fig. 1.6. In this transition region, the call can be serviced by any of the neighboring base stations. Only once the mobile is well within the boundaries of a cell is the handoff

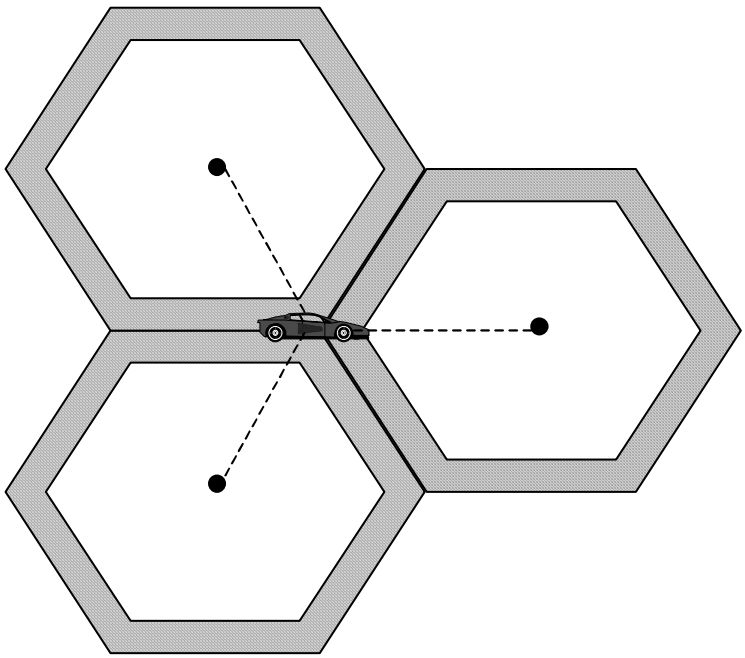

Figure 1.6: Typical soft handoff transition region.

complete, and the other base stations no longer attempt to handle the call [22].

Macrodiversity on the Reverse Link

On the reverse link of a conventional system using soft handoff, the base stations in a mobile's Active Set decode the signals independently. If the message is decoded differently at the various base stations, the system controller, or base station interconnection, determines which base station is receiving the highest quality signal and decides in its favor [10].

In [23] the authors show analytically that soft handoff is capable of increasing both the reverse link capacity and the cell coverage when compared to hard handoff. They present a comprehensive analysis which takes both intracell and other cell interference into account. Their results show that most of the advantages of soft handoff are obtained with two neighboring base stations. The addition of more base stations to the soft handoff has diminishing returns [23].

Typically each cell participating in a soft handoff independently sends a power control bit to the mobile. The mobile reduces its power if it receives a "down" command from any

one of the base stations, and it increases its power only if it receives an "up" command from all of the base stations [13]. In this way the mobile's power is ultimately controlled by the base station receiving the best signal [13]. This keeps the mobile transmit power to a minimum, which in turn minimizes the overall level of interference in the system.

In [24], the Multiply-Detected Macrodiversity (MDM) scheme is developed which outperforms selection-based diversity schemes. The MDM scheme uses a post-detection combining technique, and is based on the maximum likelihood criterion. The MDM decision algorithm combines the individual hard decisions from each base station with a measure of the quality of each link to form the final decision. The authors compare MDM to selection diversity, and they show that MDM has the capability to significantly reduce the system's BER [24].

In [25], a macrodiversity system which uses pre-detection combining is considered. Pre-detection combining generally yields more improvement than post-detection combining. However, it does so at the expense of increased complexity and increased traffic on the wireline network. Therefore, the wireline network may need to be installed with cable or fibre in order to handle the increased traffic. The author develops a power control algorithm based on a carrier to interference spectral density ratio for a macrodiversity network [25]. The signal's phases are aligned before combining the macrodiversity antennas, and the interference is treated as white noise. The power control algorithm is implemented to counteract the effects of shadowing, but it does not attempt to track the fast fading. The required power for each user can be solved with a set of K equations and K unknowns, where K is the number of users in the network. The author also proposes a decentralized version of the power control algorithm which is an adaptive process that converges to the centralized solution. The decentralized version, however, still requires each user to broadcast its own interference level in order to facilitate the power updates of the other users [25].

Macrodiversity on the Forward Link

On the forward link, the neighboring base stations offset their pseudonoise (PN) sequences and transmit simultaneously to the mobile in soft handoff. The mobile's RAKE receiver can isolate and combine these different transmissions as if they were natural multipath produced by the environment [23]. Therefore, soft handoff on the downlink is equivalent to generating artificial multipath. The advantage of this artificial multipath is the increased diversity present at the mobile unit's RAKE receiver. However, the disadvantage of artificial multipath is the increase in the overall level of interference.

In [21], the authors study the tradeoff between the added diversity and the increased interference by comparing CDMA capacity with both soft and "softer" handoff to CDMA capacity without any form of soft handoff. They found that even though soft and "softer" handoff with base stations having three sectors per cell causes the downlink capacity to increase, soft handoff alone in unsectorized cells results in a small capacity loss. The authors of [26] evaluate the effect of varying the soft handoff coverage area. In other words, they vary the size of the transition region. Their results show that there is virtually no benefit in using soft handoff on the forward link as the forward link capacity remains fairly constant regardless of the soft handoff coverage area. A similar investigation was performed in [27] where the effect of a changing soft handoff threshold on forward link capacity is evaluated. The soft handoff threshold determines which base stations will be in the mobile's Active Set by including the base stations whose energy to interference and noise density ratio exceeds the threshold. In contrast to the previous study, [27] found a small capacity increase with a decreasing soft handoff threshold. However, if the threshold is lowered too far, the increase in interference cancels any benefit due to additional diversity.

While the findings of the above three studies, [21], [26] and [27], differ slightly, they all agree that at some point the increased interference generally neutralizes the added diversity for unsectorized cells. In these papers, all of the base stations in the Active Set transmit the same power to the mobile unit in soft handoff. The authors of [28] investigate the allocation of different transmit powers at the base stations in the Active Set, based on the premise that a base station with a better link to the mobile unit should transmit with a higher power. However, this type of power allocation does not balance the decrease in one user's BER due to a transmit power increase against the interference experienced by the other users. In [29], a centralized downlink power control algorithm is introduced for multi-antenna transmission. The authors simplify their solution and create a decentralized algorithm called the "Greedy Algorithm." Their results indicate that the "Greedy Algorithm" meets the same BER requirement as equal power multi-antenna transmission, but with less overall transmit power.

From the above work, it can be observed that there is still room for further investigation into the effects of macrodiversity on the forward link of a DS-CDMA system when the base stations in the Active Set allocate different transmit powers to the mobile unit in soft handoff.

1.4 Multiuser Detection and Interference Cancellation

As can be seen from the capacity estimates in Section 1.2, even with well designed codes and the use of power control, the traditional detector which correlates the received signal with the desired spreading sequence is interference limited and often insufficient. Therefore, a great deal of effort has been targeted towards replacing the conventional detector. It has been shown that multiuser detectors are more robust than the conventional detector in the presence of MAI.

The optimum multiuser detector developed in [2] far outperforms the conventional detector since it nearly eliminates the effects of MAI, and its performance rivals that of a single user system. It consists of a bank of matched filters followed by the Viterbi algorithm, and its complexity grows exponentially with the number of users. Therefore, a suboptimal multiuser detection scheme is proposed in [30] in order to reduce this complexity. The proposed decorrelating receiver is a linear detector, and it is able to achieve the near-far resistance obtained by the optimal multiuser detector. The only time that the conventional detector will outperform the decorrelating receiver is when the MAI is subordinate to the background noise. This is because the decorrelating receiver is the multiple-access equivalent to the zero-forcing equalizer which enhances the background noise while attempting to eliminate the MAI. The MMSE multiuser detector in [31] does not suffer from noise enhancement as does the decorrelating receiver. One of the major disadvantages of the decorrelating and the MMSE multiuser detectors is that ideally the filters have an infinite length, and are thus infinite impulse response (IIR). Adaptive single-user techniques are used in [32] to obtain finite memory-length detectors. Later, in [33] it is shown that the IIR filters can be approximated by FIR filters, and a reasonable number of taps is often sufficient to provide performance similar to that of the original IIR detector.

The performance of the ML detector and the decorrelating detector is analyzed in [2] and [30] respectively for the additive white Gaussian noise (AWGN) channel, and the analysis in [34] extends this to the flat Rayleigh fading channel. The results show that both of the multiuser detectors outperform the conventional detector, and the optimum ML detector's performance approaches that for an isolated transmission. The decorrelator's asymptotic efficiency in the flat Rayleigh fading channel is consistent with that of the AWGN channel [34]. In [35], Z. Zvonar extended the results from the single path fading channel to a frequency selective channel. His paper investigates the use of decorrelating receivers with

both RAKE multipath diversity and antenna diversity. It is shown that this approach improves the performance beyond that achieved with conventional RAKE receivers at the expense of increased complexity.

The studies in [36] and [37] discuss multisensor multiuser receivers. While the authors of [36] state that the multiple sensors could refer to antenna elements or base stations, it is assumed that the set of users represented at each sensor is the same, and the average power levels are similar at each sensor. This situation more closely resembles the combination of multiuser detection with microdiversity. Therefore, rather than including [36] and [37] in Section 1.5, they are included here. The authors of [36] state that the use of multiple sensors tends to average the MAI out towards zero. They also state that with a moderate number of users and a tolerable near-far problem, the use of multisensor detection alone, without any multiuser detection, has the capability to yield relatively good performance. They do, however, compare conventional and decorrelating multisensor detectors, and the decorrelating multisensor detector far outperforms the conventional multisensor detector as expected. This research has been extended in [37] where the authors compare the performance of a multisensor RAKE receiver, a multisensor conventional multistage detector [40], and their multisensor generalized multistage detector. Their conventional multistage detector is similar to the parallel interference cancellation (PIC) multistage detector developed in [40]. As its name implies, PIC involves interference cancellation, and the general class of interference cancellation schemes will be addressed shortly. From the above three multisensor receivers, the generalized multistage detector appears to be best suited to suppressing MAI in heavily loaded systems.

The issue of combining the MMSE multiuser detection in [32] with power control is addressed in [38], and [39] extends this to include beamforming. The authors of [39] show that the total power transmitted by all users is significantly reduced when power control, MMSE multiuser detection, and beamforming are combined.

The decorrelating and MMSE receivers mentioned above are linear multiuser detectors. Another important group of suboptimal multiuser detectors are non-linear detectors which employ interference cancellation (IC). IC receivers attempt to estimate the MAI and subtract it from the received signal. They require knowledge of the users' spreading sequences, channel gains, and delays. Two fundamental classes of IC receivers are parallel interference cancellation and successive interference cancellation (SIC).

PIC receivers attempt to cancel the MAI from all users simultaneously. A well known

multistage PIC receiver is developed in [40]. The authors present a realizable implementation of their algorithm which achieves a fixed decoding delay, and they also show that the computational complexity increases linearly with the number of users.

In contrast to PIC receivers, SIC receivers cancel the MAI successively on a user by user basis. The SIC receiver works by first detecting the strongest user. The strongest user's signal is then subtracted from the composite signal by regenerating it using the user's spreading sequence, channel estimate, delay estimate, and symbol decision. Once the MAI from the strongest user is removed, the second strongest user can be detected, and this process is repeated until the weakest user is detected [41]. The authors of [41] investigate the performance of SIC receivers for both coherent and noncoherent modulation. For the coherent case, it is assumed that the receiver has perfect knowledge of the phase. However, the amplitude information is estimated by the matched filter output. In the noncoherent case, the matched filter is used to estimate both the amplitude and the phase. In [42], the author extends this work by using Pilot Symbol Assisted Modulation (PSAM) for the channel estimation in a SIC receiver. SIC receivers perform best in environments with a large variation in power between users. However, in a heavily loaded system it is likely that some users will have similar power. While the PIC and SIC receivers perform well if all of the decisions are correct, incorrect decisions will have a negative impact on all other users.

All of the work discussed thus far has focused on applying multiuser detection in CDMA networks, and traditionally multiuser detection has been associated with spread spectrum communications. However, a ML multiuser detector that can be used in a TDMA system is presented in [18], and the results show that multiuser detection is also extremely attractive in narrowband TDMA systems.

Now that the optimal and the various types of suboptimal multiuser detection schemes have been discussed, the benefits of combining multiuser detection with macrodiversity will be outlined in the following section.

1.5 Multiuser Detection and Macrodiversity

The idea of combining multiuser detection with macrodiversity is still relatively new. There have been a few initial studies on this topic which show that it is a promising area for further investigation. Intracell macrodiversity in a Joint Detection (JD)-CDMA system is investigated in [43], where intracell macrodiversity refers to macrodiversity within a cell.

In order to perform the intracell macrodiversity, remote antennas are deployed which are connected to the central base station. The results show that the carrier to interference ratio can be reduced by about 3-4 dB while maintaining the same outage probability when three remote antennas are deployed [43].

The authors of [44] study multiuser detection with base station diversity in a TDMA system. The multiuser detector at each base station produces a log-likelihood ratio, and the diversity is obtained by using equal gain combining of log-likelihood ratios. This approach has similarities to the MDM algorithm presented in [24]. While the MDM algorithm was originally designed for hard decisions, [44] extends this to incorporate soft decisions. This technique of combining multiuser detection with macrodiversity results in a significant BER reduction. These results are produced assuming that the receiver has perfect channel state information (CSI) and perfect code synchronization. In their paper, the authors state that optimal multiuser detection cannot be combined with macrodiversity since optimal multiuser detectors are implemented using the Viterbi algorithm which produces hard bit decisions. However, Chapter 3 of this thesis proposes the Conditional Metric Merge (CMM) algorithm which, similar to the Viterbi algorithm, utilizes a dynamic programming approach. It is the CMM algorithm that enables optimal multiuser-macrodiversity detection.

In [45], the authors investigate the performance of macrodiversity in conjunction with conventional detectors, linear MMSE multiuser detectors and decision-based (or SIC) detectors. The detectors are developed for both synchronous and asynchronous CDMA systems. However, performance results are reported only for the synchronous systems. The results reported in [45] are valid for static AWGN channels with perfect CSI and perfect code synchronization. Again, these results show promise in the area of multiuser-macrodiversity detection. However, further research needs to be done to determine the performance of optimal, ML, multiuser-macrodiversity detection in Rayleigh fading channels. Since all of the multiuser detection schemes rely on accurate CSI and accurate code synchronization, we will discuss these issues in the following section.

1.6 Code Synchronization and Channel Estimation

To date, most of the multiuser detection research has assumed perfect knowledge of the channel parameters. There have, however, been a few studies on the impact of estimation errors on multiuser detection [46], [47], [48]. For example, in [46], the authors study the

impact of misjudging the amplitude, phase, and delays of two asynchronous users in an underwater communications system. They quantify the reduction in asymptotic multiuser efficiency (AME) for both the optimal ML detector and the suboptimal 2-stage detector developed in [40]. AME is defined in [49] as "the ratio between the SNR required to achieve the same uncoded bit error rate in the absence of interfering users and the actual SNR." The authors of [46] found that the AMEs of both multiuser detectors eventually approached zero as the mismatch in timing, amplitude, and phase increased. The authors conclude that since optimal ML detection is extremely computationally complex, it is only warranted when the timing, amplitude, and phase estimates are nearly perfect [46].

The problem of estimating signal amplitudes and phases while simultaneously detecting the data in a multiuser communications system is addressed in [50]. The complex amplitude is estimated using a recursive least-squares algorithm, and it is assumed that the receiver has a priori knowledge of the relative delays [50]. This assumption is removed in [51] where methods for estimating the complex amplitude are also presented for receivers which have no knowledge of the time delays.

A subspace based approach is used in [52] to estimate the relative delays and the signal amplitudes in a multiuser DS-CDMA system. In [52], Bensley and Aazhang decompose the multiuser problem into a number of single user problems, and they use the signal's sample correlation matrix to separate the observation space into both signal and noise subspaces. While this method can estimate a signal's amplitude and delay, the second order statistics contain no phase information, and the signal's phase cannot be recovered [52]. Subspace-based methods are also used in [53] for propagation delay estimation. The authors state that if the complex gain is needed for coherent detection, pilot symbols could be used to extract this information. Subspace-based approaches are attractive as they do not require any type of training sequence. However, as a result of the eigenvector decomposition, they are rather computationally complex.

ML synchronization of DS-CDMA signals is addressed in [54], and Bensley and Aazhang again decompose the multiuser estimation into a number of single user problems. In [54], the interfering users are treated as colored non-Gaussian noise, and ML estimates are developed based on both the Cholesky and eigenvector decompositions. The users' delay, amplitude, and phase are estimated, but results are reported only for the delay estimates. Unlike the subspace-based approaches, ML synchronization generally requires a training sequence to

be sent during initial acquisition. However, the ML synchronization in [54] achieves acquisition faster than the subspace method in [52], and it does so with lower computational complexity. ML parameter estimation in a multiuser CDMA system is also addressed in [55], [56], and [57]. All three papers estimate the amplitudes, phases, and delays of each user's channel impulse response. Unlike the approach in [54] which assumes that the delay spread is insignificant, [55], [56], and [57] assume that the channel is frequency selective. While the method developed in [55] estimates the parameters of the channel impulse response, the authors focus on the issue of synchronization. They first develop a ML approach which estimates the relative delays for all users. However, since this approach is far too computationally complex, they present a more practical single-user ML estimator. The authors derive the Cramér-Rao bound which bounds the best performance achievable of an unbiased estimator. They show that their single-user ML estimator exhibits near-far resistance, and its performance is fairly close to the Cramér-Rao bound.

Even though the ML parameter estimation techniques discussed above are able to estimate a channel's complex gain, they do so during a training sequence which is sent during initial acquisition. It is stated in [54] that their algorithm should track slowly changing parameters. However, the fading process needs to be sampled at or above the Nyquist rate in order to adequately track the channel's complex gain information [58]. The insertion of pilot symbols into the data stream has proven to be an effective method of obtaining channel estimates in a single user system with moderate to rapid fading [58]. In [42], the author extends the method of Pilot Symbol Assisted Modulation (PSAM) to a SIC receiver operating in a Rayleigh fading environment. A decorrelator is used for estimating the channels' complex gains, and the author investigates the effect of inserting one pilot symbol per user, inserting three consecutive pilot symbols per user, and inserting one pilot symbol surrounded by guard intervals per user. In [59], the authors propose a pilot-based, MMSE, multiuser channel estimation technique for a TDMA system. The method allows for time variation in the channels both within and between the training sequences, and the authors also design appropriate training sequences which have good autocorrelation and cross-correlation properties. The MMSE multiuser channel estimation in [59] produces extremely accurate channel estimates that can be used with the ML detector. Therefore, Chapter 4 extends the method in [59] for use in a CDMA system.

The following section identifies the contributions that this thesis makes to the area of macrodiversity combining.

1.7 Thesis Contributions

This thesis contains several contributions to the area of macrodiversity combining.

In Chapter 2, the ML multiuser-macrodiversity detector is derived. This derivation is the first to account for the fact that the multiuser detection at each macrodiversity antenna includes different, and often overlapping, sets of users. Further manipulation reveals that the metric for ML multiuser-macrodiversity detection can be written so that it is composed of sums of terms that depend on only a few symbols at a time. Once this metric structure has been revealed, it becomes evident that a dynamic programming approach can be applied to the ML multiuser-macrodiversity detector to keep its computational complexity at a minimum.

The Conditional Metric Merge algorithm presented in Chapter 3 is the realization of this dynamic programming approach. The CMM algorithm is a central contribution of this thesis. It is the key to ML multiuser-macrodiversity detection as it illustrates how the ML multiuser-macrodiversity detector would be implemented in practice.

Chapter 4 presents a new MMSE multiuser channel estimation technique that extends the work of [59] to be used in a DS-CDMA system. This channel estimation technique has the ability to track the complex gains of channels subject to frequency selective fading and imperfect code synchronization.

A performance analysis is conducted on the ML multiuser-macrodiversity detector in Chapter 5. This appears to be the first analytical treatment of the ML multiuser-macrodiversity detector in Rayleigh fading channels, and it also includes the effects of frequency selective fading, imperfect synchronization, and imperfect channel state information.

Chapter 7 presents an algorithm for optimizing the transmit power of macrodiversity antennas in the downlink of an indoor DS-CDMA system. It is shown that the power optimization increases the downlink capacity by about 10 - 20 %.

Finally, Appendix A presents a new computational tool for use in general fading channel analyses when the detection scheme can be expressed as a quadratic form in zero-mean complex Gaussian random variables. This method is capable of inverting a characteristic function which consists of both multiple and simple poles. It is numerically stable, eliminates singularities and circumvents the need for differentiation.

Each of these contributions will be discussed in detail in the following chapters of this thesis.

Chapter 2

ML Multiuser-Macrodiversity Detection

Traditionally, multiuser detection has been combined with microdiversity where the antennas are co-located and have the same set of users [35]. In contrast, this thesis combines multiuser detection with macrodiversity where widely separated base stations or antennas share information about users. Macrodiversity is unlike microdiversity since each user's signal arrives at the various antennas with different relative delays and mean square values. As a result, the antennas include different, but often overlapping, sets of users in the multiuser-macrodiversity detection (MUMD). In a CDMA system, users can benefit from the addition of macrodiversity to multiuser detection in two ways. The first way is by taking advantage of the diversity already present in the system, and the second way is through improved ML multiuser detection.

The complexity of the ML multiuser-macrodiversity detector grows exponentially with the number of users since it is based on the detector developed in [2]. To mitigate this growth, Chapter 3 presents the new Conditional Metric Merge algorithm which is designed to keep the exponent of exponential growth for the ML multiuser-macrodiversity detector to a minimum. Further, it may be attractive in future PCS systems to have a few high bit rate users at lower processing gains, thus making exponential growth not as prohibitive. However, if computational complexity is still an issue, a suboptimal linear detector, such as the decorrelating detector, may be more attractive [30].

The idea of combining macrodiversity with multiuser detection in a DS-CDMA system

is not new, and the previous work in this area is outlined in Section 1.5. To date the optimal ML multiuser-macrodiversity detector has not been investigated. Therefore, this thesis conducts a performance analysis on the ML multiuser-macrodiversity detector in Rayleigh fading channels. The effects of frequency selective fading, imperfect synchronization, and imperfect CSI are also included in the analysis. In this chapter, the system model is presented, and the metric for ML-MUMD is derived.

In order to perform the MUMD, each base station must forward its signals to the system controller, thus causing traffic to increase in the wireline network. A certain amount of data reduction is possible by forwarding the matched filter outputs to the system controller as opposed to the complex envelopes. However, the traffic still increases significantly since the matched filter outputs are analog quantities that need to be digitized. As a practical consideration, the ML multiuser-macrodiversity detector may be better suited to an indoor environment where the fixed network of the system could be installed with either cable or fibre, which would allow for the increase in traffic. However, the analysis is kept general and is applicable to both outdoor and indoor environments. The performance improvement achieved by the multiuser-macrodiversity detector may be very attractive in providing services such as voice, image, and video.

2.1 System Model

An asynchronous multiple-access system is considered where the signal arriving at antenna l is given as:

$$r_l(t) = \sum_{n=-M}^{M} \sum_{k=1}^{K} A_k b_k(n) \sum_{g=0}^{G} c_{lkg}(n)\, s_k(t - nT - \tau_{lk} - gT_c) + z_l(t). \tag{2.1}$$

There are a total of K users in the system, and each user transmits a total of $N = 2M + 1$ data symbols. The transmitted signature waveform for user k is given by $s_k(t)$ and has support $[0, T]$. The transmission delay of the first arrival between the k^{th} user and the l^{th} antenna is given by τ_{lk}, and a resolution of T_c is achieved for the subsequent arrivals in the multipath delay profile. A_k is user k's amplitude factor, and the average power of the transmitted signal is $P_k = A_k^2/(2T)$. $b_k(n)$ is the n^{th} BPSK information symbol of the k^{th} user, and the data is sent at a symbol rate of $1/T$. $z_l(t)$ is the additive white Gaussian noise (AWGN) at antenna l; it is a complex Gaussian process with zero mean and a power spectral density of N_o.

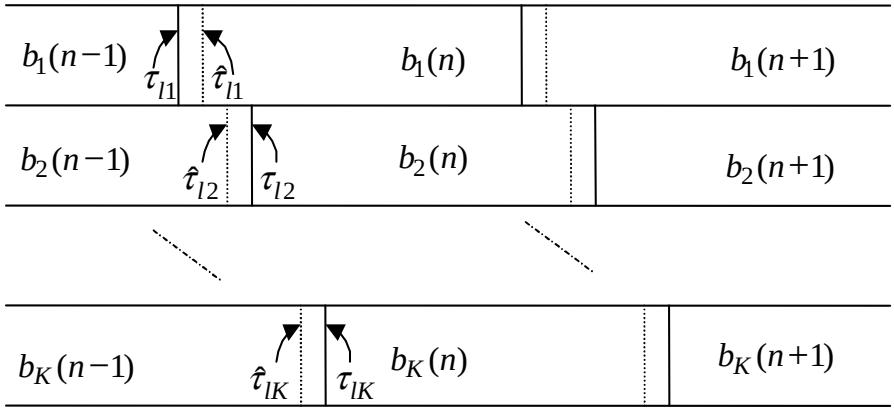

Figure 2.1: Users' Information Symbol Sequences at antenna l.

It is assumed that the channel follows the wide sense stationary uncorrelated scattering (WSSUS) channel model. The frequency selective channel between the k^{th} user and the l^{th} antenna is represented using a tapped delay line with spacing T_c, where T_c is the chip duration such that $T_c = \left(\frac{R}{W}\right) T$, and W/R is the processing gain of the system. The number of resolvable paths is determined by the chip duration, T_c, and the delay spread, T_d, such that $G = \lfloor T_d/T_c \rfloor$. The complex Gaussian channel gain for the g^{th} resolvable path between the k^{th} user and the l^{th} antenna is $c_{lkg}(n)$ with variance $\sigma^2_{c,lkg}$ and Doppler spread f_D. Its autocorrelation function can be written as

$$R_{c,lkg}(n) = \sigma^2_{c,lkg} J_o(2\pi f_D T n) \tag{2.2}$$

which has the power spectrum characteristic of isotropic scattering [14].

Fig. 2.1 shows the users' information symbols arriving at antenna l. For the purposes of description, the relative delays in the figure have been ordered such that $0 < \tau_{l1} < ... < \tau_{lK} < T$. However, in general, the ordering will be different at each antenna in a macrodiversity system. For clarity, the subsequent arrivals due to frequency selective fading have been omitted from the diagram in Fig. 2.1. τ_{lk} denotes the actual transmission delay between the k^{th} user and the l^{th} antenna, and $\widehat{\tau}_{lk}$ is the estimate of this delay. The timing estimation errors are limited to $\frac{-T_c}{2} \leq \tau_{lk} - \widehat{\tau}_{lk} \leq \frac{T_c}{2}$ and cause a portion of the adjacent data symbols to act as interference in the detection.

The other sources of interference come from the imperfect channel estimates, the white

noise, and the multiple access interference (MAI), which is described as follows. Theoretically, all K signals are present at antenna l. However, some of these signals will be too weak to include in the MUMD. These weaker signals will then act as MAI in the detection.

By rewriting (2.1), the received signal at antenna l is now given as

$$r_l(t) = \mathbf{s}_{\psi_l}^T \mathbf{B}_{\psi_l} \mathbf{c}_{\psi_l} + \mathbf{s}_{\phi_l}^T \mathbf{B}_{\phi_l} \mathbf{c}_{\phi_l} + z_l(t) \tag{2.3}$$

where ψ_l and ϕ_l represent two sets of users. The users in ψ_l are included in the MUMD at antenna l, while the users in ϕ_l are treated as MAI. The $\mathbf{s}_{\psi_l}$, $\mathbf{B}_{\psi_l}$, and $\mathbf{c}_{\psi_l}$ in (2.3) are defined below.

$$\mathbf{s}_{\psi_l} = \left[\mathbf{s}_{\psi_l}^{\mathrm{T}}(-M), ..., \mathbf{s}_{\psi_l}^{\mathrm{T}}(M)\right]^{\mathrm{T}} \tag{2.4}$$

$$\mathbf{B}_{\psi_l} = diag\left(\mathbf{B}_{\psi_l}(-M), ..., \mathbf{B}_{\psi_l}(M)\right) \tag{2.5}$$

and

$$\mathbf{c}_{\psi_l} = \left[\mathbf{c}_{\psi_l}^{\mathrm{T}}(-M), ..., \mathbf{c}_{\psi_l}^{\mathrm{T}}(M)\right]^{\mathrm{T}} \tag{2.6}$$

where

$$\mathbf{s}_{\psi_l}(n) = \left[\left\{\left[s_x(t - nT - \tau_{lx}), ..., s_x(t - nT - \tau_{lx} - GT_c)\right] \middle| x \in \psi_l\right\}\right]^{\mathrm{T}} \tag{2.7}$$

$$\mathbf{B}_{\psi_l}(n) = diag\left(\left\{A_x b_x(n) \mathbf{I}_{G+1} \middle| x \in \psi_l\right\}\right) \tag{2.8}$$

and

$$\mathbf{c}_{\psi_l}(n) = \left[\left\{\left[c_{lx0}(n), ..., c_{lxG}(n)\right] \middle| x \in \psi_l\right\}\right]^{\mathrm{T}}. \tag{2.9}$$

The braces are used to show that $\mathbf{s}_{\psi_l}(n)$, $\mathbf{B}_{\psi_l}(n)$, and $\mathbf{c}_{\psi_l}(n)$ are constructed using all values of x where $x \in \psi_l$. For example, $\mathbf{s}_{\psi_l}(n)$ and $\mathbf{c}_{\psi_l}(n)$ are of size $(K_{\psi_l}(G+1) \times 1)$, resulting in $\mathbf{s}_{\psi_l}$ and $\mathbf{c}_{\psi_l}$ of size $(NK_{\psi_l}(G+1) \times 1)$, where K_{ψ_l} is the number of users included in the MUMD at antenna l. Similarly, $\mathbf{B}_{\psi_l}(n)$ is a $(K_{\psi_l}(G+1) \times K_{\psi_l}(G+1))$ matrix, and $\mathbf{B}_{\psi_l}$ is a $(NK_{\psi_l}(G+1) \times NK_{\psi_l}(G+1))$ matrix. $\mathbf{s}_{\phi_l}$, $\mathbf{B}_{\phi_l}$, and $\mathbf{c}_{\phi_l}$ are created in a similar fashion to $\mathbf{s}_{\psi_l}$, $\mathbf{B}_{\psi_l}$, and $\mathbf{c}_{\psi_l}$ by replacing x with u where $u \notin \psi_l$.

The vector of matched filter outputs is given as

$$\mathbf{y}_{\psi_l} = \int_{-\infty}^{\infty} \widehat{\mathbf{s}}_{\psi_l}^{*} r_l(t)\, dt \tag{2.10}$$

where $\widehat{\mathbf{s}}_{\psi_l}$ is the estimate of $\mathbf{s}_{\psi_l}$. The format of $\widehat{\mathbf{s}}_{\psi_l}$ is similar to that of $\mathbf{s}_{\psi_l}$. However, the propagation delays, $\{\tau_{lx}\}$, in $\mathbf{s}_{\psi_l}$ are replaced with the estimates, $\{\widehat{\tau}_{lx}\}$, in $\widehat{\mathbf{s}}_{\psi_l}$. The vector of matched filter outputs can now be written as

$$\mathbf{y}_{\psi_l} = \mathbf{R}_{\mathbf{s},\psi_l}\mathbf{B}_{\psi_l}\mathbf{c}_{\psi_l} + \mathbf{R}_{\mathbf{s},\psi_l,\phi_l}\mathbf{B}_{\phi_l}\mathbf{c}_{\phi_l} + \mathbf{z}_{\psi_l} \tag{2.11}$$

where $\mathbf{R}_{\mathbf{s},\psi_l} = \int_{-\infty}^{\infty} \widehat{\mathbf{s}}^*_{\psi_l}\mathbf{s}^{\mathrm{T}}_{\psi_l} dt$, $\mathbf{R}_{\mathbf{s},\psi_l,\phi_l} = \int_{-\infty}^{\infty} \widehat{\mathbf{s}}^*_{\psi_l}\mathbf{s}^{\mathrm{T}}_{\phi_l} dt$, and $\mathbf{z}_{\psi_l} = \int_{-\infty}^{\infty} \widehat{\mathbf{s}}^*_{\psi_l} z_l(t)\, dt$. In detail,

$$\mathbf{R}_{\mathbf{s},\psi_l} = \begin{bmatrix} \mathbf{R}_{\mathbf{s},\psi_l}(-M,-M) & \mathbf{R}_{\mathbf{s},\psi_l}(-M,-M+1) & 0 & 0 & \\ \mathbf{R}_{\mathbf{s},\psi_l}(-M+1,-M) & \mathbf{R}_{\mathbf{s},\psi_l}(-M+1,-M+1) & \mathbf{R}_{\mathbf{s},\psi_l}(-M+1,-M+2) & 0 & \\ 0 & \mathbf{R}_{\mathbf{s},\psi_l}(-M+2,-M+1) & \mathbf{R}_{\mathbf{s},\psi_l}(-M+2,-M+2) & \cdots & \\ \ddots & \ddots & \ddots & & \\ & \ddots & \ddots & \ddots & \\ \cdots & \cdots & \mathbf{R}_{\mathbf{s},\psi_l}(M-2,M-2) & \mathbf{R}_{\mathbf{s},\psi_l}(M-2,M-1) & 0 \\ \cdots & 0 & \mathbf{R}_{\mathbf{s},\psi_l}(M-1,M-2) & \mathbf{R}_{\mathbf{s},\psi_l}(M-1,M-1) & \mathbf{R}_{\mathbf{s},\psi_l}(M-1,M) \\ \cdots & 0 & 0 & \mathbf{R}_{\mathbf{s},\psi_l}(M,M-1) & \mathbf{R}_{\mathbf{s},\psi_l}(M,M) \end{bmatrix} \tag{2.12}$$

where

$$\mathbf{R}_{\mathbf{s},\psi_l}(n,m) = \left[\left\{ \begin{bmatrix} \rho_{xw}(n,m,\tau_{lw}-\widehat{\tau}_{lx}) & \cdots & \rho_{xw}(n,m,\tau_{lw}-\widehat{\tau}_{lx}+GT_c) \\ \vdots & \ddots & \vdots \\ \rho_{xw}(n,m,\tau_{lw}-\widehat{\tau}_{lx}-GT_c) & \cdots & \rho_{xw}(n,m,\tau_{lw}-\widehat{\tau}_{lx}) \end{bmatrix} \middle| \, x,w \in \psi_l \right\} \right] \tag{2.13}$$

and

$$\rho_{xk}(n,m,\tau) = \int_{-\infty}^{\infty} s^*_x(t-nT)\, s_k(t-mT-\tau)\, dt. \tag{2.14}$$

Since the transmitted waveforms for each user have support $[0,T]$, $\rho_{xk}(n,m,\tau) = 0$ for $|(m-n)T+\tau| \geq T$. Therefore, if we assume that $\max_k(\{\tau_{lk}\}) - \min_k(\{\tau_{lk}\}) + GT_c < T$, $\mathbf{R}_{\mathbf{s},\psi_l}(n,m) = 0$ for $|m-n| > 1$. Figs. 2.2 and 2.3 show the relevant integration periods between two users' transmitted waveforms. Specifically, for users x and w, where $\tau_{lw} > \tau_{lx}$, Fig.

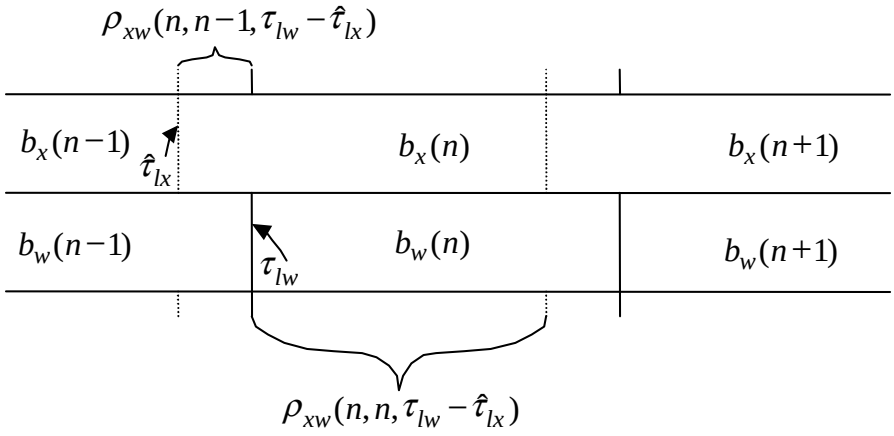

Figure 2.2: Integration periods for $\rho_{xw}\left(n, n-1, \tau_{lw} - \widehat{\tau}_{lx}\right)$ and $\rho_{xw}\left(n, n, \tau_{lw} - \widehat{\tau}_{lx}\right)$.

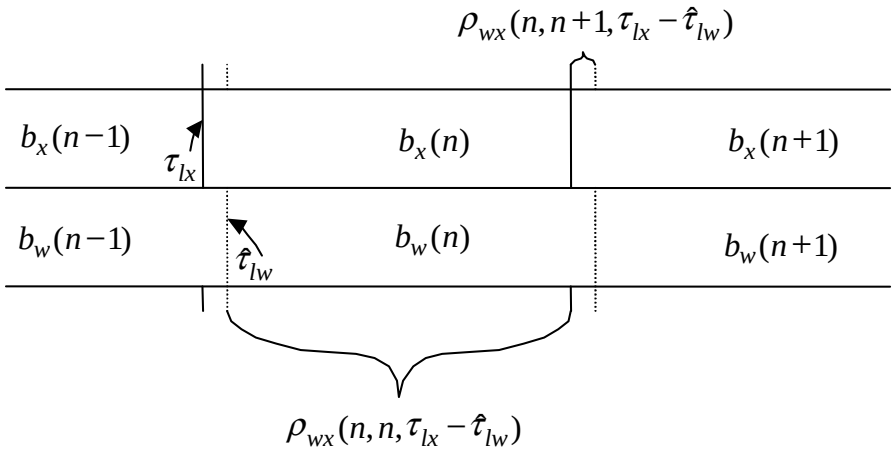

Figure 2.3: Integration periods for $\rho_{wx}\left(n, n, \tau_{lx} - \widehat{\tau}_{lw}\right)$ and $\rho_{wx}\left(n, n+1, \tau_{lx} - \widehat{\tau}_{lw}\right)$.

2.2 shows the integration periods for $\rho_{xw}(n, n-1, \tau_{lw} - \widehat{\tau}_{lx})$ and $\rho_{xw}(n, n, \tau_{lw} - \widehat{\tau}_{lx})$, and Fig. 2.3 shows the integration periods for $\rho_{wx}(n, n, \tau_{lx} - \widehat{\tau}_{lw})$ and $\rho_{wx}(n, n+1, \tau_{lx} - \widehat{\tau}_{lw})$.

As can be seen from (2.12), (2.13), and (2.14), the cross-correlations between the users' transmitted waveforms can vary with times n and m. This type of variation would occur with long spreading sequences that span several information symbols. Even though the effects of time-varying cross-correlations are not investigated in this thesis, the time dependence has been included for generality.

In (2.13), the braces are used again to show that $\mathbf{R}_{\mathbf{s},\psi_l}(n, m)$ is created with all values of x and w where $x, w \in \psi_l$. Changing x indexes the submatrices column-wise, while changing w indexes the submatrices row-wise. $\mathbf{R}_{\mathbf{s},\psi_l,\phi_l}(n, m)$ is formulated in a similar fashion by replacing w with u where $u \notin \psi_l$. The following section also uses the quantity, $\widehat{\mathbf{R}}_{\mathbf{s},\psi_l} = \int_{-\infty}^{\infty} \widehat{\mathbf{s}}^{*}_{\psi_l} \widehat{\mathbf{s}}^{\mathrm{T}}_{\psi_l} dt$. To create $\widehat{\mathbf{R}}_{\mathbf{s},\psi_l}$, the $\mathbf{R}_{\mathbf{s},\psi_l}(n, m)$ in (2.12) is replaced with $\widehat{\mathbf{R}}_{\mathbf{s},\psi_l}(n, m)$, and the τ_{lw} in (2.13) is replaced with $\widehat{\tau}_{lw}$. Therefore, even though $\mathbf{R}_{\mathbf{s},\psi_l}$ is generally non-Hermitian, by replacing the τ_{lw} in (2.13) with $\widehat{\tau}_{lw}$, $\widehat{\mathbf{R}}_{\mathbf{s},\psi_l}$ becomes a Hermitian matrix.

The following section describes how the above quantities are used in the ML-MUMD.

2.2 Maximum Likelihood Multiuser-Macrodiversity Detection

The ML multiuser-macrodiversity detector uses knowledge of the signal waveforms $\{s_x(t)\}$, estimates of the relative delays $\{\widehat{\tau}_{lx}\}$, and complex channel gain estimates $\{v_{lxg}(n)\}$ in order to decide on the transmitted data symbols in $\mathbf{B}_{\psi_l}$. A block diagram of the receiver is shown in Fig. 2.4. Assuming that the data symbols are equiprobable, and assuming that the macrodiversity antennas are spaced far enough apart to ensure independent fading, the ML multiuser-macrodiversity detector maximizes the following probability with respect to the data:

$$\prod_{l=1}^{L} P\left[\mathbf{y}_{\psi_l} | \mathbf{B}_{i,\psi_l}, \mathbf{v}_{\psi_l}, \widehat{\mathbf{s}}_{\psi_l}\right] = \frac{\exp\left[\frac{-1}{2} \sum_{l=1}^{L} \left((\mathbf{y}_{\psi_l} - \widehat{\mathbf{y}}_{\psi_l})^{\dagger} \mathbf{K}^{-1}_{\mathbf{y},\psi_l} (\mathbf{y}_{\psi_l} - \widehat{\mathbf{y}}_{\psi_l}) \right)\right]}{\prod_{l=1}^{L} (2\pi)^{N(G+1)K_{\psi_l}} \det(\mathbf{K}_{\mathbf{y},\psi_l})} \tag{2.15}$$

where $\dagger$ denotes the Hermitian transpose, $\widehat{\mathbf{y}}_{\psi_l} = \widehat{\mathbf{R}}_{\mathbf{s},\psi_l} \mathbf{B}_{i,\psi_l} \mathbf{v}_{\psi_l}$, and L is the number of antennas in the system including both microdiversity and macrodiversity antennas.

In (2.15), the subscript, i, in $\mathbf{B}_{i,\psi_l}$ is used to show that all possible data combinations in $\mathbf{B}_{i,\psi_l}$ are used in the decision process, and the detector selects the data which maximizes (2.15). The vector, $\mathbf{v}_{\psi_l}$, is

$$\mathbf{v}_{\psi_l} = \left[\mathbf{v}_{\psi_l}^{\mathrm{T}}(-M), ..., \mathbf{v}_{\psi_l}^{\mathrm{T}}(M)\right]^{\mathrm{T}} \tag{2.16}$$

where

$$\mathbf{v}_{\psi_l}(n) = \left[\left\{\left[v_{lx0}(n), ..., v_{lxG}(n)\right] | \, x \in \psi_l\right\}\right]^{\mathrm{T}} \tag{2.17}$$

where $x \in \psi_l$, and $v_{lxg}(n)$ is the estimate of the complex channel gain $c_{lxg}(n)$.

In (2.15), it is assumed that $P\left[\mathbf{y}_{\psi_l} | \mathbf{B}_{i,\psi_l}, \mathbf{v}_{\psi_l}, \widehat{\mathbf{s}}_{\psi_l}\right]$ is complex Gaussian. In fact, this probability is not strictly complex Gaussian. The users which are not involved in the ML-MUMD produce MAI, where the MAI portion of $\mathbf{y}_{\psi_l}$ is $\mathbf{R}_{\mathbf{s},\psi_l,\phi_l}\mathbf{B}_{\phi_l}\mathbf{c}_{\phi_l}$. The cross-correlations in $\mathbf{R}_{\mathbf{s},\psi_l,\phi_l}$ are binomial random variables with zero mean and variance $\sigma_s^2 = R/W$, where R/W is the inverse of the processing gain. Nevertheless, the summation over the large number of interfering signals results in a probability distribution which closely approximates a Gaussian distribution. Further, the fact that the code synchronization is imperfect also causes $P\left[\mathbf{y}_{\psi_l} | \mathbf{B}_{i,\psi_l}, \mathbf{v}_{\psi_l}, \widehat{\mathbf{s}}_{\psi_l}\right]$ to be non-Gaussian. However, since systems are designed to have a relatively small timing jitter, (2.15) is approximately Gaussian and can be used as the ML multiuser-macrodiversity detector.

The covariance matrix, $\mathbf{K}_{\mathbf{y},\psi_l}$, is given as:

$$\begin{aligned}
\mathbf{K}_{\mathbf{y},\psi_l} &= E\left[\left(\mathbf{y}_{\psi_l} - \widehat{\mathbf{y}}_{\psi_l}\right)\left(\mathbf{y}_{\psi_l} - \widehat{\mathbf{y}}_{\psi_l}\right)^{\dagger}\right] \\
&= \mathbf{R}_{\mathbf{s},\psi_l}\mathbf{B}_{\psi_l}\Omega_{\mathbf{c},\psi_l}\mathbf{B}_{\psi_l}^{\dagger}\mathbf{R}_{\mathbf{s},\psi_l}^{\dagger} \qquad (2.18) \\
&\quad + \widehat{\mathbf{R}}_{\mathbf{s},\psi_l}\mathbf{B}_{\psi_l}\Omega_{\mathbf{v},\psi_l}\mathbf{B}_{\psi_l}^{\dagger}\widehat{\mathbf{R}}_{\mathbf{s},\psi_l}^{\dagger} \\
&\quad - 2\,\mathrm{Re}\left[\mathbf{R}_{\mathbf{s},\psi_l}\mathbf{B}_{\psi_l}\Omega_{\mathbf{c},\mathbf{v},\psi_l}\mathbf{B}_{\psi_l}^{\dagger}\widehat{\mathbf{R}}_{\mathbf{s},\psi_l}^{\dagger}\right] \\
&\quad + \mathbf{R}_{\mathbf{s},\psi_l,\phi_l}\mathbf{B}_{\phi_l}\Omega_{\mathbf{c},\phi_l}\mathbf{B}_{\phi_l}^{\dagger}\mathbf{R}_{\mathbf{s},\psi_l,\phi_l}^{\dagger} + N_0\widehat{\mathbf{R}}_{\mathbf{s},\psi_l} \qquad (2.19)
\end{aligned}$$

where

$$\Omega_{\mathbf{c},\mathbf{v},\psi_l} = \begin{bmatrix} \boldsymbol{\xi}_{\mathbf{c},\mathbf{v},\psi_l}(0) & \cdots & \boldsymbol{\xi}_{\mathbf{c},\mathbf{v},\psi_l}(-2M) \\ \vdots & \ddots & \vdots \\ \boldsymbol{\xi}_{\mathbf{c},\mathbf{v},\psi_l}(2M) & \cdots & \boldsymbol{\xi}_{\mathbf{c},\mathbf{v},\psi_l}(0) \end{bmatrix}. \tag{2.20}$$

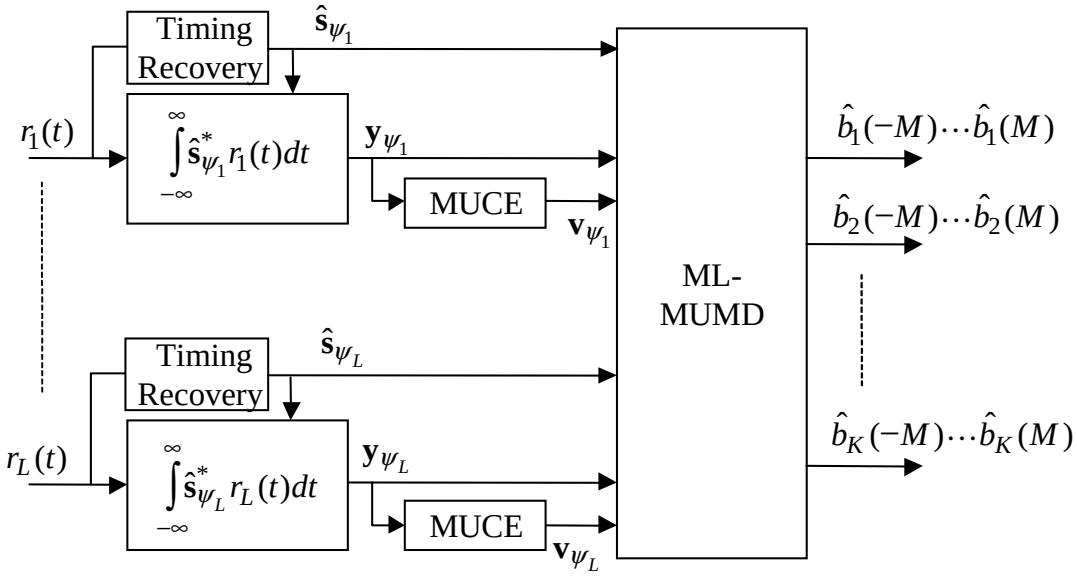

Figure 2.4: The ML-multiuser macrodiversity detector with multiuser channel estimation (MUCE).

In (2.20), $\boldsymbol{\xi}_{\mathbf{c},\mathbf{v},\psi_l}(m)$ is given as

$$\begin{aligned}\boldsymbol{\xi}_{\mathbf{c},\mathbf{v},\psi_l}(m) &= J_0(2\pi f_D T m)\cdot \\ &\quad diag\left(\{\eta_{lx0}\sigma_{c,lx0}\sigma_{v,lx0},...,\eta_{lxG}\sigma_{c,lxG}\sigma_{v,lxG}|\, x\in\psi_l\}\right) \qquad (2.21)\end{aligned}$$

where η_{lxg} is the correlation coefficient between the complex channel gain $c_{lxg}(n)$ and the channel estimate $v_{lxg}(n)$.

In (2.19), $\Omega_{\mathbf{c},\psi_l}$ and $\Omega_{\mathbf{v},\psi_l}$ are equivalent to $\Omega_{\mathbf{c},\mathbf{c},\psi_l}$ and $\Omega_{\mathbf{v},\mathbf{v},\psi_l}$ respectively. Similarly $\boldsymbol{\xi}_{\mathbf{c},\psi_l}(m) = \boldsymbol{\xi}_{\mathbf{c},\mathbf{c},\psi_l}(m) = J_0(2\pi f_D T m)\cdot diag\left(\left\{\sigma^2_{c,lx0},...,\sigma^2_{c,lxG}\middle|\, x\in\psi_l\right\}\right)$. On the last line of (2.19), we also see the term $\Omega_{\mathbf{c},\phi_l}$. In order to create $\Omega_{\mathbf{c},\phi_l}$, the $\boldsymbol{\xi}_{\mathbf{c},\psi_l}(m)$ in $\Omega_{\mathbf{c},\psi_l}$ is replaced with $\boldsymbol{\xi}_{\mathbf{c},\phi_l}(m)$ by substituting the x with u where $u\notin\psi_l$.

Since $z_l(t)$ is a white Gaussian noise process, the second order statistics of $\mathbf{z}_{\psi_l}$ depend only on the receiver's matched filters. Therefore, as can be seen in (2.19), $E\left[\mathbf{z}_{\psi_l}\mathbf{z}^\dagger_{\psi_l}\right] = N_o\widehat{\mathbf{R}}_{\mathbf{s},\psi_l}$.

The current difficulty with maximizing (2.15) is that it requires knowledge of $\mathbf{K}_{\mathbf{y},\psi_l}$. The $\mathbf{K}_{\mathbf{y},\psi_l}$ in (2.19) must be estimated in order to use it in (2.15). In its current format $\mathbf{K}_{\mathbf{y},\psi_l}$ contains unknown quantities. For example, at the receiver, we do not have knowledge of

$\mathbf{s}_{\psi_l}$; we only have knowledge of $\widehat{\mathbf{s}}_{\psi_l}$. Therefore, the $\mathbf{R}_{\mathbf{s},\psi_l}$ in (2.19) would need to be replaced with $\widehat{\mathbf{R}}_{\mathbf{s},\psi_l}$. In addition to this, we have no knowledge whatsoever of $\mathbf{R}_{\mathbf{s},\psi_l,\phi_l}$ since it includes the set of users which produce MAI. By assuming that the MAI at antenna l is modeled as white noise, and that the interference generated by the imperfect channel estimates is negligible when compared to the combination of the MAI with the thermal noise, $\mathbf{K}_{\mathbf{y},\psi_l}$ can be estimated as

$$\widehat{\mathbf{K}}_{\mathbf{y},\psi_l} = (I_{o_l} + N_o)\,\widehat{\mathbf{R}}_{\mathbf{s},\psi_l} \tag{2.22}$$

where $I_{o_l} + N_o$ is an estimate of the interference and noise power at antenna l. Here it is assumed that

$$I_{o_l} = \sigma_s^2 \sum_u A_u^2 \left|b_u\left(n\right)\right|^2 \sum_{g=0}^{G} \sigma_{c,lug}^2 \tag{2.23}$$

where $u \notin \psi_l$, $\sigma_s^2 = R/W$ (i.e. the inverse of the processing gain), and $\left|b_u\left(n\right)\right|^2 = 1$ for a BPSK system.

By replacing $\mathbf{K}_{\mathbf{y},\psi_l}^{-1}$ in (2.15) with $\widehat{\mathbf{K}}_{\mathbf{y},\psi_l}^{-1}$, noting that $\widehat{\mathbf{R}}_{\mathbf{s},\psi_l} = \widehat{\mathbf{R}}_{\mathbf{s},\psi_l}^{\dagger}$, and neglecting the hypothesis independent terms in (2.15), we can minimize the equivalent log-likelihood function, λ_i.

$$\lambda_i = \sum_{l=1}^{L} \lambda_{il} \tag{2.24}$$

where

$$\lambda_{il} = \frac{\mathbf{v}_{\psi_l}^{\dagger}\mathbf{B}_{i,\psi_l}^{\dagger}\widehat{\mathbf{R}}_{\mathbf{s},\psi_l}\mathbf{B}_{i,\psi_l}\mathbf{v}_{\psi_l} - 2\,\mathrm{Re}\left[\mathbf{y}_{\psi_l}^{\dagger}\mathbf{B}_{i,\psi_l}\mathbf{v}_{\psi_l}\right]}{I_{o_l} + N_o}. \tag{2.25}$$

Therefore, λ_{il} is summed over all of the antennas in the system to determine the N transmitted data symbols from each of the K users in the system. At first glance it appears as if we have to minimize (2.24) over all 2^{NK} combinations. However, this would be impractical as it is far too computationally complex. As a result of the fact that we have different subsets of users at each antenna, the ML solution can be achieved with less effort by performing a conditional joint detection on each user/antenna combination separately and by combining the appropriate metrics in an efficient way.

In [2], Verdu showed that the original ML multiuser detector could be implemented with a number of single-user matched filters followed by a Viterbi algorithm. He was able

to implement the multiuser detector in this fashion by showing that the appropriate metric could be separated into a sum of terms that depend on a few symbols at a time.

The Viterbi algorithm is a temporal algorithm, and consequently it cannot be applied to ML-MUMD. As a result of the overlapping sets of users at the various macrodiversity antennas, the ML multiuser-macrodiversity detector is required to operate in both space and time. However, similar to the multiuser detector in [2], λ_i for the ML multiuser-macrodiversity detector can also be rewritten so that it is composed of sums of terms that depend on only a few symbols per algorithm stage, where each stage of the algorithm defines a particular point in space and time. By noting that $\widehat{\mathbf{R}}_{\mathbf{s},\psi_l}(n,m) = 0$ for $|m-n| > 1$, λ_{il} in (2.25) can be rewritten as

$$\begin{aligned}\lambda_{il} &= \frac{1}{I_{o_l}+N_o}\left(\sum_{n=-M}^{M}\left(\sum_{m=-1}^{1}\mathbf{v}_{\psi_l}^{\dagger}(n)\,\mathbf{B}_{i,\psi_l}^{\dagger}(n)\,\widehat{\mathbf{R}}_{\mathbf{s},\psi_l}(n,n+m)\,\mathbf{B}_{i,\psi_l}(n+m)\,\mathbf{v}_{\psi_l}(n+m)\right)\right. \\ &\quad \left.-2\,\mathrm{Re}\left[\mathbf{y}_{\psi_l}^{\dagger}(n)\,\mathbf{B}_{i,\psi_l}(n)\,\mathbf{v}_{\psi_l}(n)\right]\right) \qquad (2.26)\end{aligned}$$

where the λ_{il} in (2.26) depends on past, current, and future data symbols since m takes values from -1 to $+1$. As a result of the fact that $\widehat{\mathbf{R}}_{\mathbf{s},\psi_l}(n,m) = \widehat{\mathbf{R}}_{\mathbf{s},\psi_l}^{\dagger}(m,n)$, the following symmetry occurs between the past and future data symbols:

$$\begin{aligned}&\mathbf{v}_{\psi_l}^{\dagger}(n)\,\mathbf{B}_{i,\psi_l}^{\dagger}(n)\,\widehat{\mathbf{R}}_{\mathbf{s},\psi_l}(n,n-1)\,\mathbf{B}_{i,\psi_l}(n-1)\,\mathbf{v}_{\psi_l}(n-1) = \\ &\left[\mathbf{v}_{\psi_l}^{\dagger}(n-1)\,\mathbf{B}_{i,\psi_l}^{\dagger}(n-1)\,\widehat{\mathbf{R}}_{\mathbf{s},\psi_l}(n-1,n)\,\mathbf{B}_{i,\psi_l}(n)\,\mathbf{v}_{\psi_l}(n)\right]^{\dagger}. \qquad (2.27)\end{aligned}$$

Therefore, (2.26) can be rewritten so that λ_{il} depends on only past and current data symbols as shown below.

$$\begin{aligned}\lambda_{il} &= \frac{1}{I_{o_l}+N_o}\left(\sum_{n=-M}^{M}\mathbf{v}_{\psi_l}^{\dagger}(n)\,\mathbf{B}_{i,\psi_l}^{\dagger}(n)\,\widehat{\mathbf{R}}_{\mathbf{s},\psi_l}(n,n)\,\mathbf{B}_{i,\psi_l}(n)\,\mathbf{v}_{\psi_l}(n)\,+\right. \\ &\quad 2\,\mathrm{Re}\left[\mathbf{v}_{\psi_l}^{\dagger}(n)\,\mathbf{B}_{i,\psi_l}^{\dagger}(n)\,\widehat{\mathbf{R}}_{\mathbf{s},\psi_l}(n,n-1)\,\mathbf{B}_{i,\psi_l}(n-1)\,\mathbf{v}_{\psi_l}(n-1)\,-\right. \\ &\quad \left.\left.\mathbf{y}_{\psi_l}^{\dagger}(n)\,\mathbf{B}_{i,\psi_l}(n)\,\mathbf{v}_{\psi_l}(n)\right]\right). \qquad (2.28)\end{aligned}$$

By using the fact that $\rho_{xw}(n,n-1,\widehat{\tau}_{lw}-\widehat{\tau}_{lx}) = 0$ for $\widehat{\tau}_{lw} \le \widehat{\tau}_{lx}$, further manipulation of (2.28) reveals that λ_i in (2.24) can be rewritten as follows:

$$\lambda_i = \sum_{n=-M}^{M}\sum_{l=1}^{L}\sum_{x\in\psi_l}\lambda_{ilx}(n) \qquad (2.29)$$

where

$$\begin{aligned}
\lambda_{ilx}(n) &= \frac{1}{I_{o_l}+N_o}\cdot\Bigg(|A_x|^2\,|b_{i,x}(n)|^2\,\rho_{xx}(n,n,0)\sum_{j=0}^{G}|v_{lxj}(n)|^2+\\
&\quad 2\,\mathrm{Re}\Big[|A_x|^2\,b_{i,x}^*(n)\,b_{i,x}(n-1)\cdot\\
&\quad \sum_{j=0}^{G}\sum_{g=j+1}^{G}\rho_{xx}(n,n-1,(g-j)\,T_c)\,v_{lxj}^*(n)\,v_{lxg}(n-1)+\\
&\quad A_x^*b_{i,x}^*(n)\sum_{\{w\in\psi_l|\widehat{\tau}_{lw}>\widehat{\tau}_{lx}\}}A_w b_{i,w}(n-1)\cdot\\
&\quad \sum_{j=0}^{G}\sum_{g=0}^{G}\rho_{xw}(n,n-1,\widehat{\tau}_{lw}-\widehat{\tau}_{lx}+(g-j)\,T_c)\,v_{lxj}^*(n)\,v_{lwg}(n-1)+\\
&\quad A_x^*b_{i,x}^*(n)\sum_{\{w\in\psi_l|\widehat{\tau}_{lw}\le\widehat{\tau}_{lx},w\neq x\}}A_w b_{i,w}(n)\cdot\\
&\quad \sum_{j=0}^{G}\sum_{g=0}^{G}\rho_{xw}(n,n,\widehat{\tau}_{lw}-\widehat{\tau}_{lx}+(g-j)\,T_c)\,v_{lxj}^*(n)\,v_{lwg}(n)+\\
&\quad |A_x|^2\,|b_{i,x}(n)|^2\sum_{j=0}^{G}\sum_{g=0}^{j-1}\rho_{xx}(n,n,(g-j)\,T_c)\,v_{lxj}^*(n)\,v_{lxg}(n)-\\
&\quad A_x b_{i,x}(n)\sum_{j=0}^{G}y_{lxj}^*(n)\,v_{lxj}(n)\Big]\Bigg).
\end{aligned}\tag{2.30}$$

In the absence of ISI and macrodiversity, (2.29) and (2.30) reduce to the metric for the original ML multiuser detector in [2]. As can be seen from (2.30), $\lambda_{ilx}(n)$ depends only on the following $K_{\psi_l}+1$ information symbols, $\{b_x(n-1),\{b_w(n-1)|\,w\in\psi_l,\widehat{\tau}_{lw}>\widehat{\tau}_{lx}\},\ \{b_w(n)|\,w\in\psi_l,\widehat{\tau}_{lw}\le\widehat{\tau}_{lx}\}\}$.

Therefore, even though the general structure of the ML multiuser-macrodiversity detector in (2.24) and (2.25) includes interference from past, current and future data symbols, by taking advantage of the fact that $\widehat{\mathbf{R}}_{\mathbf{s},\psi_l}(n,m)=0$ for $|m-n|>1$, that $\widehat{\mathbf{R}}_{\mathbf{s},\psi_l}(n,m)=\widehat{\mathbf{R}}_{\mathbf{s},\psi_l}^{\dagger}(m,n)$ and that $\rho_{xw}(n,n-1,\widehat{\tau}_{lw}-\widehat{\tau}_{lx})=0$ for $\widehat{\tau}_{lw}\le\widehat{\tau}_{lx}$, the ML multiuser- macrodiversity detector separates into sums of terms where each term, $\lambda_{ilx}(n)$, depends on only a select few of the past and current data symbols. As a result of the structure in (2.30), the complexity per stage of the algorithm reduces to $2^{K_{\psi_l}+1}$ for BPSK signals.

Now that λ_i has been rewritten so that each term, $\lambda_{ilx}(n)$, depends only on $K_{\psi_l}+1$

information symbols per stage, the Conditional Metric Merge (CMM) algorithm is presented which combines the metrics, $\lambda_{ilx}(n)$, in such a way that it keeps the computational complexity of the ML-MUMD to a minimum.

Chapter 3

Conditional Metric Merge Algorithm

Similar to the Viterbi algorithm, the CMM algorithm is in the general class of dynamic programming algorithms. In order to be able to utilize a dynamic programming technique, an optimization problem must have both an optimal substructure and overlapping subproblems [64]. A problem has an optimal substructure if its optimal solution is composed of optimal solutions to subproblems [64]. As can be seen in the previous section, the ML multiuser-macrodiversity detector exhibits an optimal substructure since the minimization of (2.30) is an optimal solution to a subproblem within (2.29). The ML multiuser-macrodiversity detector also has overlapping subproblems since the metrics, $\lambda_{ilx}(n)$, include different, but often overlapping, sets of users in the MUMD. Therefore, the CMM algorithm utilizes a dynamic programming approach to reduce the number of computations required to perform the MUMD.

The CMM algorithm is actually an extension of the Viterbi algorithm into the spatial domain. In fact, if all of the users' signals arrived at each macrodiversity antenna with similar relative delays, and the signals were detected by all of the macrodiversity antennas, the CMM algorithm would reduce to the Viterbi algorithm. In contrast, in a synchronous CDMA system with no intersymbol interference (ISI), the CMM algorithm reduces to a purely spatial form of the algorithm, which has not appeared in the literature to date. When the ML multiuser-macrodiversity detector operates in an asynchronous CDMA system with or without ISI, the more general CMM algorithm applies dynamic programming in both

space and time.

Since $\lambda_{ilx}(n)$ in (2.30) depends on the following $K_{\psi_l}+1$ information symbols, $\{b_x(n-1), \{b_w(n-1)|\, w \in \psi_l, \widehat{\tau}_{lw} > \widehat{\tau}_{lx}\}, \{b_w(n)|\, w \in \psi_l, \widehat{\tau}_{lw} \leq \widehat{\tau}_{lx}\}\}$, the number of probabilities calculated per stage of the algorithm is $2^{K_{\psi_l}+1}$. However, since each user may be connected to a different number of antennas, the complexity per binary decision is variable. For example, if user x is connected to the antennas in $\mathcal{A}_x$, where $\mathcal{A}_x$ is user x's active set, the number of probabilities calculated per binary decision for user x is $\sum_{l\in\mathcal{A}_x} 2^{K_{\psi_l}+1}$. It is important to note that if we were to consider a system with no ISI, $\lambda_{ilx}(n)$ would depend on only K_{ψ_l} information symbols since we would no longer need to include $b_{i,x}(n-1)$ in (2.30). Therefore, for a system with no ISI, the complexity per binary decision would be $\sum_{l\in\mathcal{A}_x} 2^{K_{\psi_l}}$. However, for generality, we will continue to assume that ISI is present in the system.

In order to describe the CMM algorithm, an index variable is used to identify a particular point in space and time. The index variable, h, is defined as

$$h = (n+M)\sum_{l'=1}^{L} K_{\psi_{l'}} + \sum_{l'=1}^{l-1} K_{\psi_{l'}} + j \tag{3.1}$$

where $1 \leq h \leq N\left(\sum_{l'=1}^{L} K_{\psi_{l'}}\right)$, $-M \leq n \leq M$, $1 \leq l \leq L$, and $1 \leq j \leq K_{\psi_l}$. Therefore, each integer, h, defines a particular time n, antenna l, and user $x = \psi_{l,j}$, where $\psi_{l,j}$ denotes the j^{th} entry in the set, ψ_l. As can be seen in (3.1), the user changes most rapidly with h, followed by the antenna, and finally the time changes slowly with h.

Since h defines a specific time n, antenna l and user x, the data symbols that are included in the metric, $\lambda_{ilx}(n)$, in (2.30) are stored in the set

$$\Psi(h) = \left\{ \begin{array}{c} b_x(n-1), \{b_w(n-1)|\, w \in \psi_l, \widehat{\tau}_{lw} > \widehat{\tau}_{lx}\}, \\ \{b_w(n)|\, w \in \psi_l, \widehat{\tau}_{lw} \leq \widehat{\tau}_{lx}\} \end{array} \right\} \tag{3.2}$$

where the data symbols involved do not change with i, $|\Psi(h)| = K_{\psi_l}+1$, and $|\cdot|$ applied to a set denotes the length of the set.

Now that the index variable, h, and the data symbol sets, $\Psi(h)$, have been introduced, a short example will be used to show how the time, antenna, and user vary with h, and how the corresponding data symbol sets, $\Psi(h)$ are formed. The example is based on the connections for the $K = 2$ users and $L = 2$ antennas depicted in Fig. 3.1. As can be seen from the figure, user 1, U1, is communicating with antenna 1, A1, only, while user 2, U2, is communicating with both antennas 1 and 2, A1 and A2. Table 3.1 uses the connections in

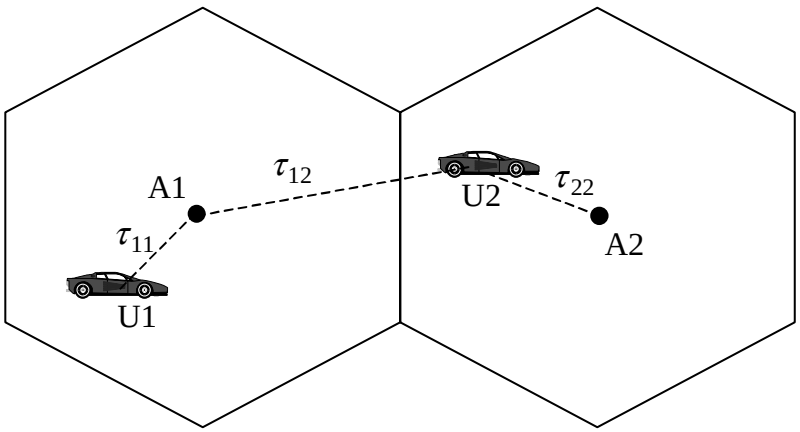

Figure 3.1: Typical connections for 2 users and 2 antennas.

Fig. 3.1 to relate each specific value of h to a particular time, antenna, and user according to the relation in (3.1). As noted above, it can be observed from the table that the user varies most rapidly with h, followed by the antenna, and finally by the time.

In Fig. 3.1, each transmission delay, τ_{lk}, between the k^{th} user and the l^{th} antenna is shown beside the appropriate link, and in this example, it is assumed that $\tau_{11} < \tau_{12}$. The relative transmission delays must be known in order to create the data symbol sets as shown in (3.2). While the relative delays affect the data symbols that appear in the set, $\Psi(h)$, the ordering of the data symbols within the set is independent of the transmission delays and corresponds with the ordering $\{b_1(-M), ..., b_K(-M), ..., b_1(M), ..., b_K(M)\}$. By using (3.2), it can be observed that the data set for A1 and U1 at time n is $\{b_1(n-1), b_2(n-1), b_1(n)\}$, the data set for A1 and U2 at time n is $\{b_2(n-1), b_1(n), b_2(n)\}$, and the data set for A2 and U2 at time n is $\{b_2(n-1), b_2(n)\}$. The data symbol sets, $\Psi(h)$, in Table 3.1 are similar to those described above and are formed using (3.2). The $\{b_k(-M-1)\}$ in Table 3.1 have been excluded from $\Psi(h)$ for $h = 1, 2$, and 3 since $b_k(n) = 0$ for $n < -M$.

Now that this example has illustrated how the index variable, h, and the data symbol sets, $\Psi(h)$ are formed in a typical system, the following paragraphs introduce the metrics, $\Lambda(h)$, that correspond with the data symbol sets, $\Psi(h)$.

The metric, $\lambda_{ilx}(n)$, is calculated for all values of the data symbols in $\Psi(h)$. If we define $\alpha = \{0, 1\}$ as the alphabet for a BPSK signal, there are $|\alpha|^{|\Psi(h)|} = 2^{K_{\psi_l}+1}$ possible combinations of the data symbol values in $\Psi(h)$ and thus $2^{K_{\psi_l}+1}$ metric calculations. The

h	n (Time)	l (Antenna)	x (User)	$\Psi(h)$ (Data symbols in the metric, $\lambda_{ilx}(n)$)
1	$-M$	1	1	$\{b_1(-M)\}$
2	$-M$	1	2	$\{b_1(-M), b_2(-M)\}$
3	$-M$	2	2	$\{b_2(-M)\}$
4	$-M+1$	1	1	$\{b_1(-M), b_2(-M), b_1(-M+1)\}$
5	$-M+1$	1	2	$\{b_2(-M), b_1(-M+1), b_2(-M+1)\}$
6	$-M+1$	2	2	$\{b_2(-M), b_2(-M+1)\}$
7	$-M+2$	1	1	$\{b_1(-M+1), b_2(-M+1), b_1(-M+2)\}$
$\vdots$	$\vdots$	$\vdots$	$\vdots$	$\vdots$

Table 3.1: Initializations for the connections shown in Fig. 3.1

metrics that are calculated for all of the various data symbol values in $\Psi(h)$ are stored in the set

$$\Lambda(h) = \left\{ \lambda_{ilx}(n) |\, i = 1, ..., |\alpha|^{|\Psi(h)|} \right\}. \tag{3.3}$$

The metrics at each stage of the algorithm can be merged by using the Combine routine. If we define $\mathbf{h} = [1, ..., h]$, the combined metrics may be expressed as

$$\Lambda(\mathbf{h}) = \Lambda(\mathbf{f}) \textcircled{\Sigma} \Lambda(h) \tag{3.4}$$

where $\mathbf{f} = [1, ..., h-1]$ and $\textcircled{\Sigma}$ represents the invoked Combine routine. The Combine routine is analogous to metric extension in the Viterbi algorithm where the computed metrics form continuations on the surviving sequences from the previous stage [15]. The following section describes how the Combine routine merges the two different sets of metrics, $\Lambda(\mathbf{f})$ and $\Lambda(h)$.

3.1 The Combine Routine

This section provides a description of the Combine routine in 3.1.1, and it also provides a practical example of this routine in 3.1.2.

3.1.1 The Combine Routine's Description

In this routine, we combine the metrics, $\Lambda(\mathbf{f})$ and $\Lambda(h)$. The data symbols that correspond with $\Lambda(\mathbf{f})$ and $\Lambda(h)$ are given by $\Psi(\mathbf{f})$ and $\Psi(h)$ respectively. In the atypical situation where $\Psi(\mathbf{f}) = \Psi(h)$, $\Lambda(\mathbf{h}) = \Lambda(\mathbf{f}) \textcircled{\Sigma} \Lambda(h)$ can be performed by simply adding

the respective metrics within each set. However, normally $\Psi(\mathbf{f}) \neq \Psi(h)$. Therefore, we create $\Psi(\mathbf{h}) = \Psi(\mathbf{f}) \cup \Psi(h)$, and we repeat the metrics in $\Lambda(\mathbf{f})$ and $\Lambda(h)$ in a manner so that they correspond with $\Psi(\mathbf{h})$. In order to repeat the metrics, we use the function, $I_w = repindex(\Psi(w), \Psi(\mathbf{h}))$ for both $w = \mathbf{f}$ and $w = h$. The returned set, I_w, contains the relevant indices in $\Psi(\mathbf{h})$ of the elements in $\Psi(\mathbf{h}) - \Psi(w)$. Once we have I_w for both $w = \mathbf{f}$ and $w = h$, we can use this information to repeat the metrics in $\Lambda(\mathbf{f})$ and $\Lambda(h)$ so that $|\Lambda(\mathbf{f})| = |\Lambda(h)| = |\alpha|^{|\Psi(\mathbf{h})|}$, and the sets can be merged by simply adding the respective metrics. This type of repetition can be performed since the metrics in $\Lambda(\mathbf{f})$ depend only on the data symbols in $\Psi(\mathbf{f})$; as a consequence, the data symbols in $\Psi(\mathbf{h}) - \Psi(\mathbf{f})$ have no effect on the metrics in $\Lambda(\mathbf{f})$. Similarly, the metrics in $\Lambda(h)$ depend only on the data symbols in $\Psi(h)$; thus, the data symbols in $\Psi(\mathbf{h}) - \Psi(h)$ have no effect on the metrics in $\Lambda(h)$.

In order to repeat the metrics in $\Lambda(w)$, we use the elements in I_w which are given by $I_{w,j}$ where $1 \leq j \leq |I_w|$. By starting with $j = 1$ and working toward $j = |I_w|$, we repeat the metrics in $\Lambda(w)$ as follows. The metrics are sequentially divided into $|\alpha|^{|\Psi(w)|+j-I_{w,j}}$ groups, and each group of $|\alpha|^{I_{w,j}-1}$ metrics is repeated so that it appears twice in succession. Therefore, within the Combine routine, the metrics, $\Lambda(w)$, that initially correspond with $\Psi(w)$ are repeated so that they correspond with $\Psi(\mathbf{h})$. Once this repetition is performed for both $w = \mathbf{f}$ and $w = h$, $\Lambda(\mathbf{h}) = \Lambda(\mathbf{f}) \textcircled{\Sigma} \Lambda(h)$ is easily calculated, and the Combine routine returns both $\Lambda(\mathbf{h})$ and $\Psi(\mathbf{h})$.

3.1.2 Example of the Combine Routine

The inputs to the Combine routine are the data symbol sets, $\Psi(\mathbf{f})$ and $\Psi(h)$, and their corresponding metrics, $\Lambda(\mathbf{f})$ and $\Lambda(h)$ respectively. Suppose the Combine routine is initialized for users 4 and 6 at times $n-1$ and n with the following data symbol sets

$$\Psi(\mathbf{f}) = \{b_4(n-1), b_6(n-1)\} \tag{3.5}$$

$$\Psi(h) = \{b_6(n-1), b_6(n)\} \tag{3.6}$$

and the metrics in Figures 3.2 and 3.3, where $\alpha^{|\Psi(w)|}$ denotes $|\Psi(w)|$ cross products on the set α [65]. As before, the ordering of the data symbols within the sets corresponds with $\{b_1(-M), ..., b_K(-M), ..., b_1(M), ..., b_K(M)\}$. In Figure 3.2, $\alpha^{|\Psi(\mathbf{f})|}$ lists all possible combinations of the data symbol values in $\Psi(\mathbf{f})$, and the metrics in $\Lambda(\mathbf{f})$ are calculated for each corresponding entry of $\alpha^{|\Psi(\mathbf{f})|}$. Normally the metrics are calculated using (2.30).

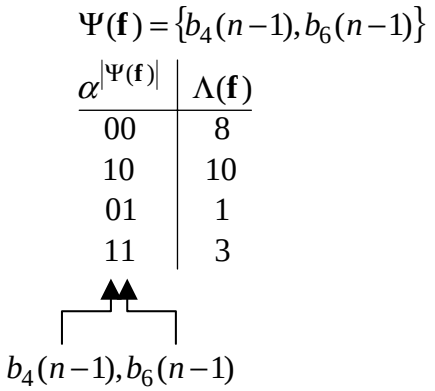

Figure 3.2: Sample metrics for $\Lambda(\mathbf{f})$.

However, in this example, the actual metrics are replaced with integers for simplicity. In a similar manner to that described above, $\alpha^{|\Psi(h)|}$ in Figure 3.3 lists all possible combinations of the data symbol values in $\Psi(h)$, and each entry of $\alpha^{|\Psi(h)|}$ is used to calculate the metrics in $\Lambda(h)$.

Now that the data symbol sets and their corresponding metrics have been defined, the *repindex* function is used to provide the proper repetition for both $\Lambda(\mathbf{f})$ and $\Lambda(h)$. The function, $I_w = repindex(\Psi(w), \Psi(\mathbf{h}))$ returns the relevant indices in $\Psi(\mathbf{h})$ of the elements in $\Psi(\mathbf{h}) - \Psi(w)$ for both $w = \mathbf{f}$ and $w = h$. $\Psi(\mathbf{h})$ is simply the union of the sets, $\Psi(\mathbf{f})$ and $\Psi(h)$. Therefore,

$$\Psi(\mathbf{h}) = \Psi(\mathbf{f}) \cup \Psi(h) = \{b_4(n-1), b_6(n-1), b_6(n)\}. \tag{3.7}$$

From (3.5) and (3.6), we calculate

$$\Psi(\mathbf{h}) - \Psi(\mathbf{f}) = \{b_6(n)\} \tag{3.8}$$

$$\Psi(\mathbf{h}) - \Psi(h) = \{b_4(n-1)\} \tag{3.9}$$

Therefore,

$$I_{\mathbf{f}} = repindex(\Psi(\mathbf{f}), \Psi(\mathbf{h})) = \{3\} \tag{3.10}$$

and

$$I_h = repindex(\Psi(h), \Psi(\mathbf{h})) = \{1\}. \tag{3.11}$$

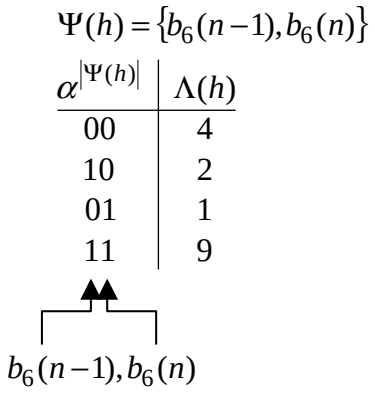

Figure 3.3: Sample metrics for $\Lambda(h)$.

In other words, counting from left to right, the symbol $b_6(n)$ in $\Psi(\mathbf{h}) - \Psi(\mathbf{f})$ appears in position $I_{\mathbf{f}} = \{3\}$ of $\Psi(\mathbf{h})$, and the symbol $b_4(n-1)$ in $\Psi(\mathbf{h}) - \Psi(h)$ appears in position $I_h = \{1\}$ of $\Psi(\mathbf{h})$. Now that $I_{\mathbf{f}}$ and I_h have been calculated, they will be used to repeat the metrics in $\Lambda(\mathbf{f})$ and $\Lambda(h)$ so that $|\Lambda(\mathbf{f})| = |\Lambda(h)| = |\alpha|^{|\Psi(\mathbf{h})|}$.

As stated previously, the metrics in $\Lambda(w)$ for both $w = \mathbf{f}$ and $w = h$ are sequentially divided into $|\alpha|^{|\Psi(w)|+j-I_{w,j}}$ groups, and each group of $|\alpha|^{I_{w,j}-1}$ metrics is repeated so that it appears twice in succession. Since $|I_{\mathbf{f}}| = |I_h| = 1$ in this example, only one repetition is needed for both $\Lambda(\mathbf{f})$ and $\Lambda(h)$, and j attains a maximum value of 1 for both $w = \mathbf{f}$ and $w = h$.

The metrics in $\Lambda(\mathbf{f})$ are divided into $|\alpha|^{|\Psi(\mathbf{f})|+j-I_{\mathbf{f},j}} = 2^{2+1-3} = 1$ group of $|\alpha|^{I_{\mathbf{f},j}-1} = 2^{3-1} = 4$ metrics, and this group is repeated so that the metrics appear as shown in $\Lambda(\mathbf{f})$ of Figure 3.4. Similarly, the metrics in $\Lambda(h)$ are divided into $|\alpha|^{|\Psi(h)|+j-I_{h,j}} = 2^{2+1-1} = 4$ groups of $|\alpha|^{I_{h,j}-1} = 2^{1-1} = 1$ metric, and these groups are each repeated so that they appear twice in succession as shown in $\Lambda(h)$ of Figure 3.4. As can be seen from Figure 3.4, $|\Lambda(\mathbf{f})| = |\Lambda(h)| = |\alpha|^{|\Psi(\mathbf{h})|}$ as expected, and $\Lambda(\mathbf{h})$ can now be calculated by simply adding the respective metrics within $\Lambda(\mathbf{f})$ and $\Lambda(h)$.

It is observed that $\Psi(\mathbf{h})$ may contain data symbols that do not appear in any of the subsequent data symbol sets, $\Psi(k)$ for $k > h$. If this is the case, we can discard the least-probable metrics with respect to these data symbols in the Select routine. The Select routine is analogous to the selection process in the Viterbi algorithm where the sequences

$\Psi(\mathbf{h}) = \{b_4(n-1), b_6(n-1), b_6(n)\}$

$\alpha^{\lvert\Psi(\mathbf{h})\rvert}$	$\Lambda(\mathbf{f})$	$\Lambda(h)$	$\Lambda(\mathbf{h})$
000	8	4	12
100	10	4	14
010	1	2	3
110	3	2	5
001	8	1	9
101	10	1	11
011	1	9	10
111	3	9	12

$b_4(n-1), b_6(n-1), b_6(n)$

Figure 3.4: The merging of sample metrics, $\Lambda(\mathbf{f})$ and $\Lambda(h)$.

are subdivided into groups that differ only in the symbol which is not involved in any subsequently received signals. From each group, the surviving sequence is the one having the largest probability, and the rest are discarded [15].

3.2 The Select Routine

This section describes the Select routine in 3.2.1, and a practical example is provided in 3.2.2 which further portrays the functionality of this routine.

3.2.1 The Select Routine's Description

We can make tentative decisions on the data symbols in the set

$$\Theta(h) = \Psi(\mathbf{h}) - \bigcup_{k>h} \Psi(k) \tag{3.12}$$

since the symbols in $\Theta(h)$ do not appear in any of the subsequent data symbol sets, $\Psi(k)$ for $k > h$. The elements in $\Theta(h)$ are given by $\Theta_j(h)$ where $1 \leq j \leq |\Theta(h)|$. Assuming that we start with $j = 1$ and work toward $j = |\Theta(h)|$, we can make a tentative decision on $\Theta_j(h)$

by dividing the $|\alpha|^{|\Psi(\mathbf{h})|-j+1}$ metrics into $|\alpha|^{|\Psi(\mathbf{h})|-j}$ groups with each group containing $|\alpha|$ metrics that differ in the symbol $\Theta_j(h)$. From each group of the $|\alpha|$ metrics, we select the minimum and discard the remaining $|\alpha|-1$ metrics. In a similar way to the Viterbi algorithm, the decision for $\Theta_j(h)$ is final if all of the groups make the same decision. Otherwise the decision for $\Theta_j(h)$ remains tentative and is deferred to a later stage. Once tentative decisions have been made on all of the symbols in $\Theta(h)$, the number of metrics in $\Lambda(\mathbf{h})$ has been reduced by a factor of $|\alpha|^{|\Theta(h)|}$, and $\Psi(\mathbf{h})$ is replaced by $\Psi(\mathbf{h})-\Theta(h)$. In total, we have made tentative decisions on the data symbols in $\Theta(\mathbf{h})=\bigcup_{1\leq j\leq h}\Theta(j)$, and these tentative decisions are stored in $D(\mathbf{h})$, where each entry of $D(\mathbf{h})$ contains $|\Theta(\mathbf{h})|$ tentative decisions, and the entire set has $|\alpha|^{|\Psi(\mathbf{h})|}$ entries.

3.2.2 Example of the Select Routine

The outputs of the Combine routine are used as inputs for the Select routine. From the example in Section 3.1.2, the data set, $\Psi(\mathbf{h})$ and corresponding metric set, $\Lambda(\mathbf{h})$ are shown in Figure 3.4. As stated previously, tentative decisions can be made on the data symbols in the set, $\Theta(h)=\Psi(\mathbf{h})-\bigcup_{k>h}\Psi(k)$. For example, if the data symbol, $b_6(n-1)$, does not appear in any of the future data symbol sets, i.e. $b_6(n-1)\notin\bigcup_{k>h}\Psi(k)$, then $b_6(n-1)\in\Theta(h)$. Further, if $b_6(n-1)$ is the only symbol in $\Psi(\mathbf{h})$ that does not appear in future data symbol sets, then $\Theta(h)=\{b_6(n-1)\}$. The elements in $\Theta(h)$ are given by $\Theta_j(h)$ where $1\leq j\leq|\Theta(h)|$, and since $|\Theta(h)|=1$ in this example, j attains a maximum value of 1. Therefore, a tentative decision is currently made for $b_6(n-1)$ only. In order to make a tentative decision for $b_6(n-1)$, the $|\alpha|^{|\Psi(\mathbf{h})|-j+1}=2^{3-1+1}=8$ metrics are divided into $|\alpha|^{|\Psi(\mathbf{h})|-j}=2^{3-1}=4$ groups with each group containing $|\alpha|=2$ metrics that differ in the symbol $\Theta_j(h)=b_6(n-1)$.

In Figure 3.4, $\alpha^{|\Psi(\mathbf{h})|}$ lists all possible combinations of the data symbol values in $\Psi(\mathbf{h})$, and $\Lambda(\mathbf{h})$ lists the corresponding metrics. Fig. 3.5 repeats this information, but initially reverses the order of $\alpha^{|\Psi(\mathbf{h})|}$ and $\Lambda(\mathbf{h})$ for purposes of description. As can be seen from Fig. 3.5, the arrows show how the 8 metrics are divided into 4 groups, and each group differs only in the symbol, $b_6(n-1)$. Within each group, a decision is formed by selecting the minimum metric and discarding the larger of the 2. It can be seen from Fig. 3.5 that the number of metrics has been reduced by a factor of $|\alpha|^{|\Theta(h)|}=2^1=2$, and $\Psi(\mathbf{h})$ is replaced by $\Psi(\mathbf{h})-\Theta(h)$. Thus, $\Psi(\mathbf{h})$ becomes $\{b_4(n-1),b_6(n)\}$, and the tentative decisions for $b_6(n-1)$ are stored in $D(\mathbf{h})$.

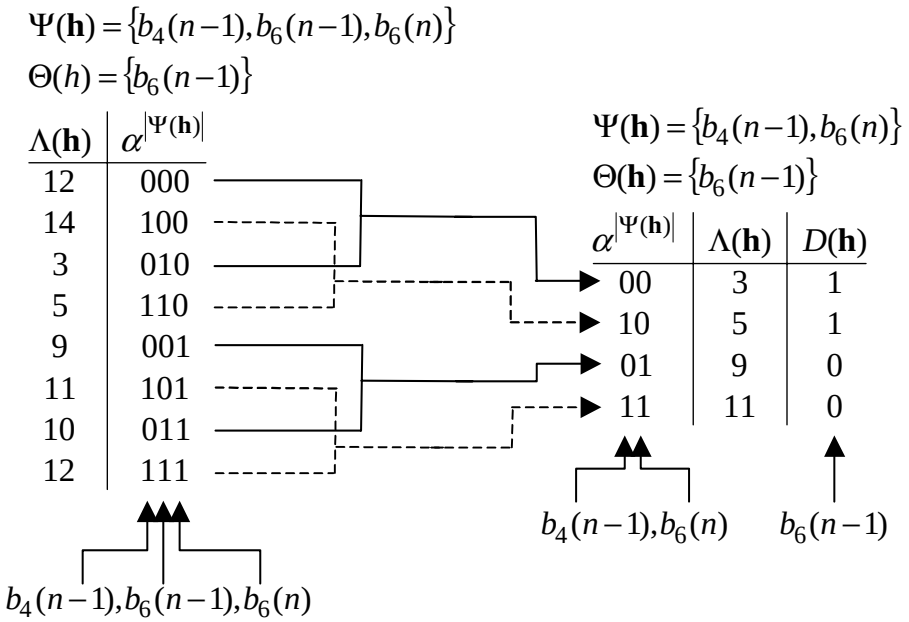

Figure 3.5: The Select routine applied to sample metrics, $\Lambda(\mathbf{h})$.

The Combine and Select routines form the major components of the CMM algorithm. Now that these routines have been described in detail, the following section will provide an additional example which further illustrates the CMM algorithm's operation.

3.3 A Typical System Using the CMM Algorithm

The major components of the CMM algorithm have now been addressed in terms of the Combine and Select routines. This example is used to demonstrate how these components fit together to form the overall algorithm. It is based on the connections for the $K = 2$ users and $L = 2$ antennas depicted in Fig. 3.1, along with the initializations provided in Table 3.1. Neither the Combine routine or the Select routine will be described in detail as examples of both of these were given in the Sections 3.1.2 and 3.2.2 respectively. Therefore, in Figs. 3.6 and 3.7, double arrows are used to represent the Combine routine, while single arrows represent the Select routine.

Fig. 3.6 shows the CMM algorithm during start-up, while Fig. 3.7 shows the CMM algorithm during normal operation. When Fig. 3.6 is compared with Fig. 3.7, it is observed

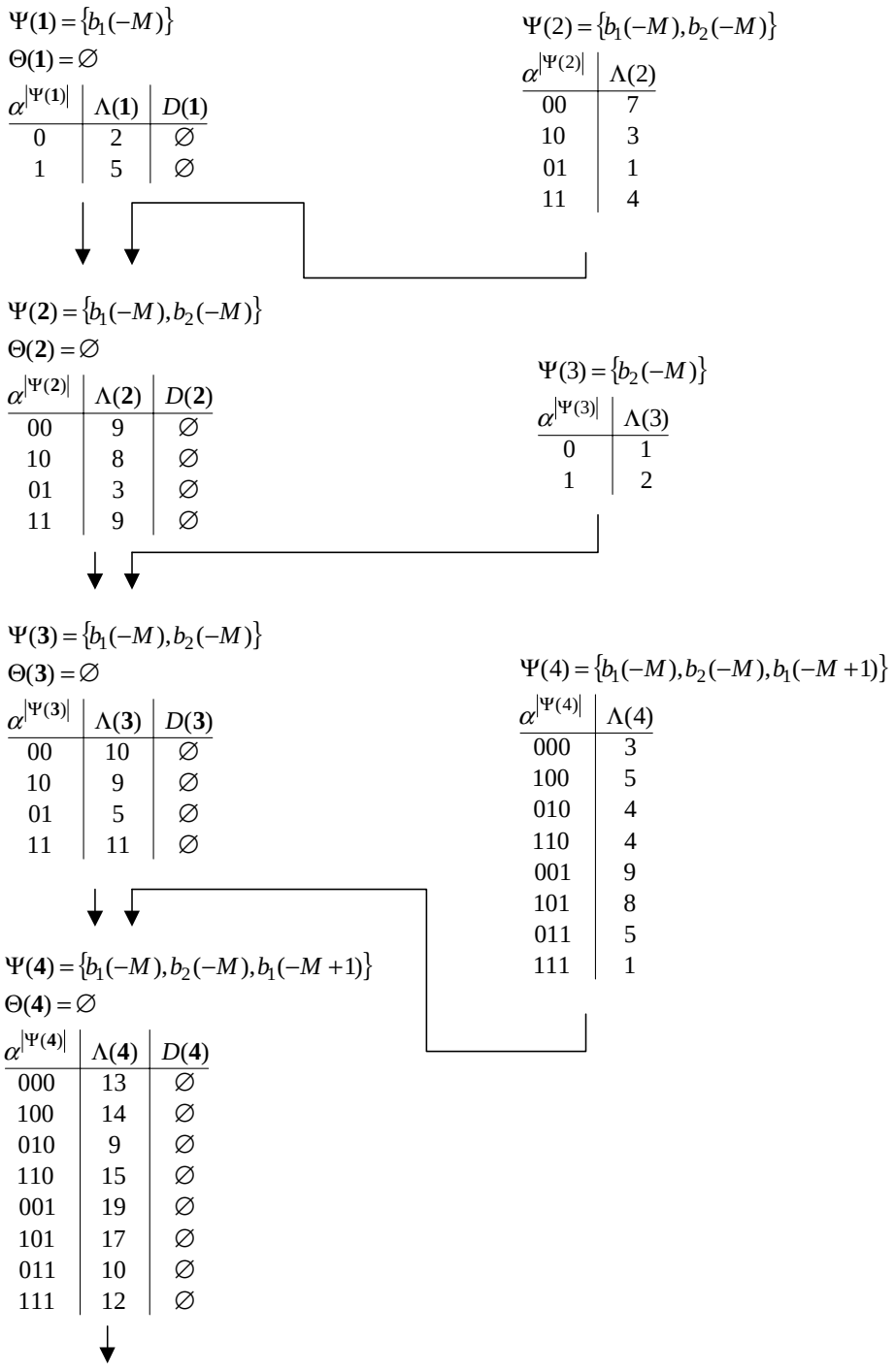

Figure 3.6: CMM algorithm during start-up.

that the Combine routine is used in both start-up and normal operation. However, the Select routine is only needed during normal operation. The reason that the Select routine is not required during start-up results from the fact that $b_k(n) = 0$ for $n < -M$. The relevant metrics, $\Lambda(h)$, are normally calculated using (2.30). However, for this example the actual metrics are replaced with integers for simplicity. The CMM algorithm in Fig. 3.6 is initialized by setting $\Psi(\mathbf{1}) = \Psi(1)$ and $\Lambda(\mathbf{1}) = \Lambda(1)$. Since no tentative decisions have been formed at this point, $\Theta(\mathbf{1}) = \varnothing$, and each entry of $D(\mathbf{1})$ is set to $\varnothing$. The Combine routine creates $\Psi(\mathbf{2}) = \Psi(\mathbf{1}) \cup \Psi(2)$ and merges $\Lambda(\mathbf{1})$ and $\Lambda(2)$ to form $\Lambda(\mathbf{2})$. During start-up, the Combine routine is repeatedly called until $\Psi(\mathbf{4})$ is formed. At stage 4, the CMM algorithm enters normal operation as time n changes to $n = -M + 1$.

Fig. 3.7 is a continuation of Fig. 3.6, and it begins by executing the Select routine. It is observed in Table 3.1 that by stage $h = 4$ the symbol, $b_1(-M)$ does not appear in any of the subsequent data symbol sets. Therefore, a tentative decision can be made on $b_1(-M)$ without impacting the final result. As expected, the number of metrics in $\Lambda(\mathbf{4})$ has been reduced by a factor of 2. Once the appropriate tentative decisions have been made, the Combine routine is again used to execute $\Lambda(\mathbf{5}) = \Lambda(\mathbf{4}) \textcircled{\sum} \Lambda(5)$. Since all of the symbols in $\Psi(\mathbf{5})$ are used in subsequent metrics, there is no reason to call Select at this point. Therefore, Combine is again called to create $\Lambda(\mathbf{6}) = \Lambda(\mathbf{5}) \textcircled{\sum} \Lambda(6)$. Since $b_2(-M)$ in $\Psi(\mathbf{6})$ is not used in any of the further metrics, tentative decisions can be made on $b_2(-M)$ without affecting the final result. This general procedure is repeated for $h > 6$.

3.4 Practical Considerations of the CMM Algorithm

In each stage of the CMM algorithm, $2^{K_{\psi_l}+1}$ probabilities are computed. Therefore, in total $N\left(\sum_{l=1}^{L} K_{\psi_l} 2^{K_{\psi_l}+1}\right)$ probabilities are computed to detect N symbols for each of the K different users.

So far in the CMM algorithm's description, $\Lambda(\mathbf{h})$ has been calculated in a consecutive fashion, starting with $h = 1$ and ending with $h = N\left(\sum_{l'=1}^{L} K_{\psi_{l'}}\right)$. However, in order to speed up the process, many of the $\Lambda(h)$'s could be calculated simultaneously since data is received at a number of different antennas. In a similar way to traditional ML multiuser detection, a processor at each antenna could calculate all of its metrics, $\lambda_{ilx}(n)$. The unique aspects of ML-MUMD enter through the use of the Combine and Select routines in the CMM algorithm. In fact, the Combine routine could be invoked many times in parallel at each of

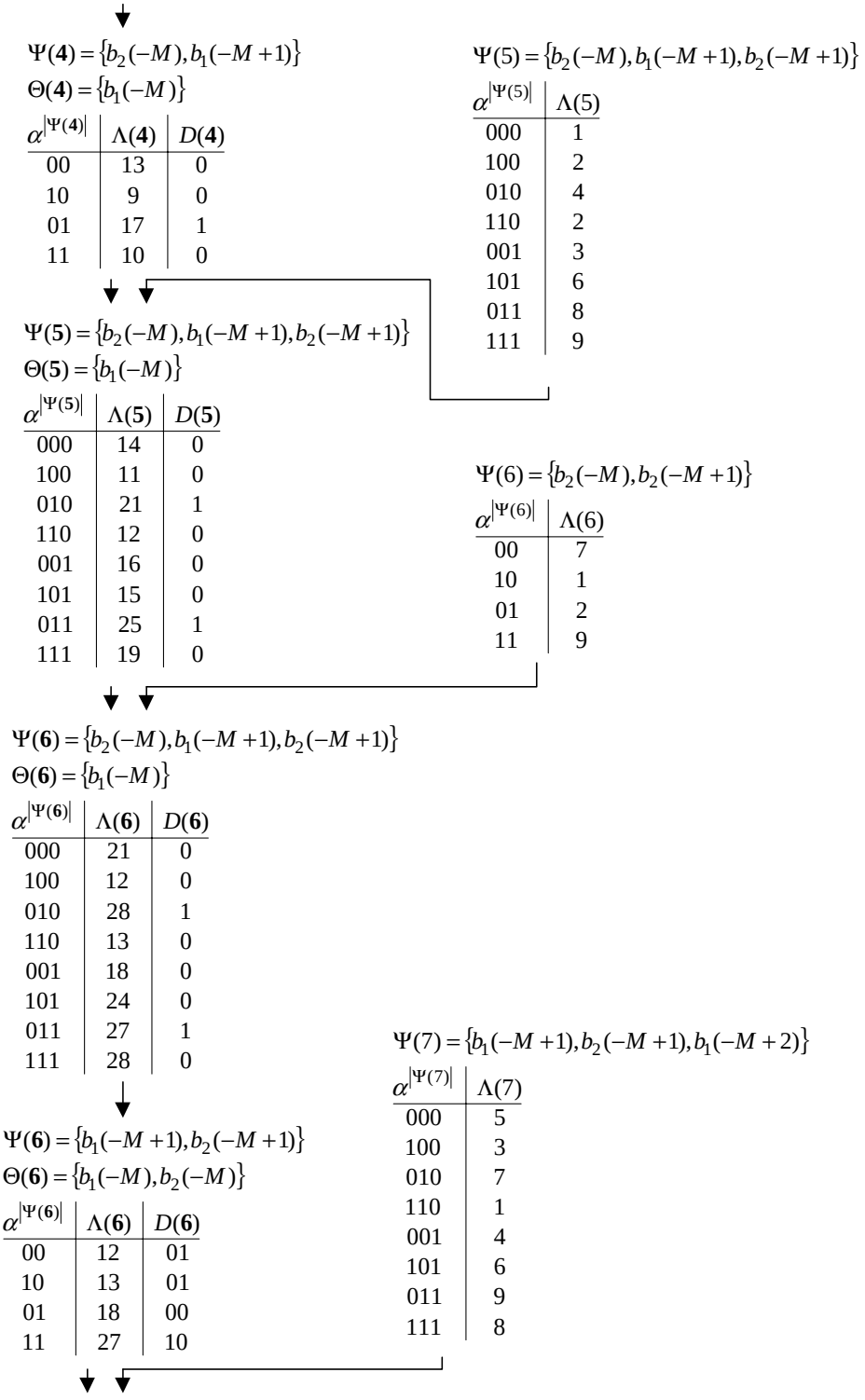

Figure 3.7: CMM algorithm during normal operation.

the macrodiversity antennas, but the Select routine should not be invoked until the interim metrics have been added to the current total at the system controller.

Regardless of how we order our calculations, the delay in detecting the information symbols is variable. However, similar to the Viterbi algorithm, a fixed delay can be achieved with a negligible loss in performance by postponing detection by a finite amount for all symbols [15].

This chapter has described the CMM algorithm for ML multiuser-macrodiversity detection in general terms, and it has also provided specific examples which illustrate the algorithm's operation. Chapter 5 analyzes the performance of this ML multiuser-macrodiversity detector. However, before the detector's performance can be evaluated, the issue of including imperfect channel estimates into the metrics must first be addressed.

Chapter 4

Multiuser Channel Estimation

As can be seen from (2.30), the ML multiuser-macrodiversity detector relies on channel estimates for detection. Previous studies have shown that these channel estimates must be extremely accurate to warrant optimal, ML, multiuser detection [46].

Section 1.6 outlines prior work in the area of code synchronization and channel estimation. Subspace based approaches to parameter estimation are used to estimate delay and amplitude information, but they are unable to estimate the channel's complex gain as the second order statistics contain no phase information [52]. Most of the ML parameter estimation techniques to date estimate both the delay and the channel's complex gain during a training sequence that is set during initial acquisition [54], [55], [56], and [57]. However, these techniques do not address the issue of tracking the complex gain in a fading environment. The insertion of pilot symbols into the data stream has proven to be an effective method of obtaining and tracking channel estimates in a single user system [58]. In [59], the authors propose a pilot-based, MMSE, multiuser channel estimation technique for a TDMA system.

This chapter extends the method in [59] for use in a CDMA system. However, unlike the study in [59], we do not need to concern ourselves with training sequence design as the pseudorandom sequences used in a DS-CDMA system are already designed with good autocorrelation and cross-correlation properties. The proposed multiuser channel estimation technique relies on prior code synchronization. However, since code synchronization is not flawless, imperfect timing estimates have been included into the analysis. The effects of frequency selective fading have also been included into the multiuser channel estimator. The results show that the combination of pilot symbols with MMSE multiuser channel

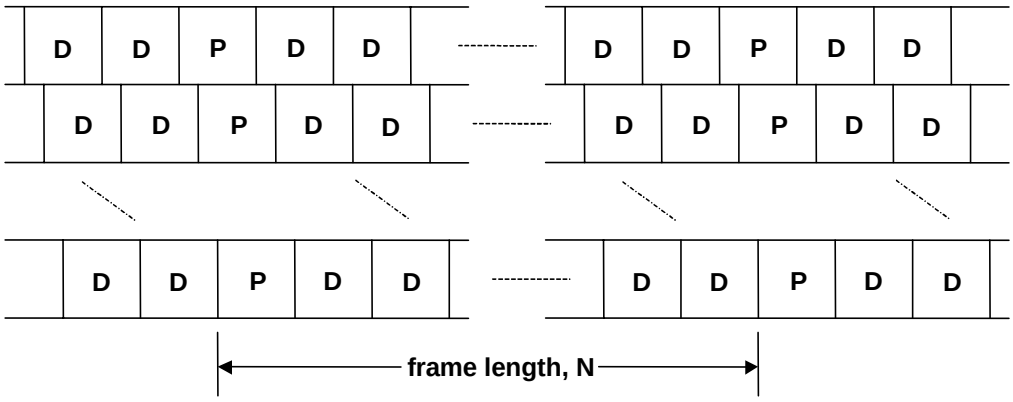

Figure 4.1: One pilot symbol without guard bands.

estimation in a CDMA system provides accurate channel estimates which can be used in (2.30).

4.1 Pilot Symbol Insertion Techniques

In order to perform the MMSE channel estimation, pilot symbols are periodically and simultaneously inserted into all of the users' data streams. The observation vector for MMSE multiuser channel estimation is given by

$$\boldsymbol{\theta}_l = \left[\mathbf{y}_{\psi_l}^{\mathrm{T}}(-QN), ..., \mathbf{y}_{\psi_l}^{\mathrm{T}}(QN)\right]^{\mathrm{T}} \tag{4.1}$$

where N denotes the spacing between pilot symbols; in other words, N is the length of the frame. Frame lengths for the various pilot symbol insertion techniques are shown in Figs. 4.1, 4.2, and 4.3. For clarity, the subsequent arrivals due to frequency selective fading have been omitted from the diagrams in Figs. 4.1, 4.2, and 4.3. Since $2Q+1$ observations are used to form a channel estimate in (4.1), $2Q+1$ is referred to as the interpolator order.

From (2.11) and (2.12), it can be observed that the matched filter outputs, $\mathbf{y}_{\psi_l}(n)$, are

$$\begin{aligned}\mathbf{y}_{\psi_l}(n) &= \sum_{i=-1}^{1} [\mathbf{R}_{\mathbf{s},\psi_l}(n, n+i)\,\mathbf{B}_{\psi_l}(n+i)\,\mathbf{c}_{\psi_l}(n+i) + \\ &\quad \mathbf{R}_{\mathbf{s},\psi_l,\phi_l}(n, n+i)\,\mathbf{B}_{\phi_l}(n+i)\,\mathbf{c}_{\phi_l}(n+i)] + \mathbf{z}_{\psi_l}(n).\end{aligned} \tag{4.2}$$

The multiuser channel estimator uses the observation vector, $\boldsymbol{\theta}_l$, to estimate the channels' complex gains in $\mathbf{c}_{\psi_l}(n)$. Since $\boldsymbol{\theta}_l$ and $\mathbf{c}_{\psi_l}(n)$ are jointly Gaussian, the MMSE estimator is

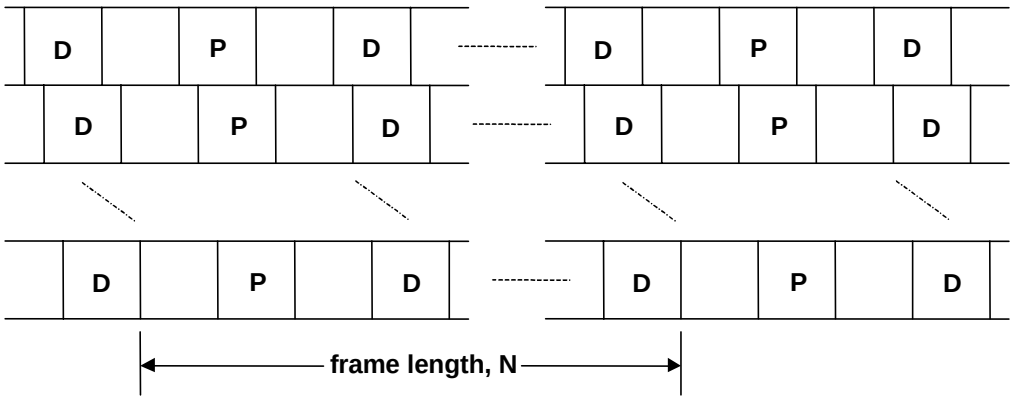

Figure 4.2: One pilot symbol with guard bands.

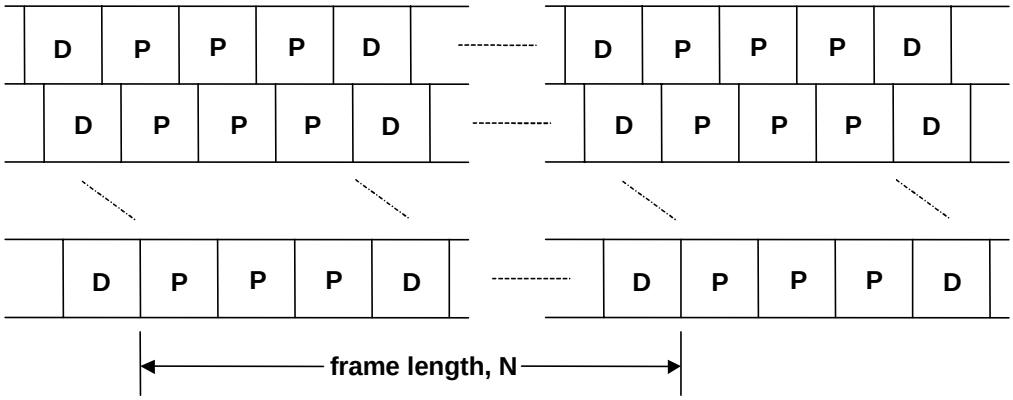

Figure 4.3: Three pilot symbols.

linear, and the channel estimates are given by

$$\mathbf{v}_{\psi_l}(n) = \mathbf{U}_l(n)\,\boldsymbol{\theta}_l. \tag{4.3}$$

For MMSE estimation, $\partial J(n)/\partial \mathbf{U}_l(n) = 0$, where $J(n)$ is defined as

$$J(n) = E\left[\left(\mathbf{c}_{\psi_l}(n) - \mathbf{U}_l(n)\,\boldsymbol{\theta}_l\right)^{\dagger}\left(\mathbf{c}_{\psi_l}(n) - \mathbf{U}_l(n)\,\boldsymbol{\theta}_l\right)\right]. \tag{4.4}$$

It follows that the optimal MMSE channel estimates are given by [66]

$$\mathbf{v}_{\psi_l}^{opt}(n) = \mathbf{P}_l^{\dagger}(n)\,\mathbf{R}_{\boldsymbol{\theta}_l}^{-1}\boldsymbol{\theta}_l \tag{4.5}$$

where $\mathbf{R}_{\boldsymbol{\theta}_l} = \frac{1}{2}E\left[\boldsymbol{\theta}_l\boldsymbol{\theta}_l^{\dagger}\right]$ and $\mathbf{P}_l(n) = \frac{1}{2}E\left[\boldsymbol{\theta}_l\mathbf{c}_{\psi_l}^{\dagger}(n)\right]$. The q^{th} submatrix of $\mathbf{P}_l(n)$ is given by $[\mathbf{P}_l(n)]_{[q]} = \frac{1}{2}E\left[\mathbf{y}_{\psi_l}(qN)\,\mathbf{c}_{\psi_l}^{\dagger}(n)\right]$. By using (4.2) and the assumption that the users' channels fade independently from each other and from the thermal noise, $[\mathbf{P}_l(n)]_{[q]}$ can be calculated as shown below

$$[\mathbf{P}_l(n)]_{[q]} = \sum_{i=-1}^{1}\mathbf{R}_{\mathbf{s},\psi_l}(qN, qN+i)\,\mathbf{B}_{\psi_l}(qN+i)\,\boldsymbol{\xi}_{\mathbf{c},\psi_l}(qN+i-n) \tag{4.6}$$

where $\boldsymbol{\xi}_{\mathbf{c},\psi_l}(m)$ is a correlation matrix similar in format to (2.21), and $q \in \{-Q, ..., Q\}$. The q,p^{th} submatrix of $\mathbf{R}_{\boldsymbol{\theta}_l}$ is given by $[\mathbf{R}_{\boldsymbol{\theta}_l}]_{[q,p]} = \frac{1}{2}E\left[\mathbf{y}_{\psi_l}(qN)\,\mathbf{y}_{\psi_l}^{\dagger}(pN)\right]$. Again, by assuming that the users' channels fade independently, $[\mathbf{R}_{\boldsymbol{\theta}_l}]_{[q,p]}$ can be written as

$$\begin{aligned}[\mathbf{R}_{\boldsymbol{\theta}_l}]_{[q,p]} = \sum_{i=-1}^{1}\sum_{j=-1}^{1}\Big[&\mathbf{R}_{\mathbf{s},\psi_l}(qN, qN+i)\,\mathbf{B}_{\psi_l}(qN+i)\,\boldsymbol{\xi}_{\mathbf{c},\psi_l}((q-p)N+i-j)\\ &\mathbf{B}_{\psi_l}^{\dagger}(pN+j)\,\mathbf{R}_{\mathbf{s},\psi_l}^{\dagger}(pN, pN+j) + \mathbf{R}_{\mathbf{s},\psi_l,\phi_l}(qN, qN+i)\,\mathbf{B}_{\phi_l}(qN+i)\\ &\boldsymbol{\xi}_{\mathbf{c},\phi_l}((q-p)N+i-j)\,\mathbf{B}_{\phi_l}^{\dagger}(pN+j)\,\mathbf{R}_{\mathbf{s},\psi_l,\phi_l}^{\dagger}(pN, pN+j)\Big] +\\ &N_o\widehat{\mathbf{R}}_{\mathbf{s},\psi_l}(qN, pN)\end{aligned} \tag{4.7}$$

where

$$\widehat{\mathbf{R}}_{\mathbf{s},\psi_l}(qN, pN) = \begin{cases}\widehat{\mathbf{R}}_{\mathbf{s},\psi_l}(qN, qN), & q = p\\ 0 & q \neq p\end{cases} \tag{4.8}$$

and $q, p \in \{-Q, ..., Q\}$.

The difficulty that arises in the construction of $\mathbf{P}_l(n)$ and $\mathbf{R}_{\boldsymbol{\theta}_l}$ is similar to that encountered with the covariance matrix, $\mathbf{K}_{\mathbf{y},\psi_l}$, in Chapter 2. $\mathbf{P}_l(n)$ and $\mathbf{R}_{\boldsymbol{\theta}_l}$ depend on quantities

such as $\mathbf{R}_{\mathbf{s},\psi_l}$ and $\mathbf{R}_{\mathbf{s},\psi_l,\phi_l}$, and we do not have full knowledge of this information at the receiver. Therefore, we are required to make suboptimal channel estimates which are given by (4.3), where $\mathbf{U}_l(n) = \widehat{\mathbf{P}}_l^{\dagger}(n)\,\widehat{\mathbf{R}}_{\boldsymbol{\theta}_l}^{-1}$, and $\widehat{\mathbf{P}}_l(n)$ and $\widehat{\mathbf{R}}_{\boldsymbol{\theta}_l}$ are estimates of $\mathbf{P}_l(n)$ and $\mathbf{R}_{\boldsymbol{\theta}_l}$ respectively. The estimates, $\widehat{\mathbf{P}}_l(n)$ and $\widehat{\mathbf{R}}_{\boldsymbol{\theta}_l}$, depend on the amount of information known at the receiver and on the method used for pilot symbol insertion. In the following sections, $\widehat{\mathbf{P}}_l(n)$ and $\widehat{\mathbf{R}}_{\boldsymbol{\theta}_l}$ are derived for three different situations: 1) One pilot symbol inserted per frame, 2) One pilot symbol inserted per frame with guard bands placed on either side of the pilot symbol, and 3) Three pilot symbols inserted per frame. These three pilot symbol insertion techniques are similar to those in [42], where the author investigates an SIC receiver, which uses a decorrelator for multiuser channel estimation.

4.1.1 One Pilot Symbol without Guard Bands

Fig. 4.1 depicts the insertion of one pilot symbol per frame. As can be seen from Fig. 4.1, no guard bands are placed on either side of the pilot symbols. Therefore, the adjacent data symbols produce interference in the multiuser channel estimation. Since data symbols reside next to the pilot symbols, we have no knowledge $\mathbf{B}_{\psi_l}(qN+i)$ or $\mathbf{B}_{\psi_l}(pN+j)$ in (4.6) and (4.7) for $i,j = \pm 1$. Therefore, the estimates, $\widehat{\mathbf{P}}_l(n)$ and $\widehat{\mathbf{R}}_{\boldsymbol{\theta}_l}$, in (4.9) and (4.10) cannot include these adjacent data symbols. Hence, when one pilot symbol is inserted per frame with no guard bands, the q^{th} submatrix of $\widehat{\mathbf{P}}_l(n)$ becomes

$$\left[\widehat{\mathbf{P}}_l(n)\right]_{[q]} = \widehat{\mathbf{R}}_{\mathbf{s},\psi_l}(qN,qN)\,\mathbf{B}_{\psi_l}(qN)\,\boldsymbol{\xi}_{\mathbf{c},\psi_l}(qN-n) \tag{4.9}$$

where $q \in \{-Q,...,Q\}$. Similarly, the q,p^{th} submatrix of $\widehat{\mathbf{R}}_{\boldsymbol{\theta}_l}$ is

$$\begin{aligned}\left[\widehat{\mathbf{R}}_{\boldsymbol{\theta}_l}\right]_{[q,p]} &= \widehat{\mathbf{R}}_{\mathbf{s},\psi_l}(qN,qN)\,\mathbf{B}_{\psi_l}(qN)\,\boldsymbol{\xi}_{\mathbf{c},\psi_l}((q-p)N) \\ &\quad \mathbf{B}_{\psi_l}^{\dagger}(pN)\,\widehat{\mathbf{R}}_{\mathbf{s},\psi_l}^{\dagger}(pN,pN) + (I_{o_l}+N_o)\,\widehat{\mathbf{R}}_{\mathbf{s},\psi_l}(qN,pN)\end{aligned} \tag{4.10}$$

where $q,p \in \{-Q,...,Q\}$. In (4.10), the unknown information is modeled as white noise, where I_{o_l} is given in (2.23). The I_{o_l} in (2.23) underestimates the interference as it does not account for the interference resulting from the adjacent data symbols. The interference from the adjacent data symbols is difficult to estimate as it depends on the degree of asynchronicity between users. Therefore, I_{o_l} was both overestimated and underestimated to determine its effect on the channel estimation errors. It was observed that overestimating the I_{o_l} results in an unwanted error floor, while underestimating I_{o_l} results in no noticeable degradation in the channel estimation errors.

4.1.2 One Pilot Symbol with Guard Bands

Fig. 4.2 shows the insertion of one pilot symbol per frame with guard intervals placed on either side of the pilot symbol. During the guard intervals, the mobile suppresses transmission for time instants $n = qN \pm 1$. Therefore, the adjacent data symbols no longer produce interference in the multiuser channel estimation. Since the adjacent data symbols are not transmitted, the $\mathbf{P}_l(n)$ and $\mathbf{R}_{\boldsymbol{\theta}_l}$ in (4.6) and (4.7) can be rewritten as:

$$[\mathbf{P}_l(n)]_{[q]} = \mathbf{R}_{\mathbf{s},\psi_l}(qN, qN)\,\mathbf{B}_{\psi_l}(qN)\,\boldsymbol{\xi}_{\mathbf{c},\psi_l}(qN - n) \tag{4.11}$$

and

$$\begin{aligned}[\mathbf{R}_{\boldsymbol{\theta}_l}]_{[q,p]} &= \mathbf{R}_{\mathbf{s},\psi_l}(qN, qN)\,\mathbf{B}_{\psi_l}(qN)\,\boldsymbol{\xi}_{\mathbf{c},\psi_l}((q-p)N) \\ &\quad \mathbf{B}^{\dagger}_{\psi_l}(pN)\,\mathbf{R}^{\dagger}_{\mathbf{s},\psi_l}(pN, pN) + \mathbf{R}_{\mathbf{s},\psi_l,\phi_l}(qN, qN)\,\mathbf{B}_{\phi_l}(qN) \\ &\quad \boldsymbol{\xi}_{\mathbf{c},\phi_l}((q-p)N)\,\mathbf{B}^{\dagger}_{\phi_l}(pN)\,\mathbf{R}^{\dagger}_{\mathbf{s},\psi_l,\phi_l}(pN, pN) + \\ &\quad N_o\widehat{\mathbf{R}}_{\mathbf{s},\psi_l}(qN, pN)\,. \end{aligned} \tag{4.12}$$

In Section 4.1.1, the estimates, $\widehat{\mathbf{P}}_l(n)$ and $\widehat{\mathbf{R}}_{\boldsymbol{\theta}_l}$, were derived with the assumption that the receiver had no knowledge of the adjacent data symbols. Since the adjacent data symbols are no longer transmitted in this section, this underlying assumption at the receiver remains unchanged. Therefore, $\widehat{\mathbf{P}}_l(n)$ and $\widehat{\mathbf{R}}_{\boldsymbol{\theta}_l}$ are given by (4.9) and (4.10) respectively.

4.1.3 Three Pilot Symbols

Fig. 4.3 depicts the insertion of three adjacent pilot symbols per frame. Since guard bands are no longer used to suppress transmission, $\mathbf{P}_l(n)$ and $\mathbf{R}_{\boldsymbol{\theta}_l}$ are given by (4.6) and (4.7) respectively. The receiver has full knowledge of all of the data symbols in (4.6) and (4.7), and the estimates, $\widehat{\mathbf{P}}_l(n)$ and $\widehat{\mathbf{R}}_{\boldsymbol{\theta}_l}$, become:

$$\left[\widehat{\mathbf{P}}_l(n)\right]_{[q]} = \sum_{i=-1}^{1} \widehat{\mathbf{R}}_{\mathbf{s},\psi_l}(qN, qN+i)\,\mathbf{B}_{\psi_l}(qN+i)\,\boldsymbol{\xi}_{\mathbf{c},\psi_l}(qN+i-n) \tag{4.13}$$

and

$$\begin{aligned}\left[\widehat{\mathbf{R}}_{\boldsymbol{\theta}_l}\right]_{[q,p]} &= \sum_{i=-1}^{1}\sum_{j=-1}^{1}\Big[\widehat{\mathbf{R}}_{\mathbf{s},\psi_l}(qN, qN+i)\,\mathbf{B}_{\psi_l}(qN+i)\,\boldsymbol{\xi}_{\mathbf{c},\psi_l}((q-p)N+i-j) \\ &\quad \mathbf{B}^{\dagger}_{\psi_l}(pN+j)\,\widehat{\mathbf{R}}^{\dagger}_{\mathbf{s},\psi_l}(pN, pN+j)\Big] + (I_{o_l} + N_o)\,\widehat{\mathbf{R}}_{\mathbf{s},\psi_l}(qN, pN)\,. \end{aligned} \tag{4.14}$$

Now that the various pilot symbol insertion techniques have been presented, the following section will investigate the performance of the MMSE multiuser channel estimators.

4.2 Performance Calculations

By using the suboptimal estimate, $\mathbf{v}_{\psi_l}(n) = \mathbf{U}_l(n)\boldsymbol{\theta}_l$, where $\mathbf{U}_l(n) = \widehat{\mathbf{P}}_l^{\dagger}(n)\widehat{\mathbf{R}}_{\boldsymbol{\theta}_l}^{-1}$, the estimation error covariance matrix becomes [59], [66]

$$\begin{aligned}\mathbf{R}_{\mathbf{e},\psi_l}(n) &= E\left[\left(\mathbf{c}_{\psi_l}(n) - \mathbf{U}_l(n)\boldsymbol{\theta}_l\right)\left(\mathbf{c}_{\psi_l}(n) - \mathbf{U}_l(n)\boldsymbol{\theta}_l\right)^{\dagger}\right] \\ &= \boldsymbol{\xi}_{\mathbf{c},\psi_l}(0) - \mathbf{U}_l(n)\mathbf{P}_l(n) - \\ &\quad \mathbf{P}_l^{\dagger}(n)\mathbf{U}_l^{\dagger}(n) + \mathbf{U}_l(n)\mathbf{R}_{\boldsymbol{\theta}_l}\mathbf{U}_l^{\dagger}(n). \end{aligned} \tag{4.15}$$

The individual error variances, $\sigma_{e,lxg}^2$, are given by the diagonal elements of the matrix, $\mathbf{R}_{\mathbf{e},\psi_l}(n)$. In particular, the diagonal of $\mathbf{R}_{\mathbf{e},\psi_l}(n)$ is

$$vdiag\left(\mathbf{R}_{\mathbf{e},\psi_l}(n)\right) = \left[\left\{\left[\sigma_{e,lx0}^2, ..., \sigma_{e,lxG}^2\right] \middle| x \in \psi_l\right\}\right]^{\mathrm{T}} \tag{4.16}$$

where the function *vdiag* is used to convert the diagonal of a matrix into a vector. Similarly, the individual variances of the channel estimates, $\sigma_{v,lxg}^2$, are given by

$$vdiag\left(\mathbf{U}_l(n)\mathbf{R}_{\boldsymbol{\theta}_l}\mathbf{U}_l^{\dagger}(n)\right) = \left[\left\{\left[\sigma_{v,lx0}^2, ..., \sigma_{v,lxG}^2\right] \middle| x \in \psi_l\right\}\right]^{\mathrm{T}} \tag{4.17}$$

and the correlation coefficients are found in (4.18), where η_{lxg} denotes the correlation coefficient between the complex channel gain, $c_{lxg}(n)$ and the channel estimate, $v_{lxg}(n)$.

$$\begin{aligned} &vdiag\left(\mathbf{P}_l^{\dagger}(n)\mathbf{U}_l^{\dagger}(n)\right) = \\ &\left[\left\{\left[\eta_{lx0}\sigma_{c,lx0}\sigma_{v,lx0}, ..., \eta_{lxG}\sigma_{c,lxG}\sigma_{v,lxG}\right] \middle| x \in \psi_l\right\}\right]^{\mathrm{T}}. \end{aligned} \tag{4.18}$$

In (4.15), the estimation error covariance matrix depends on n. However, it is shown in [58] that while the estimation error depends on the position within the frame, this position dependence is negligible. Therefore, we only need to calculate the individual error variances for one position in the frame, and the resulting $\left\{\sigma_{e,lxg}^2\right\}$ are valid for all positions. In a similar way the variances, $\left\{\sigma_{v,lxg}^2\right\}$ in (4.17) and the correlation coefficients, $\{\eta_{lxg}\}$ in (4.18) are also valid for all positions within the frame.

4.3 Results

This section investigates the performance of the MMSE multiuser channel estimators with the various pilot symbol insertion techniques. Before the results can be presented, we must

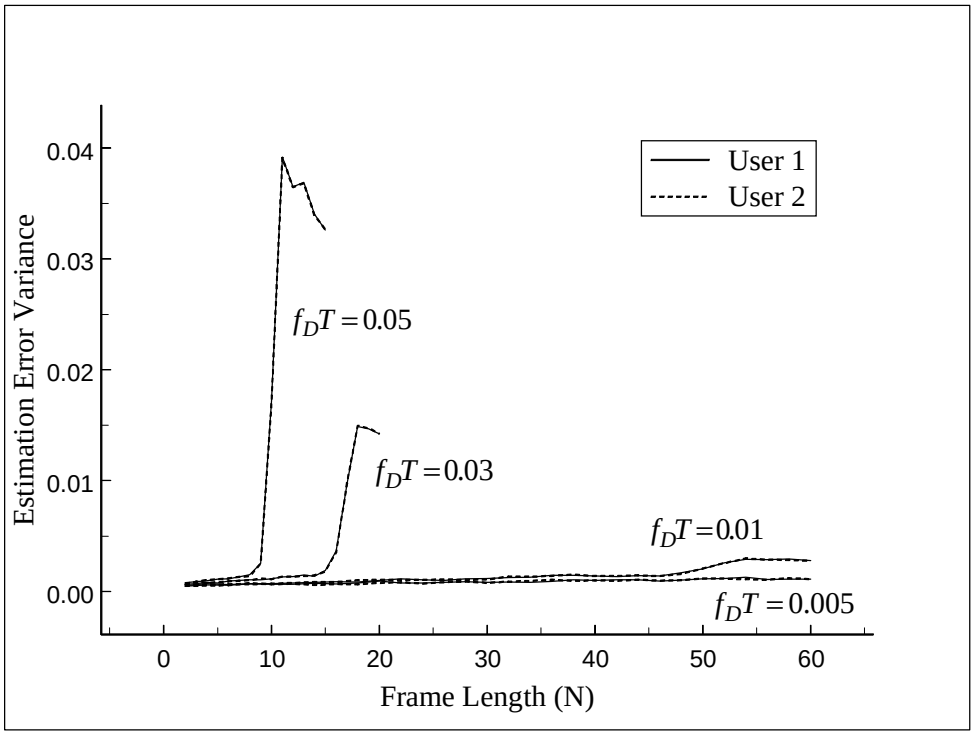

Figure 4.4: The effect of frame length on the estimation error variance.

first decide on an appropriate frame length, N, and an appropriate interpolator order, $2Q+1$. In order to determine adequate frame length and interpolator order sizes, the estimation error variance is plotted against both N and $2Q+1$ in Figs. 4.4 and 4.5, respectively. These figures are consistent with both [58] and [59]. Both [58] and [59] found that the pilot symbols need to be inserted above the Nyquist rate of the fading process, $2f_DT$. In other words, for adequate performance, $N < 1/(2f_DT)$. The authors of [58] and [59] also found that increasing the interpolator order beyond about 9 coefficients has very little impact on the estimation error variance. Therefore, the results presented in this section use an interpolator order of $2Q+1 = 9$ coefficients and a frame length size of $N = 20$ for a fading rate of $f_DT = 0.01$.

As mentioned previously, the multiuser channel estimators developed in Section 4.1

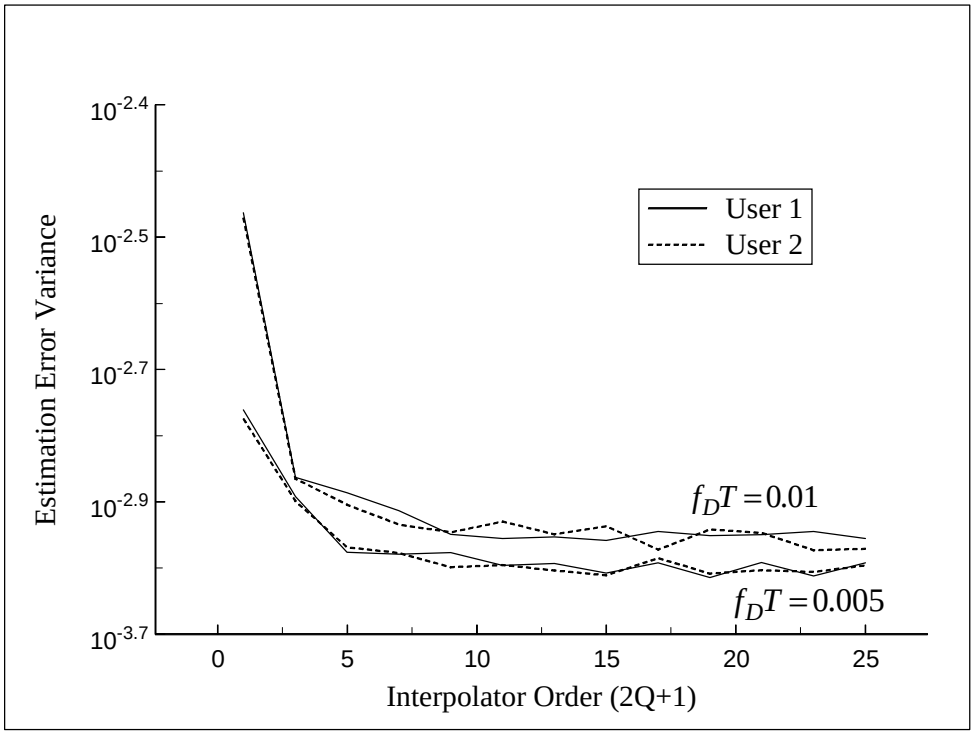

Figure 4.5: The effect of interpolator order size on the estimation error variance.

estimate the channel impulse response for channels with delay spread. Since it is common to assume an exponential power delay profile (PDP) in urban settings [3], the following results are produced for an exponentially decreasing PDP. The number of resolvable channel paths is given by $G+1$ where $G = \lfloor T_d/T_c \rfloor$, and the data symbol rate is $1/T$ where $T = (W/R)\,T_c$. In the following results it is assumed that $W = 1/T_c = 1.2288$ MHz, and the processing gain, $W/R = 32$.

The performance of the multiuser channel estimators depends on the code synchronization accuracy. A number of methods for code synchronization were discussed in Section 1.6. The technique presented in [55] describes a ML synchronization technique for DS-CDMA signals that proves to be robust in a near-far environment. In order to determine the performance of the MMSE multiuser channel estimators with imperfect synchronization, the timing estimation errors, $\{(\tau_{lk} - \widehat{\tau}_{lk})\}$, are generated using a truncated Gaussian distribution such that $|\tau_{lk} - \widehat{\tau}_{lk}| \leq T_c/2$ for all l and k. The standard deviation of the truncated Gaussian distribution depends on the effective bit energy to interference and noise density ratio, Γ_{lk} in (4.19), and is taken from the results of [55].

$$\Gamma_{lk} = \frac{A_k^2 \sum_{g=0}^{G} \sigma_{c,lkg}^2}{I_{o_l} + N_o}. \tag{4.19}$$

In the following results, the estimation error variance for the k^{th} user is given by $\sigma_{e,lk}^2 = \sum_{g=0}^{G} \sigma_{e,lkg}^2$. Both Γ_{lk} and $\sigma_{e,lk}^2$ depend on the antenna, l. However, since multiuser channel estimation is performed at each antenna separately, the dependence on l is immaterial for the results presented in this section. This dependence is preserved in the equations for consistency with the work on multiuser-macrodiversity detection.

In order to create Figs. 4.6 - 4.9, the pseudonoise (PN) sequences are randomly generated, and the results represent an average over 100 different PN sequences, each with a unique set of timing estimation errors. The results in the following figures are plotted against each user's signal to noise ratio, where the k^{th} user's SNR is given by

$$\Upsilon_{lk} = \frac{A_k^2 \sum_{g=0}^{G} \sigma_{c,lkg}^2}{N_o}. \tag{4.20}$$

Fig. 4.6 compares the performance of the three pilot symbol insertion techniques described in Section 4.1. The estimation error variances are plotted against the SNR for 2 asynchronous equipower users. Each of the users has a delay spread of $T_d = 2$ μsec; therefore, there are a total of $G + 1 = 3$ resolvable paths for each user. As can be seen from Fig.

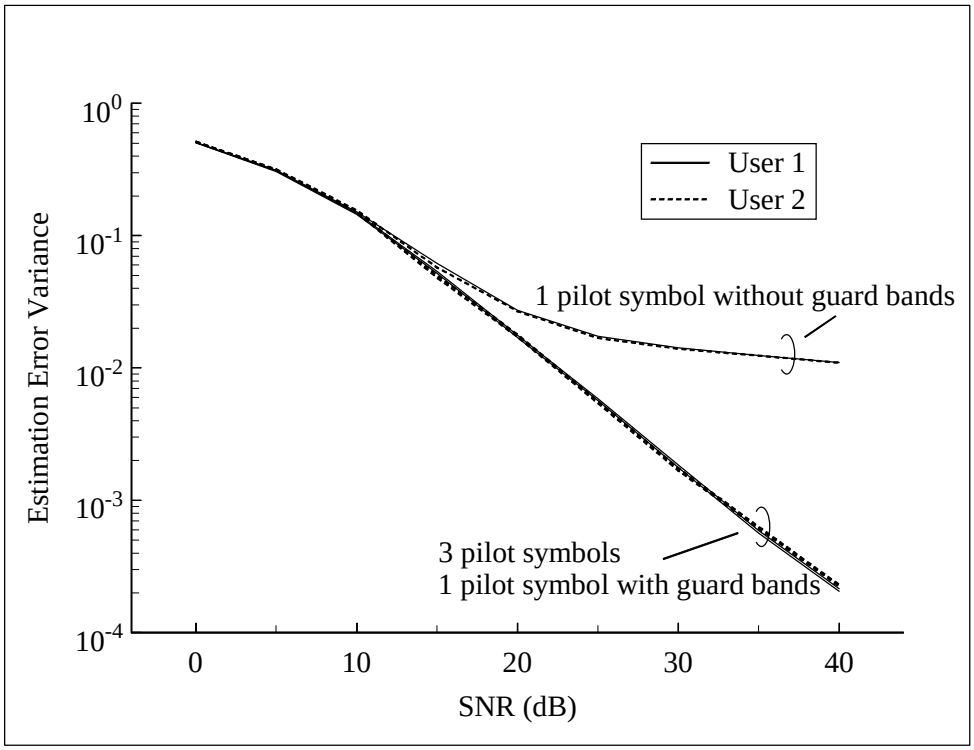

Figure 4.6: A comparison of the 3 different pilot symbol insertion techniques for 2 asynchronous users with delay spread.

4.6, the 3 pilot symbols and 1 pilot symbol with guard bands perform equally well, while the 1 pilot symbol without guard bands experiences an error floor. Since the 3 pilot symbol and 1 pilot symbol with guard bands cases perform equally well, the preferred method of pilot symbol insertion for 2 asynchronous users with delay spread is the insertion of 1 pilot symbol with guard bands on either side. The 1 pilot symbol with guard bands case is chosen over 3 pilot symbols as it is less wasteful in terms of transmitted energy.

From Fig. 4.6, it is obvious that guard intervals are essential for asynchronous users with delay spread. However, it is also obvious that guard intervals would not be needed if the users were synchronous, i.e. if their arrival times were identical, and if the delay spread were negligible. Figs. 4.7 and 4.8 investigate the effects of arrival times and delay spread on the insertion of 1 pilot symbol with and without guard intervals.

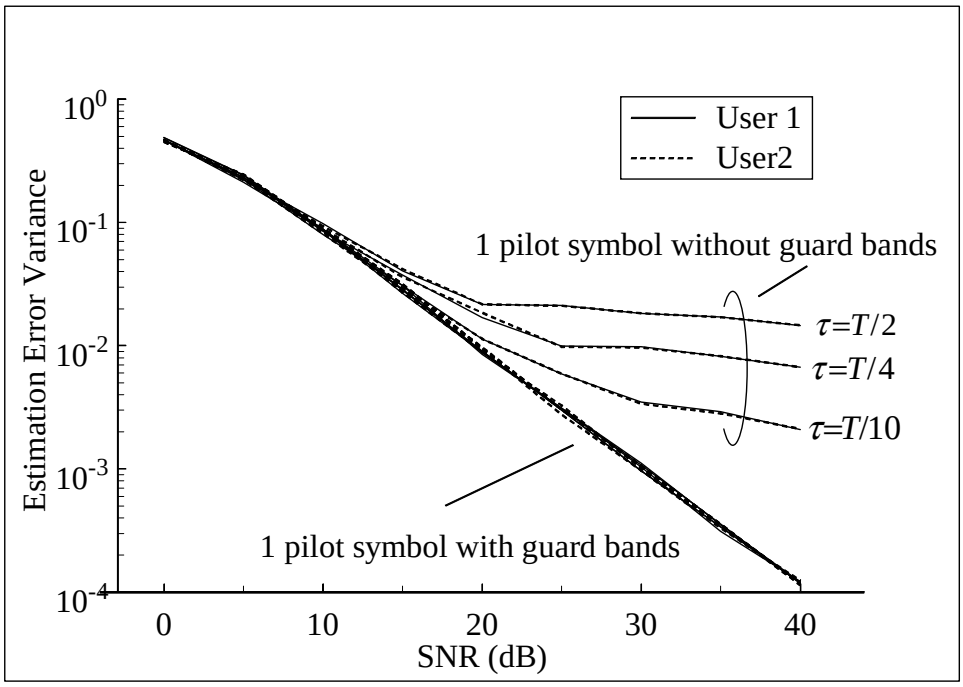

Figure 4.7: A comparison of the 1 pilot symbol with and without guard bands insertion techniques for different arrival times between users.

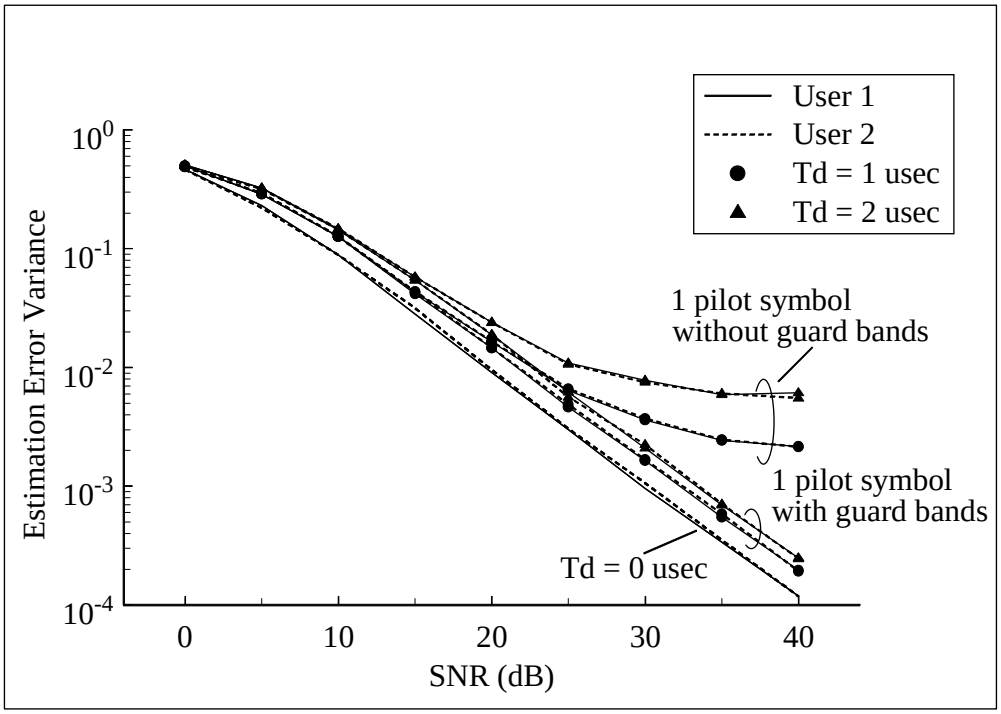

Figure 4.8: A comparison of the 1 pilot symbol with and without guard bands insertion techniques for different delay spreads.

In Fig. 4.7, the delay spread is set to $T_d = 0$, and the difference in arrival times between the 2 users is set to $\tau = 0$, $T/10$, $T/4$, and $T/2$. The two pilot symbol insertion techniques perform equally well when $\tau = 0$. However, as can be seen in Fig. 4.7, the insertion of 1 pilot symbol without guard bands develops an error floor for $\tau > 0$. When 1 pilot symbol is inserted with guard bands, the estimation error results remain consistent for all of the different arrival times.

In Fig. 4.8, the difference in arrival times between the 2 users is set to $\tau = 0$, and the delay spread is set to $T_d = 0$, 1 μsec, and 2 μsec. It can be seen from Fig. 4.8 that the 2 pilot symbol insertion techniques again perform equally well when $T_d = 0$. However, the insertion of 1 pilot symbol with guard intervals outperforms the case with no guard intervals when $T_d > 0$.

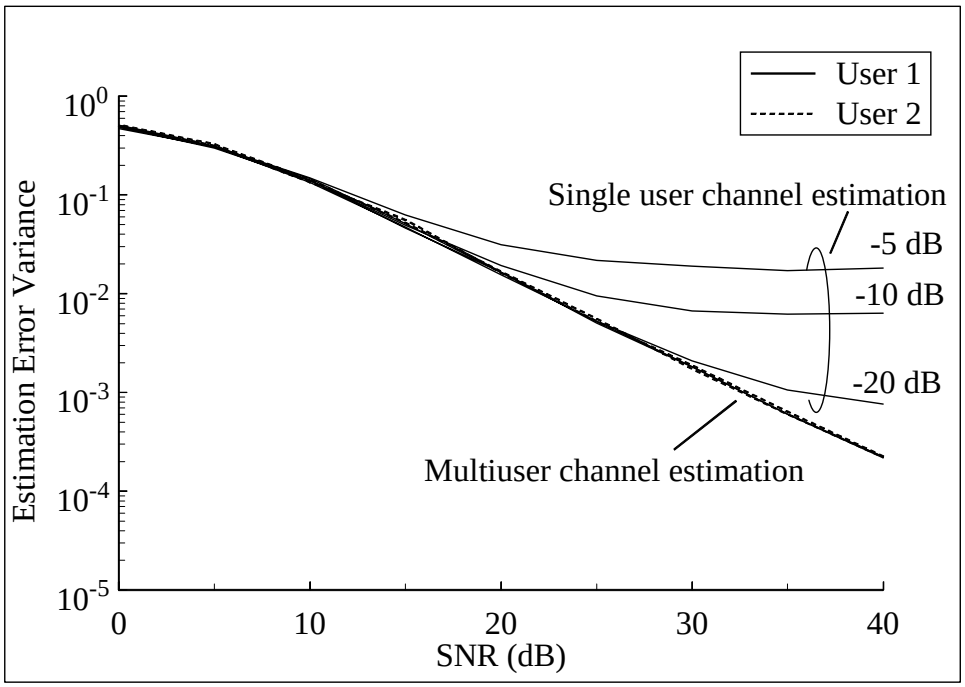

Figure 4.9: A comparison of multiuser channel estimation with single user channel estimation.

Fig. 4.9 determines the effect of leaving a user out of the MMSE multiuser channel estimation. Since the multiuser channel estimation in Fig. 4.9 is performed for only 2 users, removing one user from the channel estimation results in single user channel estimation. Both the multiuser and single user channel estimators in Fig. 4.9 are implemented by inserting 1 pilot symbol with guard bands. Two asynchronous users with a delay spread of 2 μsec are present in both of the channel estimation cases. In Fig. 4.9, user 2 arrives at the receiver with an SNR that is 5 dB, 10 dB, or 20 dB lower than user 1. As can be seen from Fig. 4.9, removing one user from the channel estimation results in an error floor which begins to take effect at around 20 dB, 25 dB, and 35 dB when user 2's SNR is 5 dB, 10 dB, and 20 dB lower than user 1 respectively. The reason for the delay in the error floor results from the fact that the processing gain suppresses the interference. Since a processing gain of $W/R = 32$ (15 dB) is used for these results, the error floor begins at around $(15 + x)$ dB when user 2's SNR is x dB below user 1. It can also be observed from Fig. 4.9 that the MMSE multiuser channel estimator is near-far resistant. The results for users 1 and 2 are both plotted against each user's *own* SNR defined in (4.20). As can be seen in Fig. 4.9, even when user 2 arrives at the receiver with an SNR that is 20 dB below user 1, it performs as if it were detected in thermal noise only.

The MMSE multiuser channel estimator proposed here reduces to that in [58] for a single user system, and with the exception of training sequences, it reduces to that in [59] for a TDMA system.

Now that the MMSE multiuser channel estimator has been presented, the performance of the ML multiuser-macrodiversity detector will be analyzed in the following chapter.

Chapter 5

Performance Analysis of the ML-MUMD

This chapter conducts a performance analysis for the ML multiuser-macrodiversity detector. The pairwise error event probability is calculated through the use of Hermitian quadratic forms in complex Gaussian variates [67], and each user's bit error probability is upper bounded by applying the union bound to the appropriate pairwise error events. The appropriate pairwise error events are defined in Section 5.2 which expands upon the methods in [2] and [34]. Section 5.2 defines a new set of indecomposable sequences for the ML multiuser-macrodiversity detector, where the indecomposable sequences are those which cannot be consistently separated into two distinct error events.

5.1 The Pairwise Error Event

This section extends the results of [18] to CDMA and macrodiversity in order to calculate the pairwise error event probability. The total data vector, which includes data symbols for times $-M \leq n \leq M$ and all K users, is defined as

$$\mathbf{b} = \left[b_1\left(-M\right), ..., b_K\left(-M\right), ..., b_1\left(M\right), ..., b_K\left(M\right)\right]^{\mathrm{T}}. \tag{5.1}$$

If the transmitted data vector is assumed to be $\mathbf{b}_j$, the ML multiuser-macrodiversity detector makes an erroneous decision if it selects $\mathbf{b}_i$ where $\mathbf{b}_i \neq \mathbf{b}_j$. Therefore, a pairwise error occurs if $\lambda_i < \lambda_j$, where the log-likelihood function, λ_i, is defined in (2.24) - (2.30). The probability of pairwise error is given as $P\left(d_{ij} < 0\right)$ where $d_{ij} = \lambda_i - \lambda_j$.

Since both $\mathbf{y}_{\psi_l}$ and $\mathbf{v}_{\psi_l}$ are vectors with complex Gaussian components, λ_{il} in (2.25) is a quadratic form in complex Gaussian variates. By modifying the format of (2.25), d_{ij} can be written as

$$\begin{aligned} d_{ij} &= \sum_{l=1}^{L} (\lambda_{il} - \lambda_{jl}) \\ &= \sum_{l=1}^{L} \begin{bmatrix} \mathbf{y}_{\psi_l}^{\dagger} & \mathbf{v}_{\psi_l}^{\dagger} \end{bmatrix} \mathbf{F}_{ij,l} \begin{bmatrix} \mathbf{y}_{\psi_l} \\ \mathbf{v}_{\psi_l} \end{bmatrix}. \end{aligned} \tag{5.2}$$

In (5.2), $\mathbf{F}_{ij,l}$ is given as

$$\mathbf{F}_{ij,l} = \begin{bmatrix} \mathbf{0} & [\mathbf{F}_{ij,l}]_{[1,2]} \\ [\mathbf{F}_{ij,l}]_{[2,1]} & [\mathbf{F}_{ij,l}]_{[2,2]} \end{bmatrix} \tag{5.3}$$

where

$$[\mathbf{F}_{ij,l}]_{[1,2]} = \frac{1}{I_{o_l} + N_o} (\mathbf{B}_{j,\psi_l} - \mathbf{B}_{i,\psi_l}) \tag{5.4}$$

$$[\mathbf{F}_{ij,l}]_{[2,1]} = [\mathbf{F}_{ij,l}]_{[1,2]}^{\dagger} \tag{5.5}$$

and

$$[\mathbf{F}_{ij,l}]_{[2,2]} = \frac{1}{I_{o_l} + N_o} \left(\mathbf{B}_{i,\psi_l}^{\dagger} \widehat{\mathbf{R}}_{\mathbf{s},\psi_l} \mathbf{B}_{i,\psi_l} - \mathbf{B}_{j,\psi_l}^{\dagger} \widehat{\mathbf{R}}_{\mathbf{s},\psi_l} \mathbf{B}_{j,\psi_l} \right). \tag{5.6}$$

From the definitions of $\mathbf{F}_{ij,l}$ in (5.3) - (5.6), it can be observed that $\mathbf{F}_{ij,l}$ is Hermitian; thus, the quadratic form is real [67], and d_{ij} in (5.2) is real.

In order to calculate the probability of a pairwise error, the inverse Laplace transform (ILT) can be calculated for $\Phi(s)/s$, where $\Phi(s)$ is the characteristic function of the thresholded variable, d_{ij} [61].

According to [67, eq. (B-3-21)], the characteristic function of d_{ij} is

$$\Phi(s) = \prod_{l=1}^{L} \frac{1}{\det(\mathbf{I} + 2s\mathbf{R}_{j,l}\mathbf{F}_{ij,l})} \tag{5.7}$$

where

$$\mathbf{R}_{j,l} = \frac{1}{2} E \left[\begin{bmatrix} \mathbf{y}_{\psi_l}\mathbf{y}_{\psi_l}^{\dagger} & \mathbf{y}_{\psi_l}\mathbf{v}_{\psi_l}^{\dagger} \\ \mathbf{v}_{\psi_l}\mathbf{y}_{\psi_l}^{\dagger} & \mathbf{v}_{\psi_l}\mathbf{v}_{\psi_l}^{\dagger} \end{bmatrix} \middle| \mathbf{b}_j \right]. \tag{5.8}$$

In (5.8),

$$\begin{aligned}\frac{1}{2}E\left[\mathbf{y}_{\psi_l}\mathbf{y}_{\psi_l}^{\dagger}\right] &= \mathbf{R}_{\mathbf{s},\psi_l}\mathbf{B}_{j,\psi_l}\Omega_{\mathbf{c},\psi_l}\mathbf{B}_{j,\psi_l}^{\dagger}\mathbf{R}_{\mathbf{s},\psi_l}^{\dagger} \\ &\quad +\mathbf{R}_{\mathbf{s},\psi_l,\phi_l}\mathbf{B}_{j,\phi_l}\Omega_{\mathbf{c},\phi_l}\mathbf{B}_{j,\phi_l}^{\dagger}\mathbf{R}_{\mathbf{s},\psi_l,\phi_l}^{\dagger} \\ &\quad +N_0\widehat{\mathbf{R}}_{\mathbf{s},\psi_l} \end{aligned} \tag{5.9}$$

$$\frac{1}{2}E\left[\mathbf{y}_{\psi_l}\mathbf{v}_{\psi_l}^{\dagger}\right] = \mathbf{R}_{\mathbf{s},\psi_l}\mathbf{B}_{j,\psi_l}\Omega_{\mathbf{c},\mathbf{v},\psi_l} \tag{5.10}$$

and

$$\frac{1}{2}E\left[\mathbf{v}_{\psi_l}\mathbf{v}_{\psi_l}^{\dagger}\right] = \Omega_{\mathbf{v},\psi_l} \tag{5.11}$$

where $\Omega_{\mathbf{c},\psi_l}$, $\Omega_{\mathbf{c},\mathbf{v},\psi_l}$, and $\Omega_{\mathbf{v},\psi_l}$ have the format shown in (2.20).

If the ML multiuser-macrodiversity detector is applied to both microdiversity and macrodiversity antennas, the total number of antennas, L, is given as $L = L_1L_2$ where there are L_1 macrodiversity antenna arrays and L_2 microdiversity antennas within each antenna array. It is assumed that the microdiversity antennas share the same set of users, and that both the arrival times and estimated arrival times are similar among the microdiversity antennas at any site. Therefore, the $\mathbf{F}_{ij,l}$ defined in (5.3) - (5.6) is identical for each microdiversity antenna within an array. It is also assumed that the antennas within an array are spaced far enough apart to ensure independent fading, but close enough that their $\mathbf{y}_{\psi_l}$ and $\mathbf{v}_{\psi_l}$ are identically distributed. Therefore, $\mathbf{R}_{j,l}$ defined in (5.8) - (5.11) is also identical for each microdiversity antenna within an array. Since both $\mathbf{F}_{ij,l}$ and $\mathbf{R}_{j,l}$ depend only on the macrodiversity antenna array locations, $\Phi(s)$ in (5.7) can be re-written as follows:

$$\Phi(s) = \prod_{l=1}^{L_1} \frac{1}{\left[\det\left(\mathbf{I} + 2s\mathbf{R}_{j,l}\mathbf{F}_{ij,l}\right)\right]^{L_2}}. \tag{5.12}$$

The ILT of $\Phi(s)/s$ is shown in (5.13), and this gives the cumulative probability density function (pdf) of the random variable, d_{ij}.

$$P(d_{ij} < \delta) = \frac{1}{2\pi j}\int_{\sigma-j\infty}^{\sigma+j\infty} \frac{\Phi(s)}{s}e^{s\delta}ds. \tag{5.13}$$

In (5.13), σ is placed within the region of convergence. Through the use of Cauchy's residue theorem [66], the ILT can be also be determined by calculating the residues at the right

plane (RP) or left plane (LP) poles as shown in (5.14) [61].

$$P(d_{ij} < \delta) = \begin{cases} -\sum\limits_{RPpoles} \text{Residue}\left[e^{s\delta}\Phi(s)/s\right], \delta \leq 0 \\ +\sum\limits_{LPpoles} \text{Residue}\left[e^{s\delta}\Phi(s)/s\right], \delta > 0 \end{cases}. \tag{5.14}$$

It follows that the probability of pairwise error is given as

$$P\left(d_{ij} < 0\right) = -\sum_{RPpoles} \text{Residue}\left[\frac{\Phi\left(s\right)}{s}\right]. \tag{5.15}$$

It is fairly simple to invert the characteristic function by residues if $\Phi(s)$ consists of simple poles only. However, if $\Phi(s)$ involves both simple and multiple poles, the ILT of $\Phi(s)/s$ becomes more complex as differentiation is required in order to calculate the residues. As can be seen from (5.12), the characteristic function of the ML multiuser-macrodiversity detector applied to both microdiversity and macrodiversity antennas includes both simple and multiple poles. Previous authors have relied on methods such as numerical integration in order to avoid differentiating by hand when inverting these complicated characteristic functions [61], [63]. However, numerical integration can have problems with stability for closely spaced poles. Appendix A presents a simple technique which provides an exact solution to (5.15). It is able to invert a characteristic function which is composed of an arbitrary number of both simple and multiple poles.

Now that the pairwise error event probability has been calculated, the following section describes how each user's BER is bounded by applying the union bound to the appropriate error events.

5.2 The Union Bound

In order to calculate the upper, or union, bound for each user's bit error probability, the concept of error sequences is introduced. Each data vector realization, $\mathbf{b}_i$, defines an error sequence

$$\boldsymbol{\varepsilon} = \left[\boldsymbol{\varepsilon}\left(-M\right), ..., \boldsymbol{\varepsilon}\left(M\right)\right] \tag{5.16}$$

where

$$\boldsymbol{\varepsilon}\left(n\right) = \left[\varepsilon_1\left(n\right), ..., \varepsilon_K\left(n\right)\right]. \tag{5.17}$$

The elements, $\varepsilon_k(n)$, take values $\{-1, 0, 1\}$, and $\mathbf{b}_i = \mathbf{b} - 2\boldsymbol{\varepsilon}$. For notational convenience, the log-likelihood functions, λ_i and λ_j, will be rewritten as $\lambda(\mathbf{b} - 2\boldsymbol{\varepsilon})$ and $\lambda(\mathbf{b})$ respectively, and the pairwise error probability, $P(d_{ij} < 0) = P(\boldsymbol{\varepsilon})$.

In [34], the upper, or union, bound for each user's bit error probability is given as

$$P_k(n) \leq \sum_{\boldsymbol{\varepsilon} \in \beta_k(n)} 2^{-w(\boldsymbol{\varepsilon})} P(\boldsymbol{\varepsilon}) \tag{5.18}$$

where $\beta_k(n)$ is defined as the set of indecomposable sequences with $\varepsilon_k(n) \neq 0$. The indecomposable sequences are those which cannot be consistently separated into two distinct error events. In (5.18), $w(\boldsymbol{\varepsilon})$ is the Hamming weight of the error sequence; in other words, $w(\boldsymbol{\varepsilon})$ gives the number of non-zero entries in $\boldsymbol{\varepsilon}$. The sum in (5.18) could be performed over all error sequences with $\boldsymbol{\varepsilon}_k(n) \neq 0$. However, many of these error events overlap causing the union bound to diverge [34]. Therefore, the method of summing over only the indecomposable sequences reduces the amount of overlap and tightens the union bound [2], [34]. The indecomposable sequences presented in [2] are valid for multiuser detection on a single antenna with an AWGN channel. The authors of [34] expand the set of indecomposable sequences in [2] for the fading channel, and the resulting set includes the smallest number of channel invariant sequences in the union bound. This section of the thesis further expands the set of indecomposable sequences in [34] in order to include the smallest number of channel invariant and time of arrival (TOA) invariant sequences in the union bound. The indecomposable sequences for the ML multiuser macrodiversity detector need to be TOA invariant because each macrodiversity antenna includes a different set of users, and each user arrives with a unique transmission delay.

The set of channel invariant and TOA invariant indecomposable sequences can be determined by following a similar approach to that taken in [34]. For any pair of error sequences, $\boldsymbol{\varepsilon}'$ and $\boldsymbol{\varepsilon}''$,

$$\begin{aligned} &\lambda\left(\mathbf{b} - 2\left(\boldsymbol{\varepsilon}' + \boldsymbol{\varepsilon}''\right)\right) + \lambda(\mathbf{b}) - \lambda\left(\mathbf{b} - 2\boldsymbol{\varepsilon}'\right) - \lambda\left(\mathbf{b} - 2\boldsymbol{\varepsilon}''\right) = \\ &\sum_{l=1}^{L} \frac{8\,\mathrm{Re}\left[\mathbf{v}_{\psi_l}^{\dagger} \mathbf{E}_{\psi_l}'^{\dagger} \widehat{\mathbf{R}}_{\mathbf{s},\psi_l} \mathbf{E}_{\psi_l}'' \mathbf{v}_{\psi_l}\right]}{I_{o_l} + N_o} \end{aligned} \tag{5.19}$$

where

$$\mathbf{E}_{\psi_l} = diag\left(\mathbf{E}_{\psi_l}(-M), ..., \mathbf{E}_{\psi_l}(M)\right) \tag{5.20}$$

and

$$\mathbf{E}_{\psi_l}(n) = diag\left(\{A_x \varepsilon_x(n)\,\mathbf{I}_{G+1} |\, x \in \psi_l\}\right). \tag{5.21}$$

In accordance with the definition for *decomposable* sequences in [2] and [34], a sequence, $\boldsymbol{\varepsilon}$, is decomposable if it can be represented as $\boldsymbol{\varepsilon} = \boldsymbol{\varepsilon}' + \boldsymbol{\varepsilon}''$ where $\boldsymbol{\varepsilon}'$ is orthogonal to $\boldsymbol{\varepsilon}''$, that is, $\boldsymbol{\varepsilon}'^{\dagger}\boldsymbol{\varepsilon}'' = 0$, and $\mathbf{v}_{\psi_l}^{\dagger}\mathbf{E}_{\psi_l}'^{\dagger}\widehat{\mathbf{R}}_{\mathbf{s},\psi_l}\mathbf{E}''_{\psi_l}\mathbf{v}_{\psi_l} \geq 0$. The sequence, $\boldsymbol{\varepsilon}$, is decomposable when $\mathbf{v}_{\psi_l}^{\dagger}\mathbf{E}_{\psi_l}'^{\dagger}\widehat{\mathbf{R}}_{\mathbf{s},\psi_l}\mathbf{E}''_{\psi_l}\mathbf{v}_{\psi_l} \geq 0$ since $\lambda(\mathbf{b}) < \lambda(\mathbf{b} - 2(\boldsymbol{\varepsilon}' + \boldsymbol{\varepsilon}''))$ when $\lambda(\mathbf{b}) < \lambda(\mathbf{b} - 2\boldsymbol{\varepsilon}')$ and $\lambda(\mathbf{b}) < \lambda(\mathbf{b} - 2\boldsymbol{\varepsilon}'')$.

The above definition for decomposable sequences is valid when there is one antenna, l, in the system. For a system with multiple antennas, this definition can be extended by requiring $\mathbf{v}_{\psi_l}^{\dagger}\mathbf{E}_{\psi_l}'^{\dagger}\widehat{\mathbf{R}}_{\mathbf{s},\psi_l}\mathbf{E}''_{\psi_l}\mathbf{v}_{\psi_l} \geq 0$ for all antennas where $1 \leq l \leq L$.

Assuming that the first two conditions are satisfied, i.e. $\boldsymbol{\varepsilon} = \boldsymbol{\varepsilon}' + \boldsymbol{\varepsilon}''$ and $\boldsymbol{\varepsilon}'^{\dagger}\boldsymbol{\varepsilon}'' = 0$, the third condition, $\mathbf{v}_{\psi_l}^{\dagger}\mathbf{E}_{\psi_l}'^{\dagger}\widehat{\mathbf{R}}_{\mathbf{s},\psi_l}\mathbf{E}''_{\psi_l}\mathbf{v}_{\psi_l} \geq 0\ \forall l$ is investigated in more detail. If the resulting matrix, $\mathbf{E}_{\psi_l}'^{\dagger}\widehat{\mathbf{R}}_{\mathbf{s},\psi_l}\mathbf{E}''_{\psi_l}$, is Hermitian positive semidefinite, then $\mathbf{v}_{\psi_l}^{\dagger}\mathbf{E}_{\psi_l}'^{\dagger}\widehat{\mathbf{R}}_{\mathbf{s},\psi_l}\mathbf{E}''_{\psi_l}\mathbf{v}_{\psi_l} \geq 0$ for an arbitrary $\mathbf{v}_{\psi_l}$ [67]. Further, if $\mathbf{E}_{\psi_l}'^{\dagger}\widehat{\mathbf{R}}_{\mathbf{s},\psi_l}\mathbf{E}''_{\psi_l}$ is Hermitian positive semidefinite for all antennas, then $\boldsymbol{\varepsilon}$ is decomposable into $\boldsymbol{\varepsilon}'$ and $\boldsymbol{\varepsilon}''$. Since $\mathbf{E}'_{\psi_l}$ and $\mathbf{E}''_{\psi_l}$ are two different matrices, the product $\mathbf{E}_{\psi_l}'^{\dagger}\widehat{\mathbf{R}}_{\mathbf{s},\psi_l}\mathbf{E}''_{\psi_l}$ is not always Hermitian positive semidefinite, and in fact it is not always Hermitian.

In order to determine whether or not the error sequence, $\boldsymbol{\varepsilon} = \boldsymbol{\varepsilon}' + \boldsymbol{\varepsilon}''$ is decomposable, we assume that the error event begins at $\varepsilon'_x(n) \neq 0$ with no other errors occurring until $\varepsilon''_k(m) \neq 0$. Since $\boldsymbol{\varepsilon} = \boldsymbol{\varepsilon}' + \boldsymbol{\varepsilon}''$ and $\boldsymbol{\varepsilon}'^{\dagger}\boldsymbol{\varepsilon}'' = 0$, $\varepsilon''_x(n) = 0$ when $\varepsilon'_x(n) \neq 0$ and $\varepsilon'_k(m) = 0$ when $\varepsilon''_k(m) \neq 0$. From the format of $\widehat{\mathbf{R}}_{\mathbf{s},\psi_l}$ in (2.12), it can be observed that the blocks $\mathbf{E}_{\psi_l}'^{\dagger}(n)\,\widehat{\mathbf{R}}_{\mathbf{s},\psi_l}(n,m)\,\mathbf{E}''_{\psi_l}(m)$ and $\mathbf{E}_{\psi_l}'^{\dagger}(m)\,\widehat{\mathbf{R}}_{\mathbf{s},\psi_l}(m,n)\,\mathbf{E}''_{\psi_l}(n)$ occur on opposite sides of the diagonal. Therefore, using the fact that $\widehat{\mathbf{R}}_{\mathbf{s},\psi_l}(n,m) = \widehat{\mathbf{R}}_{\mathbf{s},\psi_l}^{\dagger}(m,n)$, the resulting matrix, $\mathbf{E}_{\psi_l}'^{\dagger}\widehat{\mathbf{R}}_{\mathbf{s},\psi_l}\mathbf{E}''_{\psi_l}$ is Hermitian only if

$$\mathbf{E}_{\psi_l}'^{\dagger}(n)\,\widehat{\mathbf{R}}_{\mathbf{s},\psi_l}(n,m)\,\mathbf{E}''_{\psi_l}(m) = \mathbf{E}_{\psi_l}''^{\dagger}(n)\,\widehat{\mathbf{R}}_{\mathbf{s},\psi_l}(n,m)\,\mathbf{E}'_{\psi_l}(m). \tag{5.22}$$

In the following, it is assumed that $\{x,k\} \in \psi_l$. If the error, $\varepsilon''_k(m)$, occurs during time slot $m = n$, it is obvious that the equality in (5.22) does not hold true since $\widehat{\mathbf{R}}_{\mathbf{s},\psi_l}(n,n)$ is a full matrix, and by definition $\mathbf{E}_{\psi_l}'^{\dagger}(n) \neq \mathbf{E}_{\psi_l}''^{\dagger}(n)$ and $\mathbf{E}''_{\psi_l}(m) \neq \mathbf{E}'_{\psi_l}(m)$. If the error, $\varepsilon''_k(m)$, occurs during time slot $m = n+1$, the equality in (5.22) holds true only if $\widehat{\tau}_{lk} > \widehat{\tau}_{lx}$. When $\widehat{\tau}_{lk} > \widehat{\tau}_{lx}$, $\rho_{xk}(n, n+1, \widehat{\tau}_{lk} - \widehat{\tau}_{lx} - GT_c) = \ldots = \rho_{xk}(n, n+1, \widehat{\tau}_{lk} - \widehat{\tau}_{lx} + GT_c) = 0$ in $\widehat{\mathbf{R}}_{\mathbf{s},\psi_l}(n, n+1)$, and the equality in (5.22) holds since the non-zero elements in $\mathbf{E}'_{\psi_l}(n)$

and $\mathbf{E}''_{\psi_l}(m)$ are multiplied by zero elements in $\widehat{\mathbf{R}}_{\mathbf{s},\psi_l}(n, n+1)$. If the error, $\varepsilon''_k(m)$, occurs during time slot $m > n+1$, the equality in (5.22) holds true for any value of $\widehat{\tau}_{lk}$ since $\widehat{\mathbf{R}}_{\mathbf{s},\psi_l}(n,m) = \mathbf{0}$ for $|m-n| > 1$.

In the discussion above, the properties of $\mathbf{E}'^{\dagger}_{\psi_l}\widehat{\mathbf{R}}_{\mathbf{s},\psi_l}\mathbf{E}''_{\psi_l}$ are investigated for one antenna only. For a sequence to be decomposable, $\mathbf{E}'^{\dagger}_{\psi_l}\widehat{\mathbf{R}}_{\mathbf{s},\psi_l}\mathbf{E}''_{\psi_l}$ needs to be Hermitian positive semidefinite for all l. Since there are different sets of users at each antenna, and since each user arrives with a unique transmission delay, the decomposable sequences need to be TOA invariant. Regardless of the TOA, $\boldsymbol{\varepsilon}$ is guaranteed to be decomposable if the error, $\varepsilon''_k(m)$, occurs during time slot $m > n+1$. When $\varepsilon''_k(m)$ occurs during time slot $m > n+1$, $\varepsilon''_i(n+1) = 0$ for $1 \leq i \leq K$. In other words, $\boldsymbol{\varepsilon}$ is decomposable if it contains K zeros within a single time slot.

To conclude, for the ML multiuser-macrodiversity detector, an error sequence is said to be *indecomposable* if it has no sequence of K consecutive zeros within any one time slot.

There is, however, one problem remaining with the indecomposable sequences defined above. The indecomposable sequences which contain two or more consecutive ISI-only terms cause the union bound in (5.18) to diverge. Two consecutive ISI-only terms occur when $\varepsilon_k(n) \neq 0$, $\varepsilon_k(n+1) \neq 0$, and $w(\boldsymbol{\varepsilon}(n)) = w(\boldsymbol{\varepsilon}(n+1)) = 1$. The Hamming weight, $w(\boldsymbol{\varepsilon}(n))$, gives the number of non-zero entries in $\boldsymbol{\varepsilon}(n)$, and it follows that the Hamming weight of the error sequence, $w(\boldsymbol{\varepsilon})$, is $w(\boldsymbol{\varepsilon}) = \sum_{n=-M}^{M} w(\boldsymbol{\varepsilon}(n))$.

While the ISI-only terms cause difficulties in the union bound for this system, they would not cause the union bound to diverge if the channel were an AWGN channel since the complementary error function, $erfc(x)$, decreases exponentially [62]. Also, the ISI-only terms could be safely included into the union bound for a fading channel if the consecutive data symbols were interleaved causing them to fade independently [63].

In order to show the effect of the ISI-only terms on the union bound for this system, Fig. 5.1 shows the rate at which the union bound tightens in the presence of ISI. In Fig. 5.1, a single user with a delay spread of 1 μsec is detected in the presence of thermal noise at both $L = 1$ antenna and $L = 2$ microdiversity antennas. For a single user system with ISI that affects only the adjacent data symbol, $w(\boldsymbol{\varepsilon})$ corresponds to the length of the error sequence. Therefore, Fig. 5.1 shows the decrease in pairwise error probability for error bursts of length $w(\boldsymbol{\varepsilon})$. As can be seen from the figure, $P(\boldsymbol{\varepsilon})$ decreases according to $1/w(\boldsymbol{\varepsilon})$ for a system with a single antenna, and $P(\boldsymbol{\varepsilon})$ decreases according to $1/w^2(\boldsymbol{\varepsilon})$ for a system with two microdiversity antennas. It should be noted that larger delay spreads also affect

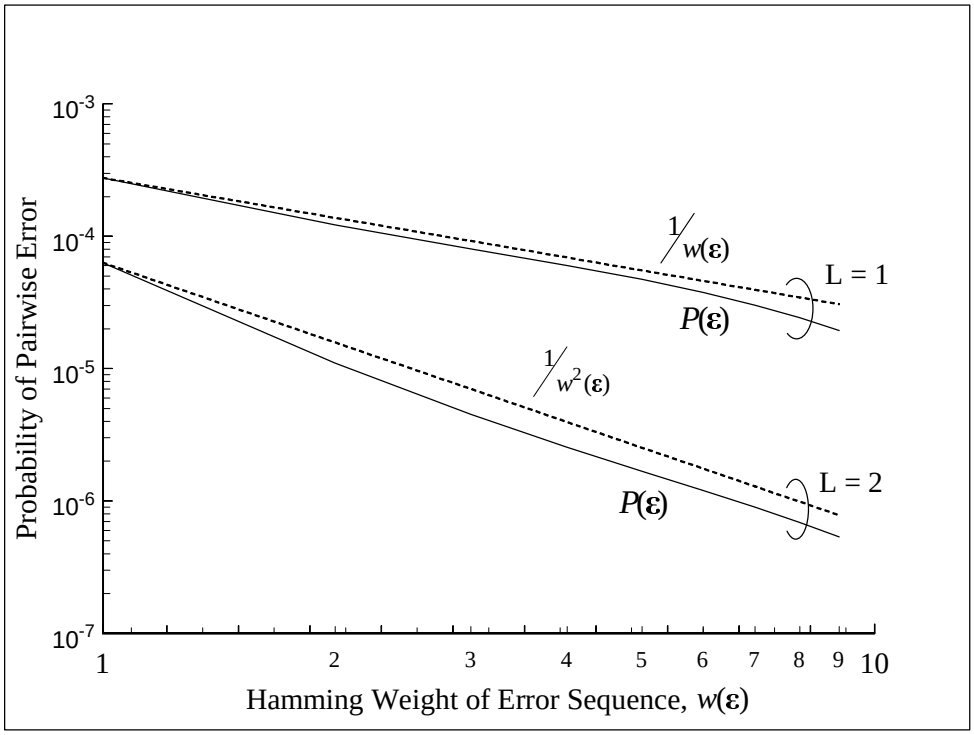

Figure 5.1: The decrease in probability of pairwise error with ISI-only terms.

the slope of $P(\varepsilon)$ vs. $w(\varepsilon)$ as a result of the diversity in the RAKE receiver. Therefore, in general $P(\varepsilon)$ decreases according to $1/w^i(\varepsilon)$, where i is an equivalent order of diversity in a system which employs microdiversity antennas, macrodiversity antennas, and a RAKE receiver.

If the ML multiuser-macrodiversity detector operates with macrodiversity antennas only and a small delay spread, $P(\varepsilon)$ will asymptotically decrease according to $1/w^i(\varepsilon)$ where $i \cong L$. However, with macrodiversity reception and unequal average power levels, the system often operates in the non-asymptotic region, where i is closer to 1. When i is close to 1, the union bound diverges since the sum $\sum_{w(\varepsilon)=1}^{\infty} 1/w(\varepsilon)$ diverges.

In order to prevent the union bound from diverging, the ISI-only terms are simply removed from the union bound. Theoretically, removing the ISI-only terms from $\beta_k(n)$

causes (5.18) no longer to be a true union bound. However, in practice (5.18) is still effectively an upper bound since realistically the ISI-only terms are not among the dominant error events.

Typically in a CDMA system, the symbol duration, T, is much greater than the delay spread, T_d. When $T \gg T_d$, the ISI due to multipath is normally neglected [15]. In Chapter 2, the ISI terms have been included in the ML multiuser-macrodiversity detector for generality since different processing gains affect the length of the symbol duration if the chip rate remains constant, thus causing T_d to occupy a larger portion of T. If a single user were to be detected in the presence of thermal noise only in a CDMA system with a low processing gain, the ISI terms would compose the dominant error events in the union bound. However, in a multiuser CDMA system with a moderate to high processing gain as studied in this thesis, the ISI component of the received signal is insignificant when compared to the MAI generated by other users.

With the exception of the error sequences that involve ISI-only terms, the sequences in $\beta_k(n)$ include the indecomposable sequences which have no occurrence of K consecutive zeros within any one time slot.

To conclude, the union bound in (5.18) upper bounds each user's bit error probability, and it is calculated by summing over the infinite number of sequences in $\beta_k(n)$ until the remaining terms can be neglected. The analysis presented in this section is used to determine the performance of the ML multiuser-macrodiversity detector, and the results are investigated in the following chapter.

Chapter 6

ML-MUMD Performance Results

This chapter investigates the performance of the ML multiuser-macrodiversity detector in both outdoor and indoor wireless communications systems. The outdoor system consists of two adjacent cells as shown in Fig. 6.1. Three different indoor systems are investigated including a single story building with two antennas per floor (Fig. 6.10), a two story building with two vertically aligned antennas (Fig. 6.16), and a two story building with two offset antennas (Fig. 6.21).

The outdoor and indoor results are calculated using the performance analysis presented in Chapter 5. These theoretical results are verified through simulations which show that the theoretical error probabilities correspond well with the simulated results.

In order to evaluate the performance of the ML-MUMD, a power control algorithm is used which approximately equalizes the performance for all users, and a multistage approach is adopted, where one macrodiversity link is added at a time. The power control algorithm and the link selection technique presented in this chapter are both heuristic in nature. While these algorithms are heuristic, they are designed specifically for the ML multiuser-macrodiversity detector since they exploit the theory developed in previous chapters. There are many algorithms possible for power control and link selection, and future research may uncover algorithms which outperform those presented in this chapter and improve the performance of the ML multiuser-macrodiversity detector beyond that reported in this thesis.

6.1 Introduction

The performance analysis conducted in the previous chapter is used to calculate the error probability results for both the outdoor and indoor wireless systems. While the analysis is general and can be used with any synchronization technique and any channel estimation technique, the performance of the ML multiuser-macrodiversity detector is heavily dependent on the accuracy of both the synchronization and the channel estimation. In order to determine the ML-MUMD results with imperfect synchronization, the timing estimation errors, $\{(\tau_{lk} - \widehat{\tau}_{lk})\}$, which range from $-T_c/2 \leq \tau_{lk} - \widehat{\tau}_{lk} \leq T_c/2$ for all l and k, are generated using a truncated Gaussian distribution. The standard deviation of the truncated Gaussian distribution is taken from the results of [55]. The MMSE multiuser channel estimator presented in Chapter 4 uses the timing estimates and provides accurate channel estimates that can be used in the ML-MUMD.

In order to focus solely on the benefit of using macrodiversity with multiuser detection, a simplified system is investigated that does not include the convolutional codes that are typically used in DS-CDMA systems. Regardless of whether an outdoor or an indoor system is investigated, the users are randomly placed into the areas of interest, and fading channel statistics are generated for each different physical scenario. The transmitted signals are assumed to undergo path loss, lognormal shadowing, and Rayleigh fading. Once the channel statistics are known for each user, the detector's performance can be evaluated analytically as discussed in Chapter 5. The detector's performance depends on ψ_l and ϕ_l, where the users in ψ_l are included in the MUMD at antenna l, while the users in ϕ_l are treated as MAI. However, each time a macrodiversity link is added, ψ_l and ϕ_l contain different sets of users, and the performance of the ML-MUMD changes. Therefore, a multistage approach is implemented by adding one macrodiversity link at a time, and the performance of the ML-MUMD is evaluated at each stage. Since the links are added one at a time, the number of stages is equal to the number of additional, or macrodiversity, links. It should be noted that the addition of each macrodiversity link to a particular antenna results in an exponential increase in the computational complexity of the ML-MUMD at that antenna alone since the CMM algorithm localizes the calculations.

The mean square values for the effective bit energy to interference and noise density

ratio, Γ, for each antenna and user combination are given by

$$\Gamma_{lk}^{(m)} = \frac{\left(A_k^{(m)}\right)^2 \sum_{g=0}^{G} \sigma_{c,lkg}^2}{I_{o_l}^{(m)} + N_o} \tag{6.1}$$

where $\Gamma_{lk}^{(m)}$ is defined as the m^{th} stage effective bit energy to interference and noise density ratio for user k at antenna l. A_k is user k's amplitude factor, and as a result of power control, $A_k^{(m)}$ may change during the various stages of macrodiversity. In (6.1) I_{o_l} is given by (2.23), and $I_{o_l}^{(m)}$ is defined as the m^{th} stage effective interference at antenna l. Since there are a total of LK possible links, and each user is initially connected to one antenna, the number of additional links, m, ranges from $0 \leq m \leq K\,(L-1)$.

In general there are L^K different possible combinations for the initial connections. At first it may appear obvious that the initial connections would be chosen based on the values of $\left\{\Gamma_{lk}^{(0)}\right\}$. However, $\left\{\Gamma_{lk}^{(0)}\right\}$ depend on the initial connections, and we have a circular problem. Therefore, in order to select the initial connections, each user, k, is connected to the antenna with the largest $\sum_{g=0}^{G} \sigma_{c,lkg}^2$. This is equivalent to ignoring the effects of MAI on each user. Ignoring the MAI is often reasonable since each connection to an antenna effectively reduces the interference to the other users at that antenna as a result of the multiuser detection. Once each user is connected to an antenna, a power control algorithm is used to equalize the performance of the users.

Traditional soft handoff power control is insufficient when applied to a ML-MUMD system. With traditional soft handoff power control, the mobile's power is adjusted based on the measured energy to interference and noise density ratio. However, this energy to interference and noise density ratio assumes that each user's signal is another user's interference and thus does not change with the addition of macrodiversity links. With multiuser detection, the users which are detected at an antenna interfere very little with each other, and the effective energy to interference and noise density ratio in (6.1) is an improved measure for a ML-MUMD system. However, the effective energy to interference and noise density ratio in (6.1) is inexact. It assumes that the users in multiuser detection do not interfere with each other whatsoever when in fact there will be some interference between these users as a result of the imperfect synchronization and imperfect channel estimation. Further, it assumes that the users that do interfere with each other are simply suppressed by the processing gain; however, the actual cross-correlation between the pseudonoise sequences may cause differences in the level of interference. Therefore, (6.1) is best viewed as an estimate of the

effective energy to interference and noise density ratio. Each time a macrodiversity link is added, the estimate changes correspondingly. If the soft handoff power control algorithm is applied at each stage of macrodiversity using the estimated effective energy to interference and noise density ratio in (6.1), the resulting fluctuations in the mobiles' transmit power can lead to confusing results.

The power control algorithm proposed in [25] is attractive since it is developed for a macrodiversity system which uses pre-detection combining. However, similar to traditional soft handoff, this algorithm also assumes that each user's signal is another user's interference since it does not employ any form of multiuser detection. If this algorithm is applied to a ML-MUMD system, it encounters the same difficulties as described above with traditional soft handoff.

In light of these difficulties, a new power control algorithm is proposed in this chapter for a ML-MUMD system. This power control algorithm is very simple and could most likely be improved upon in future work. The power control algorithm attempts to equalize the performance of all users when each user is connected to one antenna only. It does so by targeting a particular effective energy to interference and noise density ratio, Γ_t. The power at each mobile is adjusted according to the following relation

$$p_k^{(0,i+1)} = p_k^{(0,i)} + \frac{\Gamma_t - \Gamma_{lk}^{(0,i)}}{\partial \Gamma_{lk}^{(0,i)} / \partial p_k^{(0,i)}} \tag{6.2}$$

where i denotes an iterative counter, $p_k^{(0,i)} = \left(A_k^{(0,i)}\right)^2$, and $\partial \Gamma_{lk}^{(0,i)} / \partial p_k^{(0,i)} = \sum_{g=0}^{G} \sigma_{c,lkg}^2 / \left(I_{o_l}^{(0,i)} + N_o\right)$. Since every adjustment in power changes the effective interference at each antenna, (6.2) is applied in an iterative fashion until the transmit powers stabilize. At each iteration, the power control algorithm prevents the power at any mobile from going below the minimum or above the maximum allowable transmit power.

Regardless of whether or not transmit power limitations are placed on each mobile, there is no guarantee of meeting a particular Γ_t. However, the power transmitted by each mobile is limited, and if all users cannot meet Γ_t, it is reduced by 1 dB at a time until all users can achieve it within their prescribed power limits. Since Γ_t is reduced until all users are able to achieve it, the fact that all users meet Γ_t does not imply that all, or even any, of the users have an acceptable level of performance.

Once the initial powers have been chosen, Γ_t is no longer used in the additional stages of

macrodiversity for the reasons described above. Therefore, with the addition of a macrodiversity link, the performance for each user changes, and the power control algorithm simply increases the power of the worst case user by 2 dB. The worst case user is defined as the user with the highest BER. If there are a number of worst case users grouped around the same BER, the power is increased for the user within the worst case group that appears to have the least potential. The user with the least potential is determined by first assuming that the MAI for each user is negligible; then, the error probability of diversity reception with unequal SNRs is estimated in the asymptotic region using the expression in [15].

The power increase of 2 dB was chosen empirically. Increasing the power of the worst case user by 2 dB results in a significant improvement for the worst case user while leaving the other users relatively unaffected. Power increases higher than 2 dB begin to degrade the performance for the other users due to the increased level of interference. Each time a user's power is increased by 2 dB, the power control algorithm ensures that it does not exceed the maximum allowable power. Now that the power control algorithm has been discussed, the method for selecting the additional macrodiversity links will be described.

The algorithm which selects the macrodiversity links once again focuses on improving the BER of the worst case user. If user x is currently connected to antenna l, and it is the worst case user, we can boost its performance in two ways. First, we can connect user x to another antenna, thus improving its performance through diversity reception. Or second, we can add a link to antenna l from another user which effectively reduces the interference at antenna l through the action of joint detection. If there are a number of worst case users clustered around the same BER, the boost in performance is estimated for each of these users with both diversity reception and interference reduction as described below. A macrodiversity link could be chosen in an attempt to raise the performance level for the entire cluster of worst case users. However, for simplicity, the chosen macrodiversity link is the one which provides the largest performance boost to any one of the worst case users.

If we wish to improve user x's performance through diversity reception, we connect user x to the antenna j which maximizes

$$\Gamma_{jx}^{(m)} = \max_i \left(\left\{ \Gamma_{ix}^{(m)} \middle| \, x \notin \psi_i^{(m)} \right\} \right). \tag{6.3}$$

Thus, $x \in \psi_j^{(m+1)}$ and

$$\Gamma_{jx}^{(m+1)'} = \left(\frac{\Gamma_{jx}^{(m)}}{1 - \sigma_s^2 \Gamma_{jx}^{(m)}} \right) \tag{6.4}$$

where $\sigma_s^2\Gamma_{jx}^{(m)} < 1$ since $x \notin \psi_j^{(m)}$. In (6.4) $\Gamma_{jx}^{(m+1)'}$ is calculated using the powers from the previous stage, m. Once the power control algorithm has been applied, $\Gamma_{jx}^{(m+1)}$ is calculated with the updated set of powers.

If we wish to improve user x's performance through interference reduction, we connect the user y to antenna l which maximizes

$$\Gamma_{ly}^{(m)} = \max_u \left(\left\{ \Gamma_{lu}^{(m)} \middle| \, u \notin \psi_l^{(m)} \right\} \right). \tag{6.5}$$

Thus, $y \in \psi_l^{(m+1)}$ and

$$\Gamma_{lx}^{(m+1)'} = \left(\frac{\Gamma_{lx}^{(m)}}{1 - \sigma_s^2 \Gamma_{ly}^{(m)}} \right) \tag{6.6}$$

where $\sigma_s^2\Gamma_{ly}^{(m)} < 1$ since $y \notin \psi_l^{(m)}$.

Finally, the diversity reception option is chosen if $\Gamma_{jx}^{(m+1)'} > \left(1 - \sigma_s^2\Gamma_{ly}^{(m)}\right)^{-1}$, and user x is connected to antenna j. Otherwise, interference reduction is selected, and user y is connected to antenna l.

The above power control algorithm and link selection technique are used in both the outdoor and indoor ML-MUMD systems discussed in Sections 6.2 and 6.3 respectively. The following section describes the outdoor system and presents the appropriate ML-MUMD results.

6.2 Outdoor Results

In order to determine the benefit of using ML-MUMD in an outdoor system, users are randomly placed into the non-shaded areas of the two cells shown in Fig. 6.1. For the outdoor system, the power control algorithm operates with a minimum transmit power of -50 dBm and a maximum transmit power of 0 dBW [69]. The receiver noise density is set to $N_o = -169$ dBm/Hz [68]. The delay spread is assumed to be $T_d = 2$ μsec [14] resulting in $G + 1 = 3$ resolvable channel paths for each user since $W = 1/T_c = 1.2288$ MHz. The pilot symbol frame length is chosen to be $N = 20$, and the interpolator order is set to $2Q + 1 = 9$ coefficients. The path loss exponent is chosen to be 3.5, and the shadowing is assumed to be log-normally distributed with a standard deviation of 7 dB. Since it is common to assume an exponential power delay profile (PDP) in urban settings [3], the following results

are produced for an exponentially decreasing PDP. All of the above mentioned parameters were chosen to reflect a typical outdoor system. In contrast, a non-standard processing gain of $W/R = 32$ is commonly used in both this section and the following section to reflect a future PCS system which supports a few high bit rate users at lower processing gains.

In order to account for other cell interference from mobiles that are not involved in the ML-MUMD, we model them as additional thermal noise which is added on to the receiver noise density, N_o. For simplicity, the additional thermal noise is estimated based on the other cell interference produced in a traditional CDMA system. In [10], it is stated that the other cell interference is typically about 60% of the intracell interference. A traditional CDMA system which is 80% loaded has a rise over thermal noise of approximately 7 dB due to intracell interference [68]. However, as a result of the ML-MUMD, the intracell interference and some of the other cell interference will be negligible. Therefore, for an 80% loaded system with other cell interference only, the rise over thermal noise is approximately $7 + 10\log_{10}(0.6) \cong 5$ dB.

Fig. 6.2 illustrates the performance results based on the physical scenario of Fig. 6.1 using the previously described power control algorithm and link selection technique. The $L = 2$ antennas and $K = 4$ randomly placed users constitute a total of $LK = 8$ possible links. Initially, at 0 on the x axes of Fig. 6.2, each user is connected to one antenna, and the multiuser detection is performed on each antenna separately. For the case in Fig. 6.1, users 2 and 4 initially connect to antenna 1, while users 1 and 3 connect to antenna 2. Once the initial connections are formed and each user is connected to one antenna, additional links, which constitute macrodiversity, are added one at a time until there is full connectivity (i.e. each user is connected to both antennas). Full connectivity occurs at 4 on the x axes of Fig. 6.2.

In Fig. 6.2, the probability of error is reported for each user separately. However, the number of additional, or macrodiversity, links is common for all of the plots in the figure. Therefore, with the addition of each link, the number of macrodiversity links increases by 1 for every plot in the figure. As can be seen from Fig. 6.2, even though we focus on improving the performance of the worst case user, the addition of one macrodiversity link has the capability to lower the probability of error for many users. One user will benefit from the additional diversity, while other users will benefit from interference reduction through improved multiuser detection. It can also be seen from Fig. 6.2 that the simulated results, which are based on approximately two million trials, correspond well with the theoretical

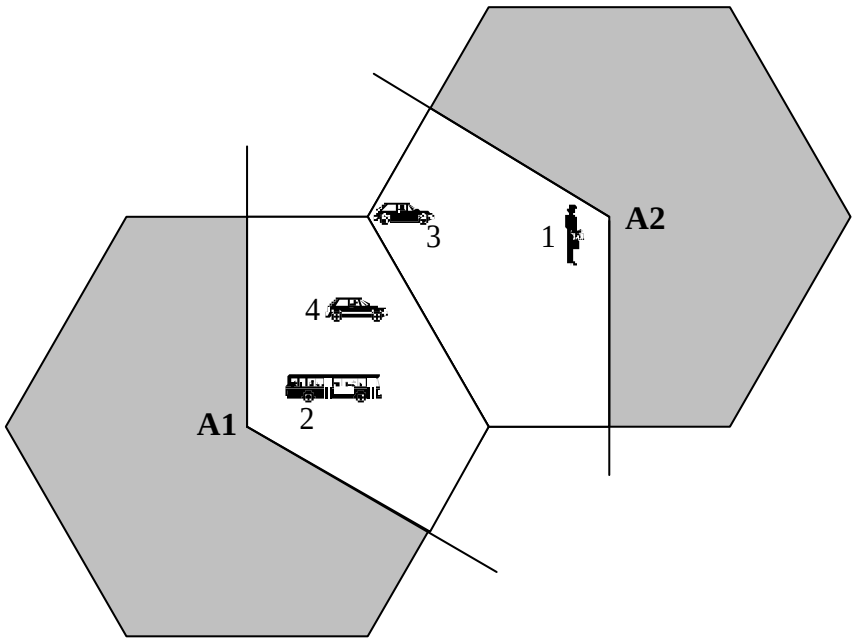

Figure 6.1: Typical physical scenario for an outdoor communications system.

results. For the lower BERs, the simulated results may depart from the theoretical results simply because too few errors were generated in the simulations in order to obtain a reliable average. The simulated results use the CMM algorithm for detection and are based on counting bit errors, while the theoretical results use the methods developed in Chapter 5; however, both are based on Monte Carlo generation of mobile locations and shadowing. At higher BERs, the simulated results depart slightly from the theoretical results since the analysis is performed with a union bound. For example, at stage 0 in Fig. 6.2, the union bound causes a slight artificial increase in the BERs of users 1, 2, and 3. However, user 4 remains relatively unaffected since its dominant error event is well above the rest.

Since the simulated results correspond well with the theoretical results, the following figures are generated using the theoretical performance analysis developed in Chapter 5. To highlight the effect of power control, Fig. 6.3 contains representative results for worst case users and median users with and without power control updates. The power control updates in Fig. 6.3 refer to the 2 dB increases in power for the worst case user at each stage of macrodiversity. In either case, power control is performed at stage 0 for the initial

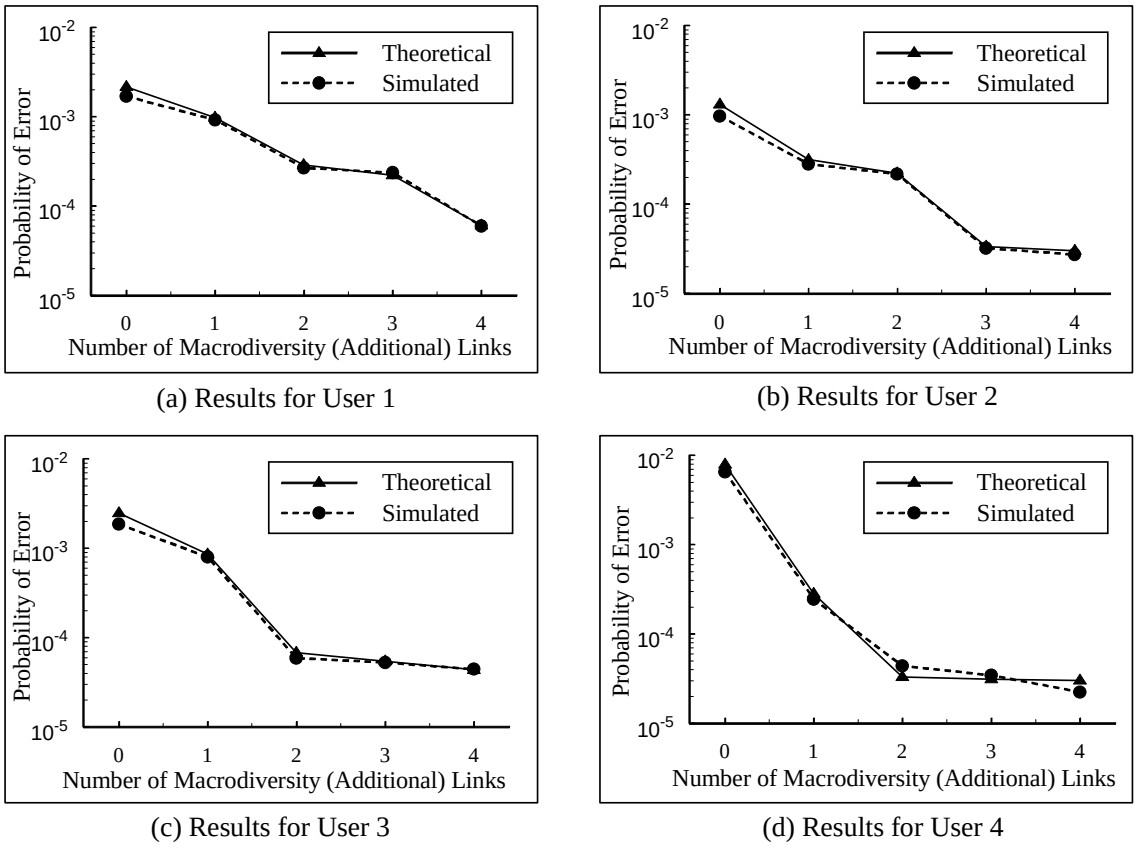

(a) Results for User 1

(b) Results for User 2

(c) Results for User 3

(d) Results for User 4

Figure 6.2: Theoretical and simulated results for the ML-MUMD operating with the physical scenario shown in Fig. 6.1.

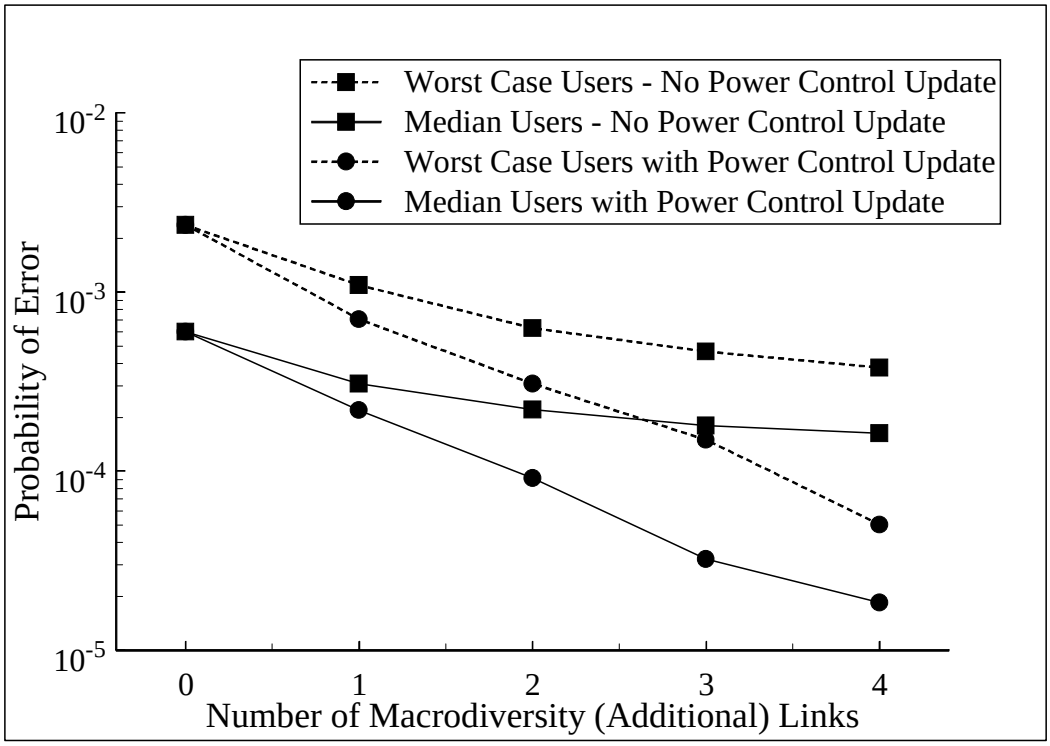

Figure 6.3: ML-MUMD results for antenna arrays of size $L_2 = 2$ operating at $\Gamma_t = 10$ dB.

connections where each user attempts to meet the targeted effective energy to interference and noise density ratio, Γ_t. In Fig. 6.3, $\Gamma_t = 10$ dB, and the results are reported for $L_1 = 2$ macrodiversity antenna arrays of size $L_2 = 2$ microdiversity antennas. It should be noted that the $\Gamma_t = 10$ dB in Fig. 6.3 refers to the originally targeted Γ_t. In certain physical scenarios Γ_t may have to be reduced so that all users can achieve it within their transmit power limits. However, the reported results include all physical scenarios, regardless of whether or not they are able to achieve the original target of $\Gamma_t = 10$ dB.

Fig. 6.3 was generated with 1000 independent trials. For each trial the users are randomly placed into the non-shaded areas of the 2 cells in Fig. 6.1 in order to generate the fading channel statistics. Even though results are presented for both worst case and median users, it is the worst case users that drive the algorithm which adds the macrodiversity links. In order to generate the worst case results, the worst case user is selected at each stage of macrodiversity. In general, these users are different, since adding a macrodiversity link dramatically helps the current worst case user, only to reveal a new worst case user for the next stage. Each of the worst case curves represents the median of the worst case users over 1000 trials. In contrast, the median user is selected at each stage of macrodiversity for the median results; therefore, each of the median curves simply represents the median user over 1000 trials.

As can be seen from Fig. 6.3, the ML multiuser-macrodiversity detector has the capability to improve performance dramatically, especially when it is implemented with power control updates. Without power control updates, the performance of the ML multiuser-macrodiversity detector appears to be limited by a type of error floor. However, with the power control updates, the probability of error for both worst case and median users drops by nearly 2 orders of magnitude as the number of macrodiversity links increases. Even though the algorithm for adding macrodiversity links concentrates on the worst case users, all users respond favorably to the ML-MUMD. It is obvious from the figure that the power control updates have a significant impact on ML-MUMD performance. As this power control update algorithm is very simple, future research would most likely improve upon this algorithm, thus improving the ML-MUMD results.

Fig. 6.4 contains distance related results for the same trials that were used to generate Fig. 6.3. The results in Fig. 6.4 are reported for the median users with power control updates. The near users in Fig. 6.4 refer to the users that are closest to one of the macrodiversity antenna arrays. Specifically, to be in the "near user" category, a user must

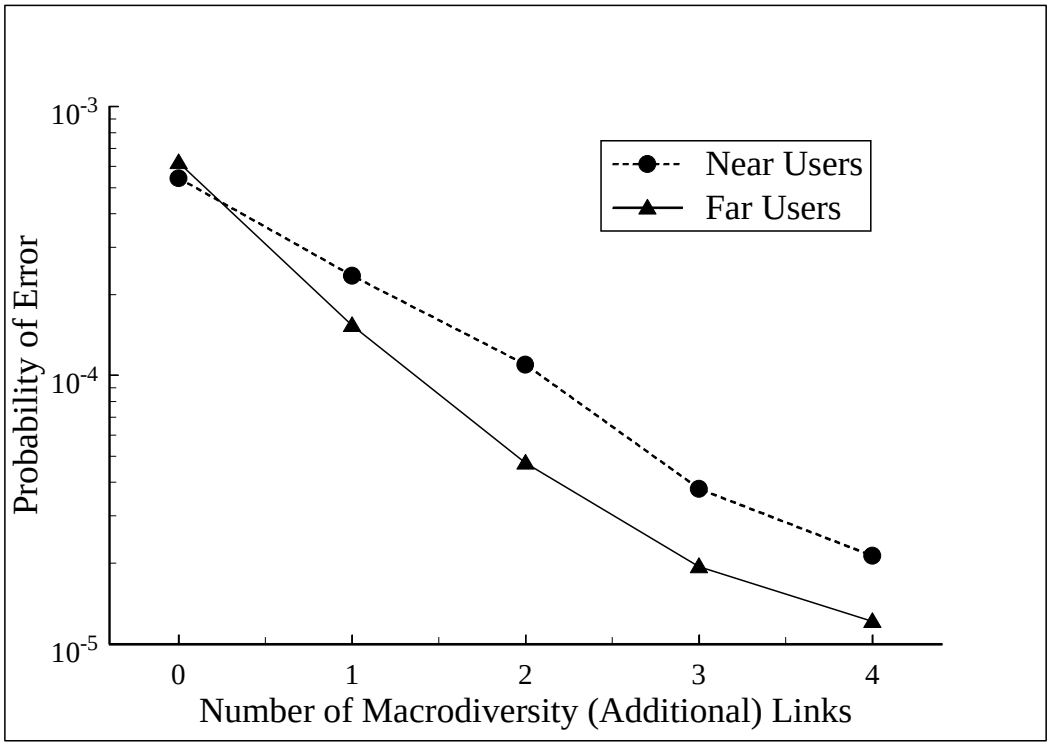

Figure 6.4: Performance of median users segregated by distance for antenna arrays of size $L_2 = 2$ operating at $\Gamma_t = 10$ dB.

be within $R/3$ of the closest antenna, where R is the radius of the cell. To be in the "far user" category, a user must be placed between $2R/3$ and R of the closest antenna. Therefore, intuitively one would expect that the far users would benefit more from the ML-MUMD as they are located in a transition region between the cells. As can be seen from Fig. 6.4, the far users do indeed benefit more from the ML-MUMD. However, the near users enjoy performance gains which are actually fairly close to the gains achieved by the far users. As a result of power control, the near users and far users have similar error probabilities at stage 0 in Fig. 6.4. Therefore, with the addition of macrodiversity links, the far users actually outperform the near users.

Figs. 6.5 and 6.6 report results which are similar to those in Figs. 6.3 and 6.4 respectively. However, the targeted $\Gamma_t = 20$ dB in Figs. 6.5 and 6.6 compared to 10 dB in Figs. 6.3 and 6.4. By comparing Fig. 6.3 with 6.5, it can be seen that the overall probability of error drops dramatically as the targeted effective energy to interference and noise density ratio is increased. The benefit from using macrodiversity increases correspondingly. The probability of error for both the worst case and median users drops by approximately 3 orders of magnitude with the power control updates as the number of macrodiversity links increases. In 6.6, it can be observed that the far users enjoy performance gains that are slightly over 3 orders of magnitude, while the performance gains of the near users are about 2.5 orders of magnitude.

To highlight the effect of changing the targeted Γ_t, the results in Figs. 6.4 and 6.6 are reproduced in Fig. 6.7 for easier comparison. The most notable difference between targeting $\Gamma_t = 10$ dB and $\Gamma_t = 20$ dB is the dramatic drop in error probability as Γ_t is increased. The cost of reducing the BER by increasing Γ_t is an increase in the overall level of transmit power.

In order to show how the transmit power changes with Γ_t, Fig. 6.8 plots the average received SNR against the targeted Γ_t for the initial connections, when each user is connected to a single antenna. The average received SNR in Fig. 6.8 is an average over all users and over 1000 different physical scenarios, where the received SNR for each user is given by (4.20). As can be seen from Fig. 6.8, increasing Γ_t increases the received SNR when $\Gamma_t \leq 20$ dB. However, setting Γ_t higher than 20 dB results in very little change to the average received SNR since the power control algorithm automatically reduces Γ_t if any user is not able to achieve it. The users may not be able to achieve Γ_t for two reasons. First, the targeted Γ_t may not be reached in an interference limited system when the received SNR no longer

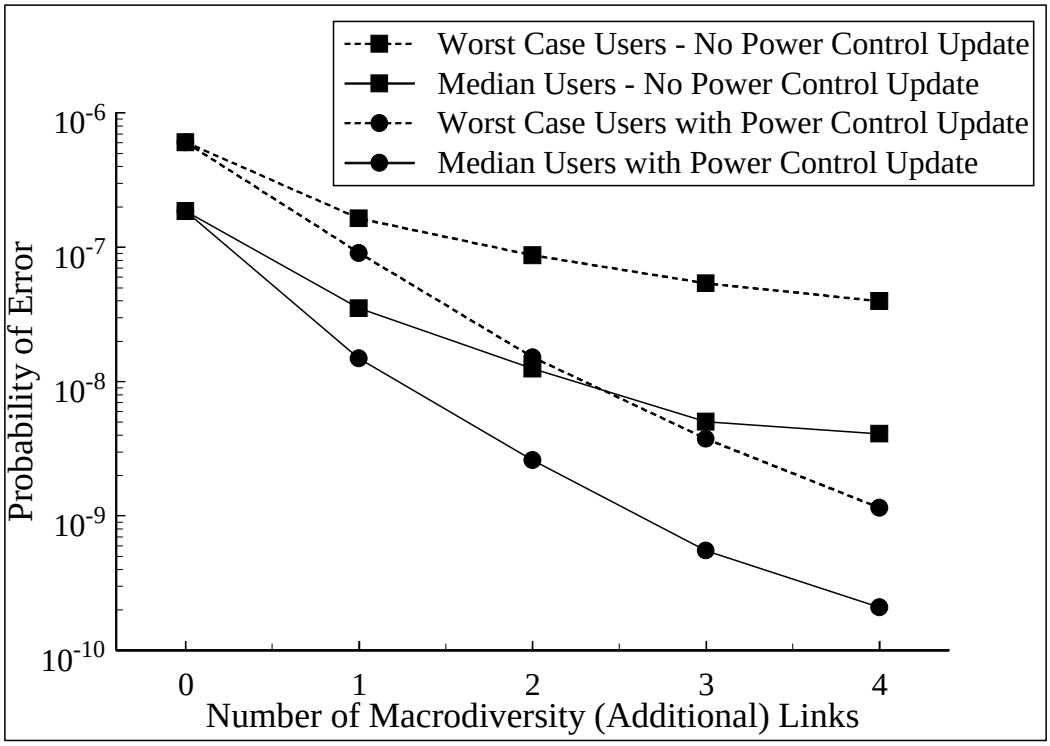

Figure 6.5: ML-MUMD results for antenna arrays of size $L_2 = 2$ operating at $\Gamma_t = 20$ dB.

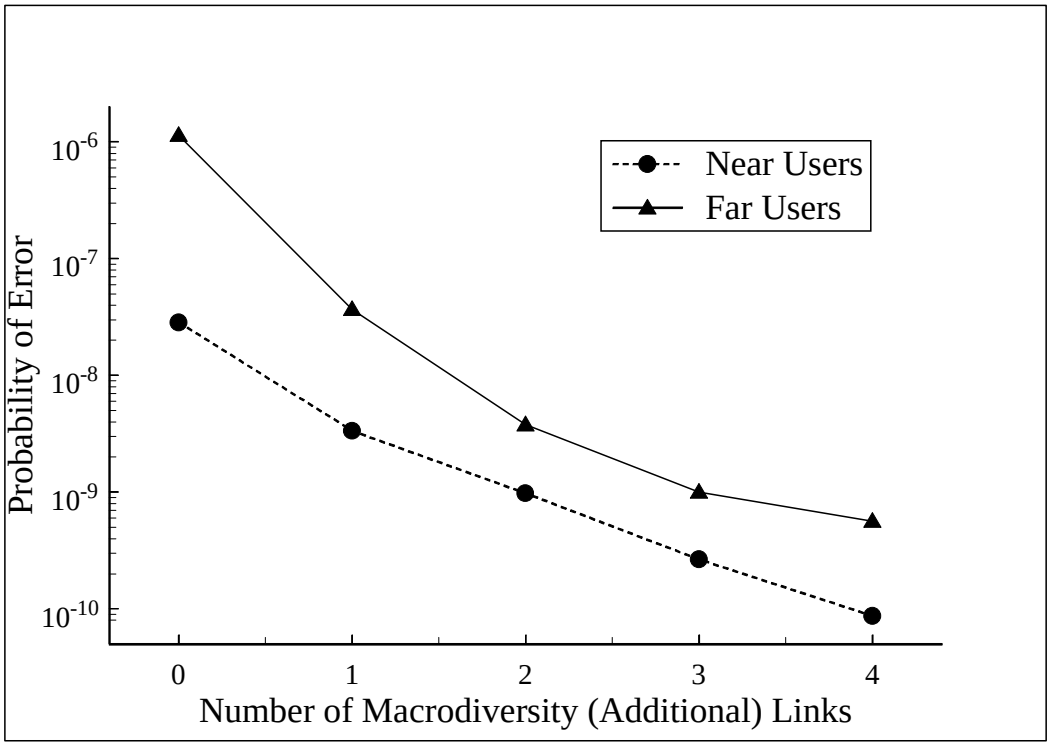

Figure 6.6: Performance of median users segregated by distance for antenna arrays of size $L_2 = 2$ operating at $\Gamma_t = 20$ dB.

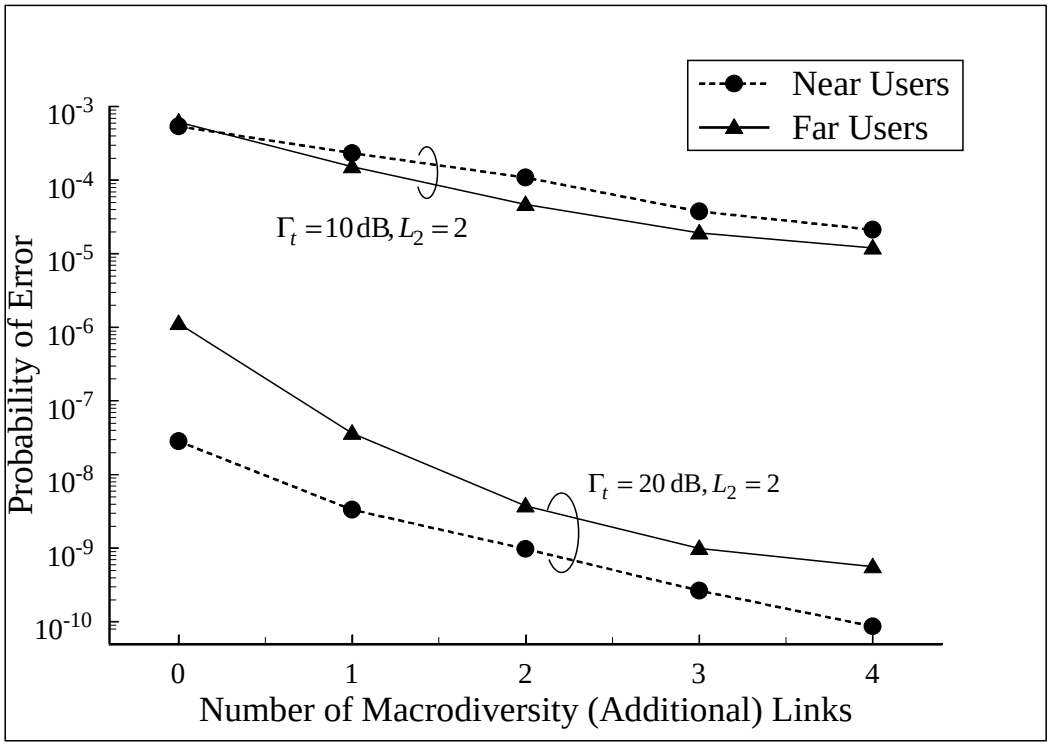

Figure 6.7: Performance of median users segregated by distance for antenna arrays of size $L_2 = 2$ operating at $\Gamma_t = 10$ dB and $\Gamma_t = 20$ dB.

increases with an increase in power. Second, a mobile may not be able to achieve Γ_t simply because its transmit power is limited.

The error bars in Fig. 6.8 show the variation in the received SNR. As expected, the variation increases as the received SNR saturates since each different physical scenario causes the power control algorithm to reduce Γ_t by a different amount.

Since the two setups in Fig. 6.7 operate in the linear portion of the received SNR curve, the error probability drops dramatically as Γ_t is increased from 10 dB to 20 dB. However, increasing Γ_t beyond 20 dB results in very little further improvement. In Fig. 6.7, it can also be seen that the separation between the far users and the near users changes as Γ_t is increased. This results from the fact that the target of $\Gamma_t = 10$ dB is met in 94% of the trials. In contrast, the target of $\Gamma_t = 20$ dB is only met in 32% of the trials. To reiterate, Γ_t may have to be reduced in certain physical scenarios so that all users can achieve it within their transmit power limits. The reported results include all physical scenarios, regardless of whether or not the originally targeted Γ_t was achieved. Therefore, the separation between the near users and the far users for $\Gamma_t = 20$ dB results from the fact that the near users are more likely to be able to achieve $\Gamma_t = 20$ dB.

Fig. 6.9 investigates the effect of processing gain on the ML-MUMD. In contrast with the previous figures, these results are generated for macrodiversity antennas only, i.e. there are no microdiversity antenna arrays and $L_2 = 1$. As can be seen from the figure, the processing gain has very little effect on the performance of the near users as these users can usually meet $\Gamma_t = 20$ dB regardless of the processing gain. In contrast, the far users have a much better chance of meeting $\Gamma_t = 20$ dB when $W/R = 128$ as expected. Similar to the situation shown in Fig. 6.4, the near and far users begin with similar error probabilities at stage 0 when $W/R = 128$. Thus, the additional macrodiversity links cause the far users to outperform the near users.

Now that ML-MUMD has been investigated in an outdoor system, the following section describes 3 different physical scenarios for an indoor system and presents the appropriate ML-MUMD results.

6.3 Indoor Results

The three dimensional environment of an indoor wireless system presents new opportunities in the area of macrodiversity combining. A mobile unit could be potentially connected to

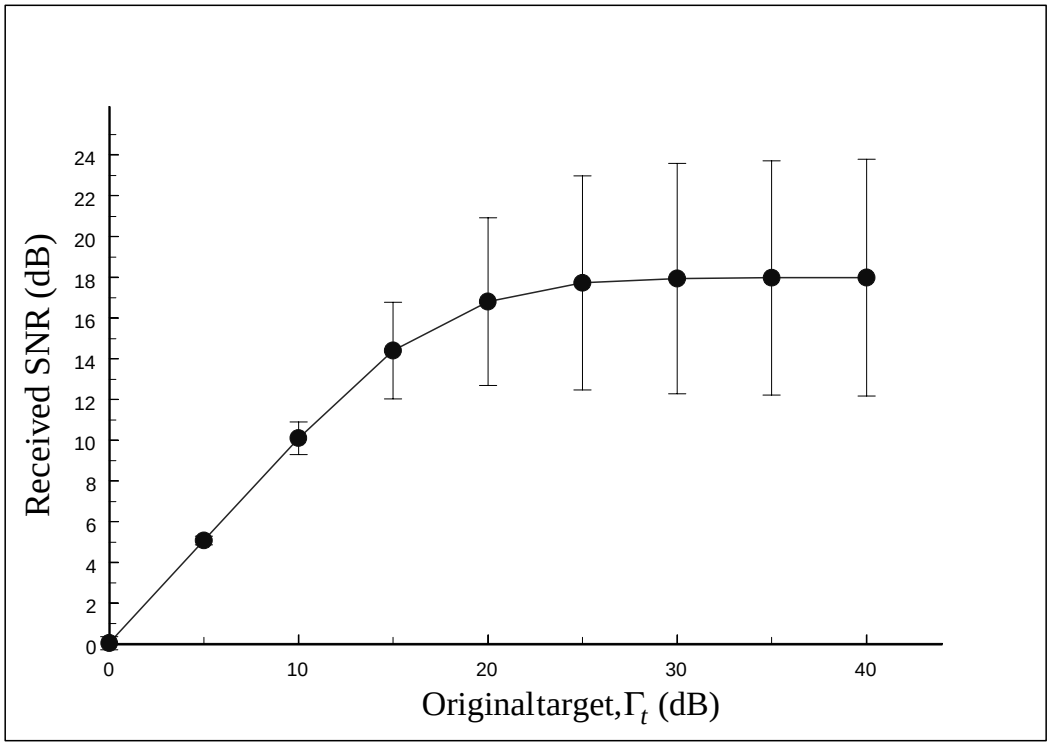

Figure 6.8: The effect of Γ_t on the received SNR for the outdoor system in Fig. 6.1.

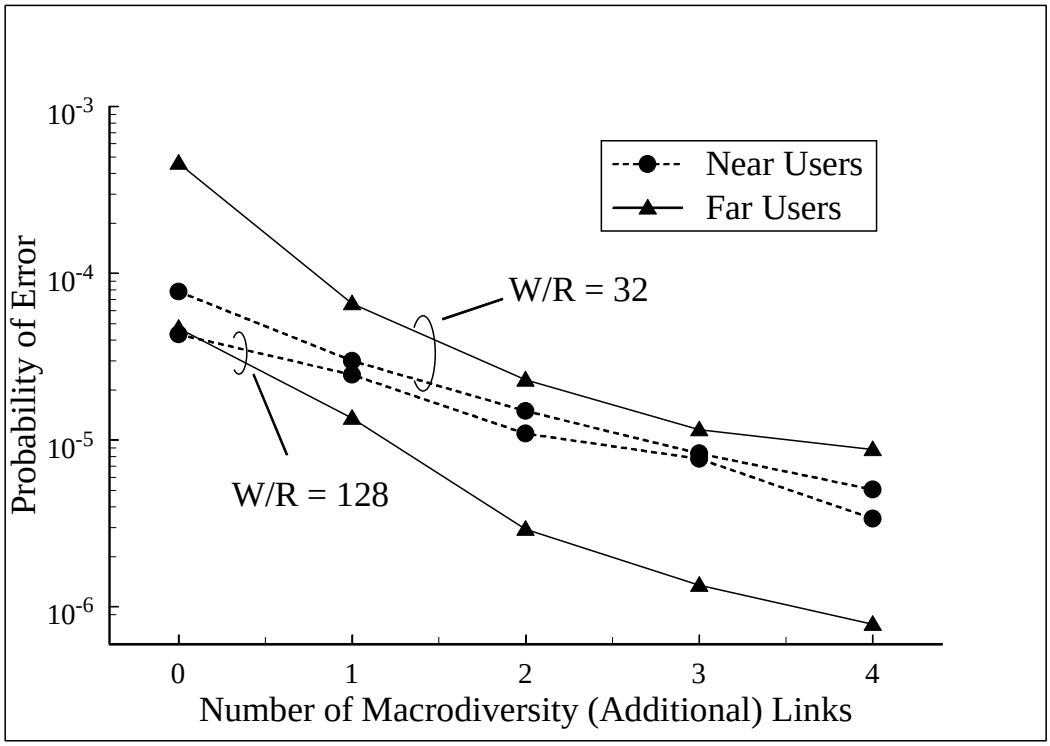

Figure 6.9: Performance of median users segregated by distance for macrodiversity antennas where $L_2 = 1$ operating at $\Gamma_t = 20$ dB.

multiple antennas on the same floor along with antennas on floors located above and below the mobile unit. The performance of the ML multiuser-macrodiversity detector is evaluated for three different situations. First, a single story building is considered with antennas placed in two locations along the main diagonal of the floor as shown in Fig. 6.10. Second, a two story building is considered, where each floor contains one centrally located antenna, or antenna array, as shown in Fig. 6.16. Finally, another two story building is considered, where each floor contains a single antenna, or antenna array, which is placed along the main diagonal of the floor as shown in Fig. 6.21. Users are added to the floor(s) of the building in a random fashion, and fading channel statistics are generated for each different physical scenario. The transmitted signals are assumed to undergo path loss, lognormal shadowing, and Rayleigh fading. For the two story buildings, correlated shadowing is incorporated between the floors of the building based on recent studies in indoor wireless propagation [5], [60].

For the above three indoor systems, the processing gain is set to $W/R = 32$. The power control algorithm operates with a minimum transmit power of -50 dBm and a maximum transmit power of -6 dBW [69]. The delay spread is assumed to be $T_d = 30$ nsec [70] resulting in only $G + 1 = 1$ resolvable channel path for each user since $W = 1/T_c = 1.2288$ MHz. The pilot symbol frame length is chosen to be $N = 100$, and the interpolator order is set to $2Q + 1 = 9$ coefficients. The following parameters for the indoor propagation model are similar to those in [4] which were based on a 1.8 GHz indoor propagation study. The path loss exponent is chosen to be 4. The signals which travel between the floors of a building experience a floor attenuation factor (FAF) which is set to 14.6 dB for a 1 floor separation between the antenna and the user. The shadowing is assumed to be lognormally distributed with a standard deviation of 9.6 or 8.4 dB for a 0 or 1 floor separation between the antenna and the user respectively. The correlated shadowing between the floors of a building is implemented in a similar manner to that proposed in [4].

Figs. 6.12, 6.17, and 6.22 contain representative results for worst case users and median users with and without power control updates for the systems shown in Figs. 6.10, 6.16, and 6.21 respectively. Similar to the outdoor results, these figures were generated with 1000 independent trials, and for each trial the users are randomly placed in the appropriate building in order to generate the fading channel statistics. In Figs. 6.12, 6.17 and 6.22, $\Gamma_t = 20$ dB, and the results are reported for $L_1 = 2$ macrodiversity antenna arrays of size $L_2 = 2$ microdiversity antennas. As can be seen from these graphs, the indoor results are

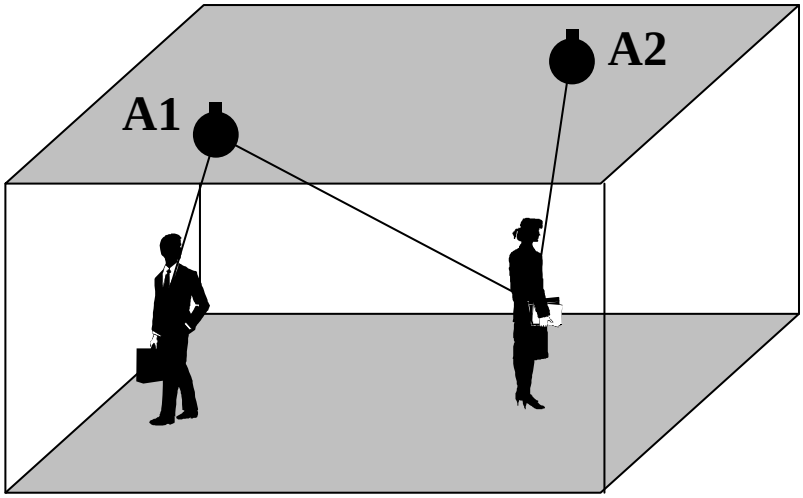

Figure 6.10: An indoor communications system with 2 antennas placed along the main diagonal of the floor.

consistent with the outdoor results, and all users respond favorably to the ML-MUMD even though the algorithm for adding macrodiversity links concentrates on the worst case users. By observing the results in Figs. 6.12, 6.17 and 6.22, it can be seen that both the worst case and median users drop by about 3 orders of magnitude in the single story building and 2 orders of magnitude in the two story buildings.

In a similar way to Fig. 6.8 for the outdoor system, Fig. 6.11 shows how the transmit power changes with Γ_t for the three different indoor systems. The average received SNR is plotted against the targeted Γ_t for the systems shown in Figs. 6.10, 6.16, and 6.21. By comparing Fig. 6.8 with Fig. 6.11, it can be seen that the shape of the received SNR curves for the outdoor system differ from that for the indoor systems. The "S" shaped curves for the indoor systems result from the fact that in the low Γ_t region, the users are often transmitted at the minimum power level of -50 dBm. In the high Γ_t region, the maximum transmit power of -6 dBW is rarely reached; however, the system becomes interference limited causing the received SNR to saturate. The error bars are left out of this figure for clarity. However, unlike the outdoor situation in Fig. 6.8, the variation in received SNR is fairly large for all values of Γ_t. This results from the fact that the minimum transmit power is often invoked in the low Γ_t region and the received SNR saturates in the high Γ_t region.

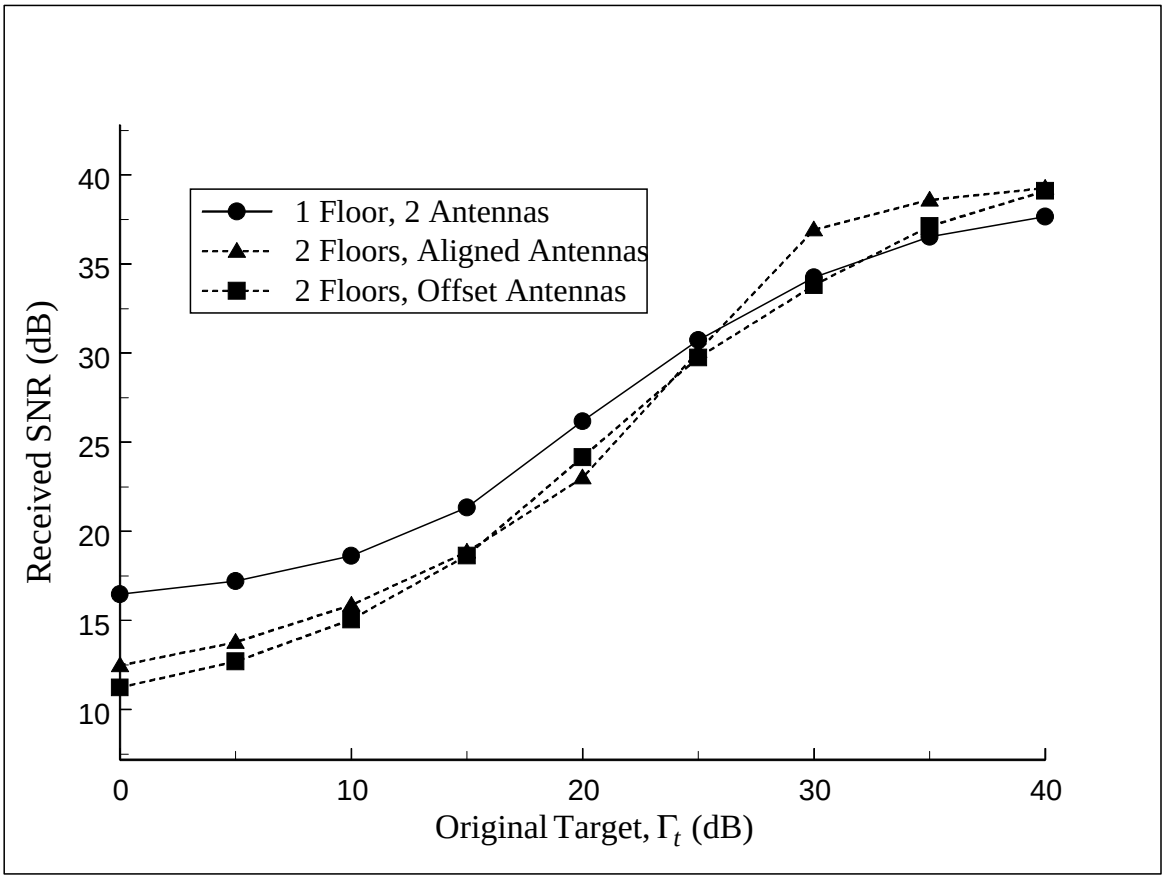

Figure 6.11: The effect of Γ_t on the received SNR for the three indoor communications systems.

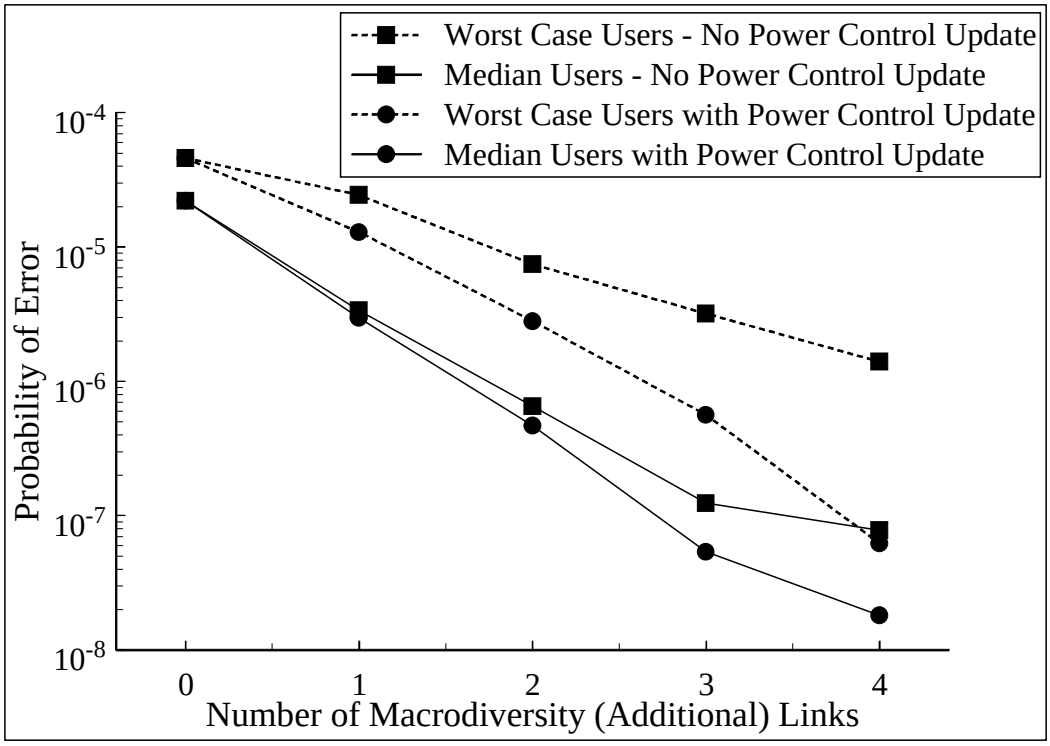

Figure 6.12: ML-MUMD results for the system shown in Fig. 6.10, operating with $L_2 = 2$ and $\Gamma_t = 20$ dB.

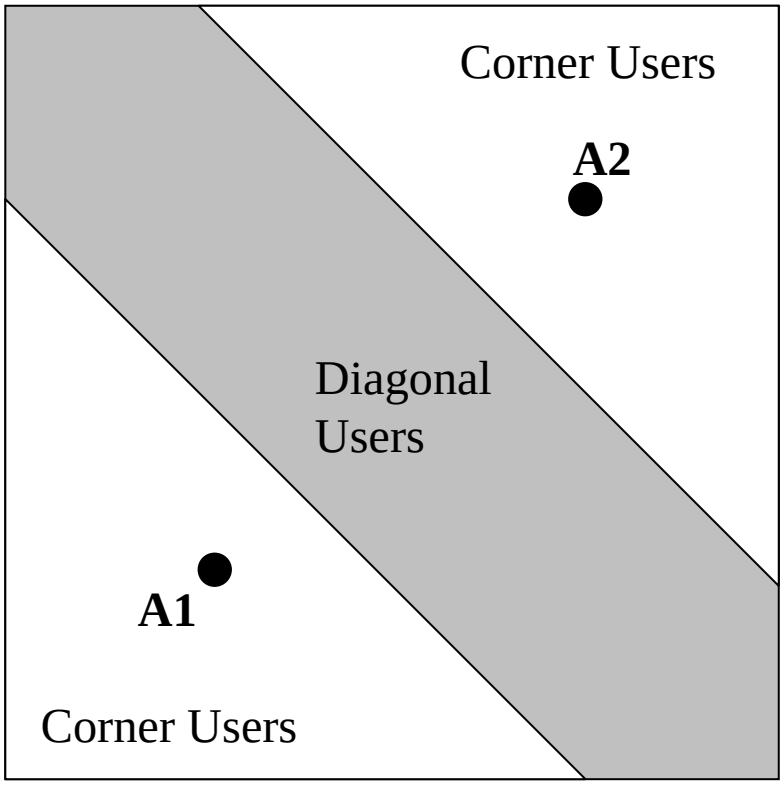

Figure 6.13: Distance sorting for the system shown in Fig. 6.10.

Figs. 6.14, 6.19 and 6.24 contain distance related results for the systems shown in Figs. 6.10, 6.16, and 6.21 respectively. The results in these figures are reported for the median users with power control updates. In all cases, three different setups are studied. The first and second setups target $\Gamma_t = 20$ dB and $\Gamma_t = 30$ dB respectively, and operate with macrodiversity antennas alone where $L_2 = 1$. The third setup targets $\Gamma_t = 20$ dB and operates with macrodiversity antenna arrays of size $L_2 = 2$. In a similar way to that described above, Figs. 6.15, 6.20 and 6.25 contain distance related results for the systems shown in Figs. 6.10, 6.16, and 6.21 when the ML multiuser-macrodiversity detectors target $\Gamma_t = 20$ dB and $\Gamma_t = 30$ dB, and operate with macrodiversity antenna arrays of size $L_2 = 2$.

For the single story building, Fig. 6.13 shows the distance sorting that was used to generate Figs. 6.14 and 6.15. As can be seen from Fig. 6.14, the error probability can be reduced by either increasing Γ_t or increasing the number of microdiversity antennas, L_2. In general, the cost of increasing Γ_t is an increase in the overall level of transmit power. However, as can be seen from Fig. 6.11, increasing Γ_t beyond 30 dB results in very little further improvement. In contrast, the transmit power is left unchanged when the number of microdiversity antennas is increased; however, the cost of increasing L_2 is the need to install an additional antenna. It can be observed from Fig. 6.14 that the diagonal users benefit more from the ML-MUMD as expected. When $\Gamma_t = 30$ dB and $L_2 = 1$, the corner users drop by more than 2 orders of magnitude, while the diagonal users drop by approximately 3 orders of magnitude. When $\Gamma_t = 20$ dB and $L_2 = 2$, the corner users drop by about 3 orders of magnitude, while the diagonal users drop by nearly 4 orders of magnitude. It can be seen in Fig. 6.15 that when $\Gamma_t = 30$ dB and $L_2 = 2$, the results improve further, and the corner users drop by more than 4 orders of magnitude, while the diagonal users drop by nearly 6 orders of magnitude.

For the two story building with centrally located antennas, Fig. 6.18 shows the distance sorting that was used to generate Figs. 6.19 and 6.20. It can be seen from Fig. 6.19 that both the near users and the far users benefit equally from the ML-MUMD. When $\Gamma_t = 30$ dB and $L_2 = 1$, both near and far users drop by about 3 orders of magnitude, and when $\Gamma_t = 20$ dB and $L_2 = 2$, the near and far users drop by about 2 orders of magnitude. The separation between the near and far users when $\Gamma_t = 20$ dB appears to be somewhat confusing at first since the target of $\Gamma_t = 20$ dB is met in nearly all of the trials. However, upon further investigation it turns out that the near users are often transmitting at the minimum transmit power level of -50 dBm. In Fig. 6.20, it can be seen that the near and

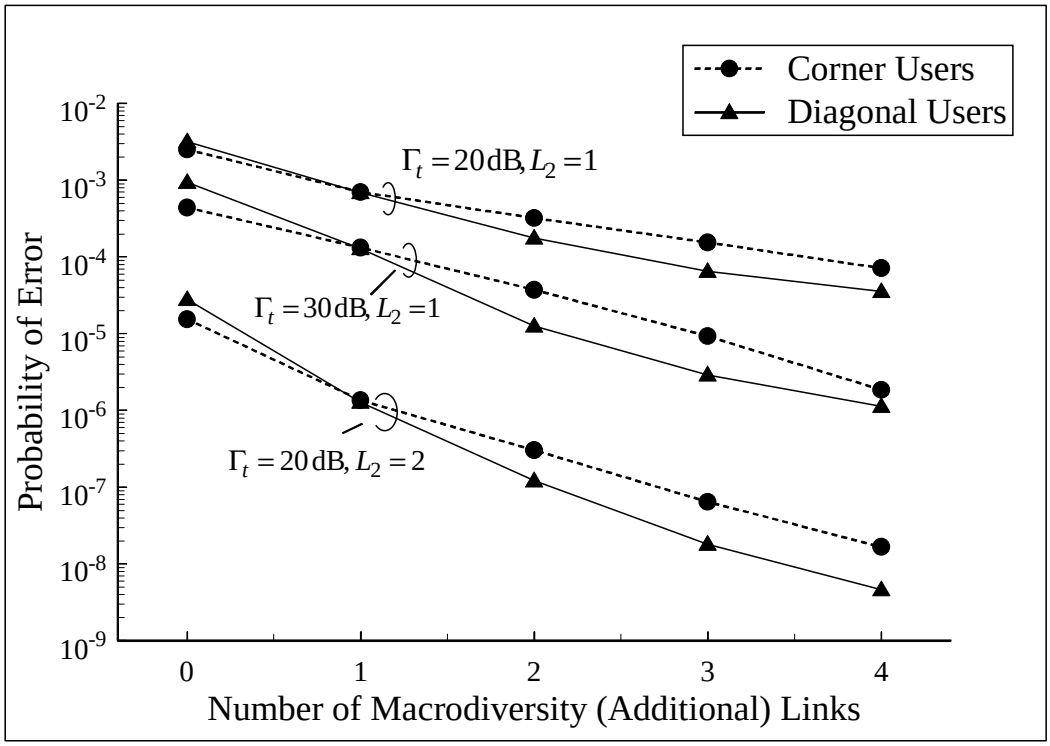

Figure 6.14: Performance of median users segregated by distance for the system shown in Fig. 6.10.

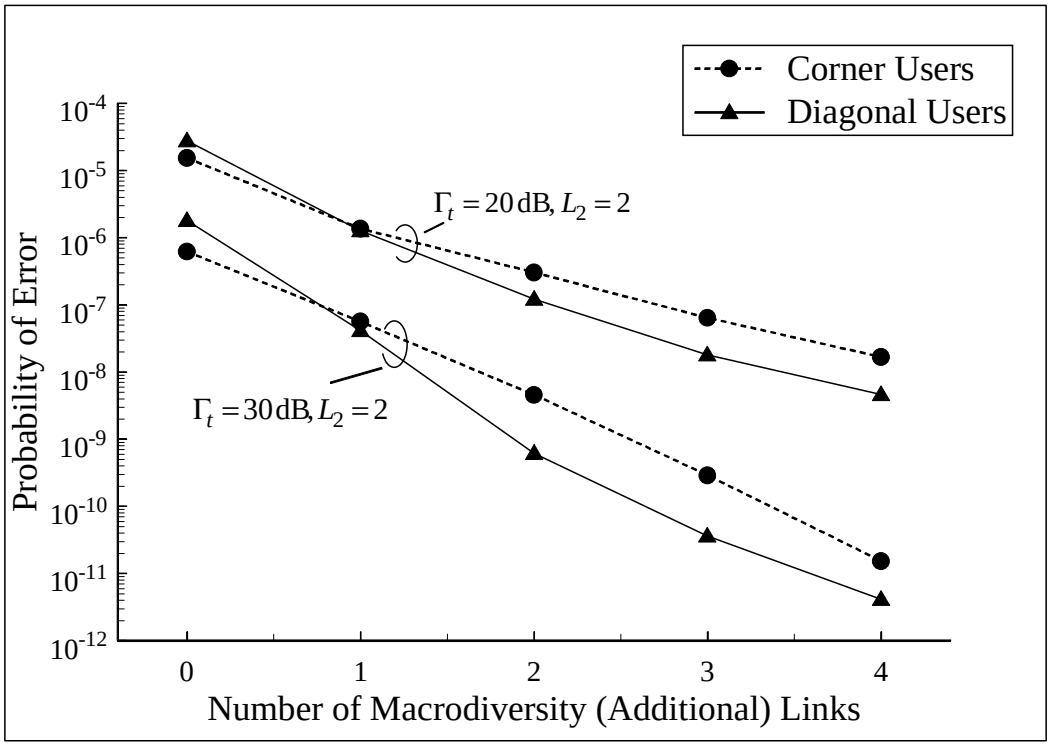

Figure 6.15: Performance of median users segregated by distance for the system shown in Fig. 6.10 operating with $L_2 = 2$.

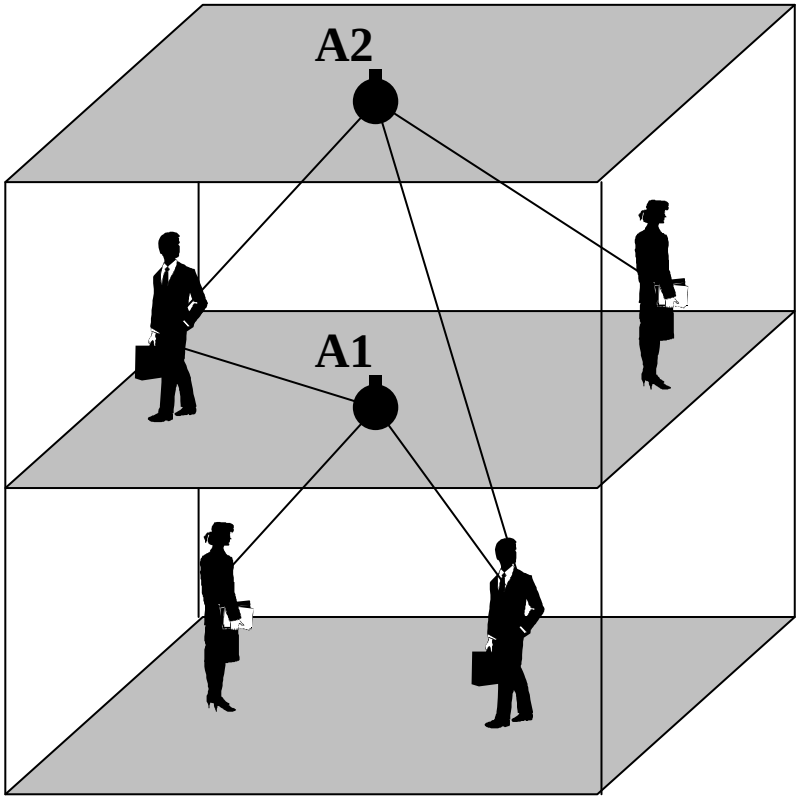

Figure 6.16: An indoor communications system with a centrally located antenna placed on each floor of the building.

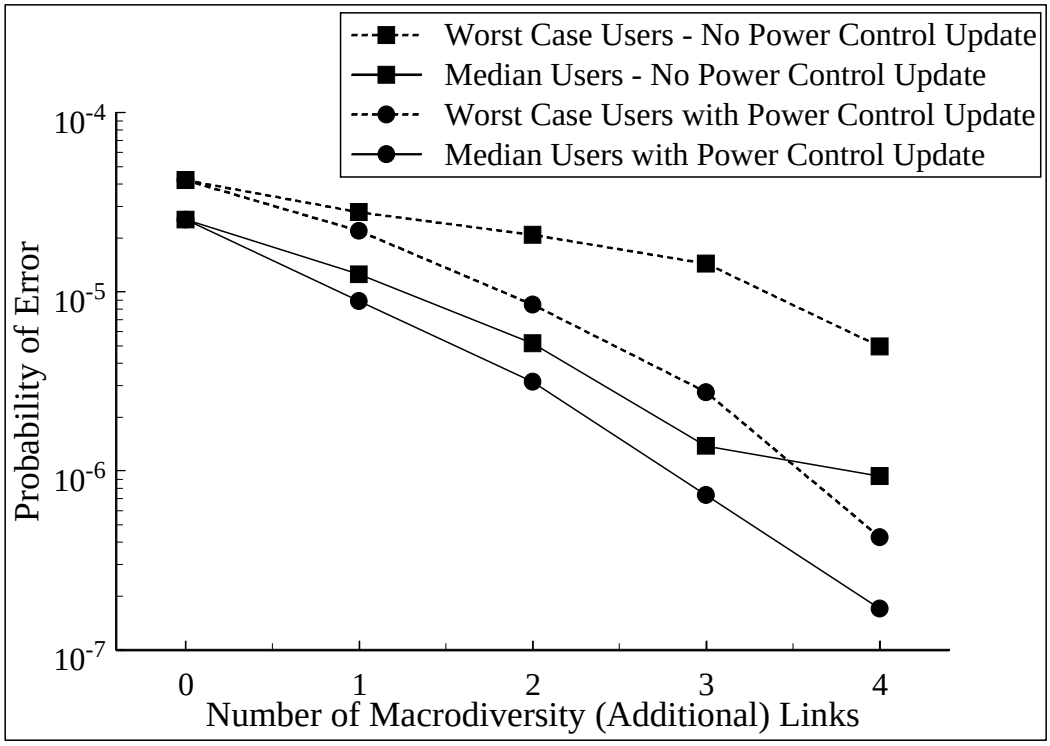

Figure 6.17: ML-MUMD results for the system shown in Fig. 6.16, operating with $L_2 = 2$ and $\Gamma_t = 20$ dB.

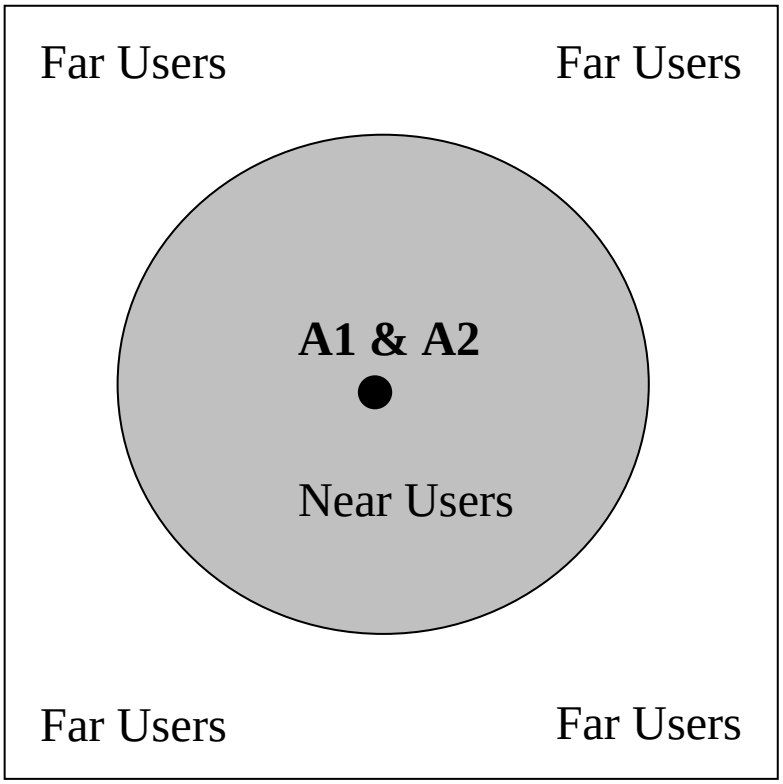

Figure 6.18: Distance sorting for the system shown in Fig. 6.16.

far users drop by nearly 6 orders of magnitude when $\Gamma_t = 30$ dB and $L_2 = 2$.

For the two story building with offset antennas, Fig. 6.23 shows the distance sorting that was used to generate Figs. 6.24 and 6.25. It can be seen from Fig. 6.24 that the far users benefit a great deal more from the ML-MUMD than the near users. When $\Gamma_t = 30$ dB and $L_2 = 1$, the near users drop by about 1.5 orders of magnitude, while the far users drop by nearly 3 orders of magnitude. When $\Gamma_t = 20$ dB and $L_2 = 2$, the near users drop by about 2 orders of magnitude, while the far users drop by 3 orders of magnitude. In Fig. 6.25, it can be seen that the near users drop by about 3 orders of magnitude, while the far users drop by 5 orders of magnitude when $\Gamma_t = 30$ dB and $L_2 = 2$.

It is interesting to compare the results for the system shown in Fig. 6.16 with the results for the system shown in Fig. 6.21 as they both operate with one macrodiversity antenna array per floor in a two story building. In [9] the authors found that as a result of the correlated shadowing between floors of a building, it is best to vertically align the antennas in a traditional CDMA system which does not include either multiuser detection or macrodiversity. In order to determine whether this recommendation holds for a CDMA system which uses ML-MUMD, the results for the vertically aligned antennas in Fig. 6.16 are compared with the results for the offset antennas in Fig. 6.21. By comparing Fig. 6.17 with Fig. 6.22 it is not immediately evident as to which system is superior as both the median and worst case users experience similar gains due to the addition of macrodiversity links. However, by comparing the distance related results in Figs. 6.19 and 6.24, it is obvious that the results for the offset antennas are more distance dependent than those for the vertically aligned antennas. Therefore, in order to provide a similar level of performance for all users, regardless of their placement within the building, the recommendation of vertically aligning the antennas remains unchanged.

6.4 Conclusions

To conclude, the outdoor and indoor ML-MUMD results both show that the addition of one macrodiversity link has the capability to lower the probability of error for many users. The combination of macrodiversity and power control is particularly powerful. Power control alone is clearly limited. Macrodiversity alone produces substantial improvement, but it falls short of the improvement achieved from the combination. The targeted effective bit energy to interference and noise density ratio, Γ_t, affects the ML-MUMD performance,

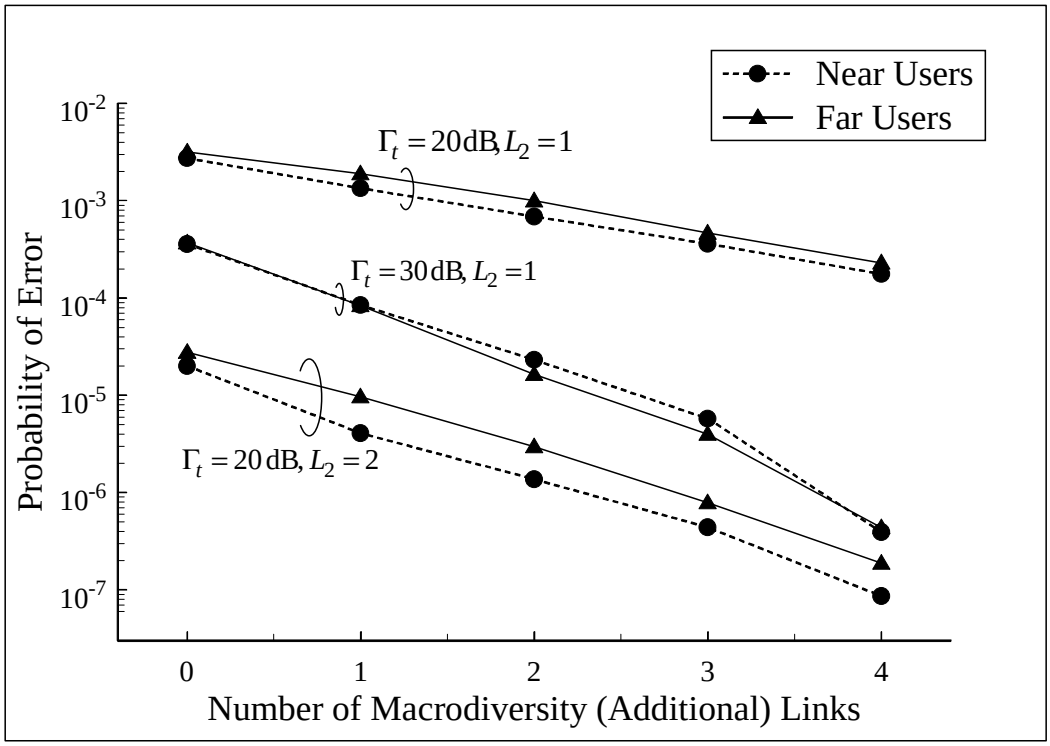

Figure 6.19: Performance of median users segregated by distance for the system shown in Fig. 6.16.

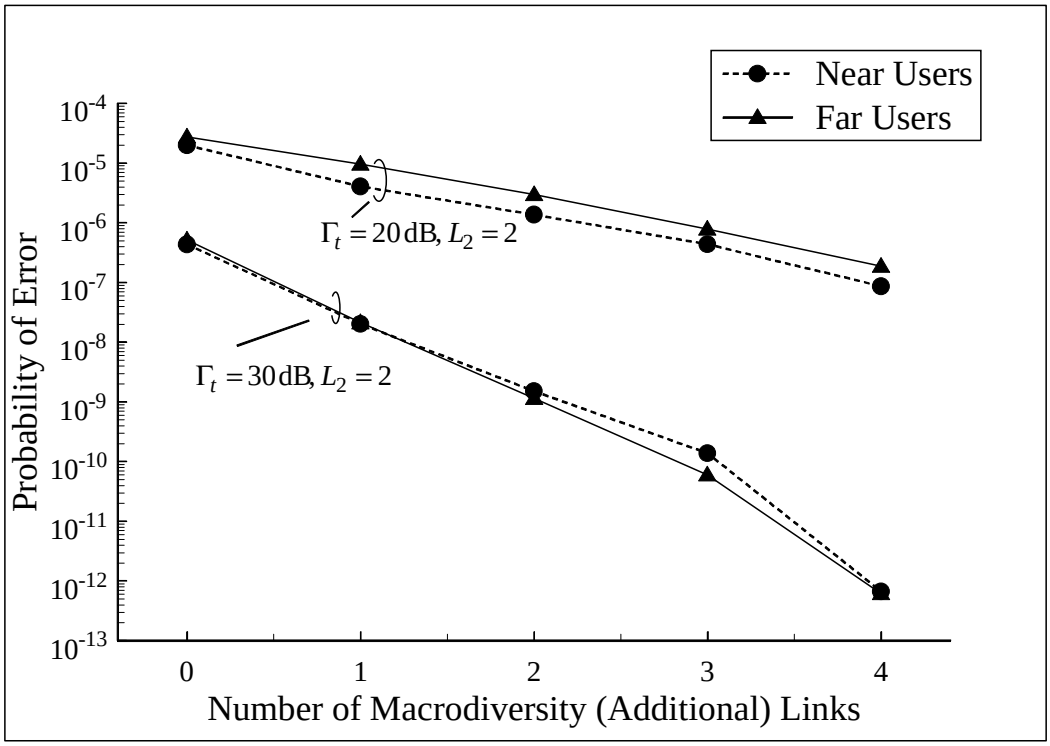

Figure 6.20: Performance of median users segregated by distance for the system shown in Fig. 6.16 operating with $L_2 = 2$.

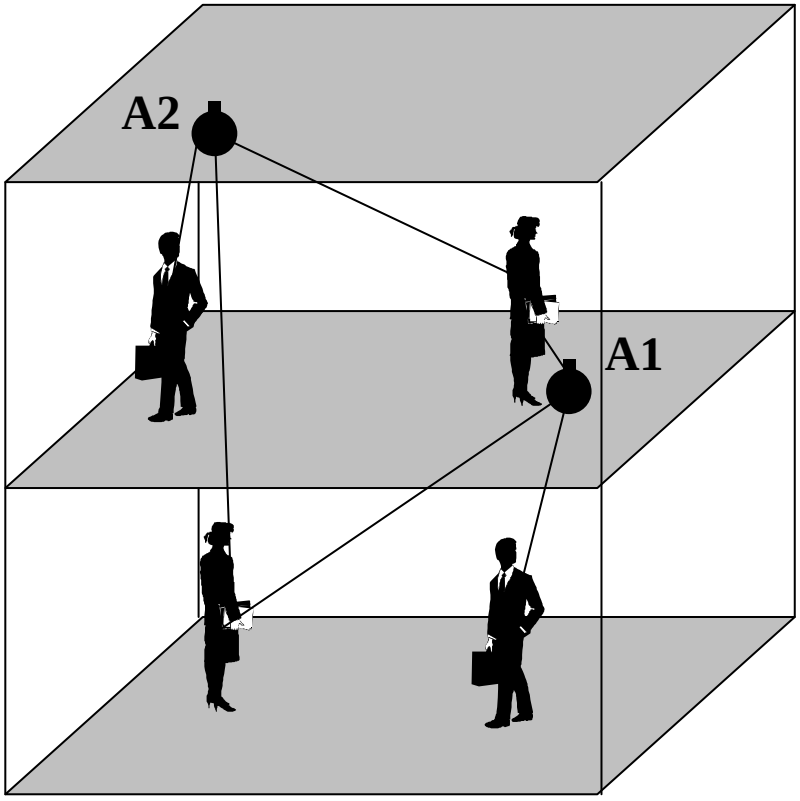

Figure 6.21: A two story indoor communications system where each floor of the building contains a single antenna which is placed along the main diagonal of the floor.

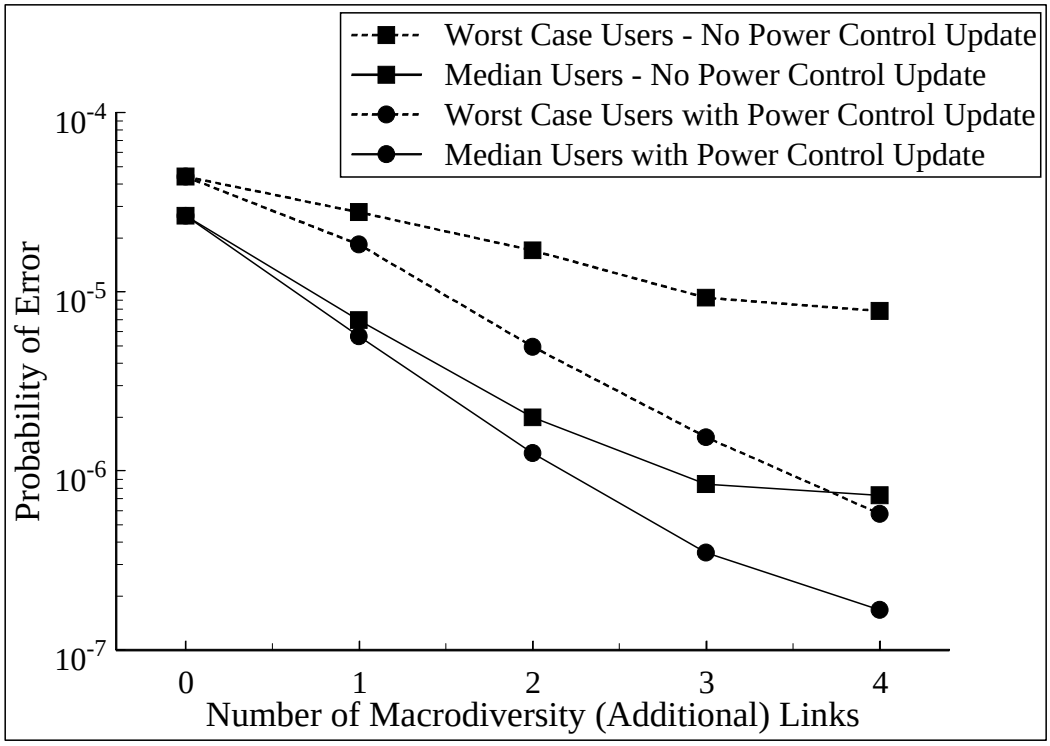

Figure 6.22: ML-MUMD results for the system shown in Fig. 6.21, operating with $L_2 = 2$ and $\Gamma_t = 20$ dB.

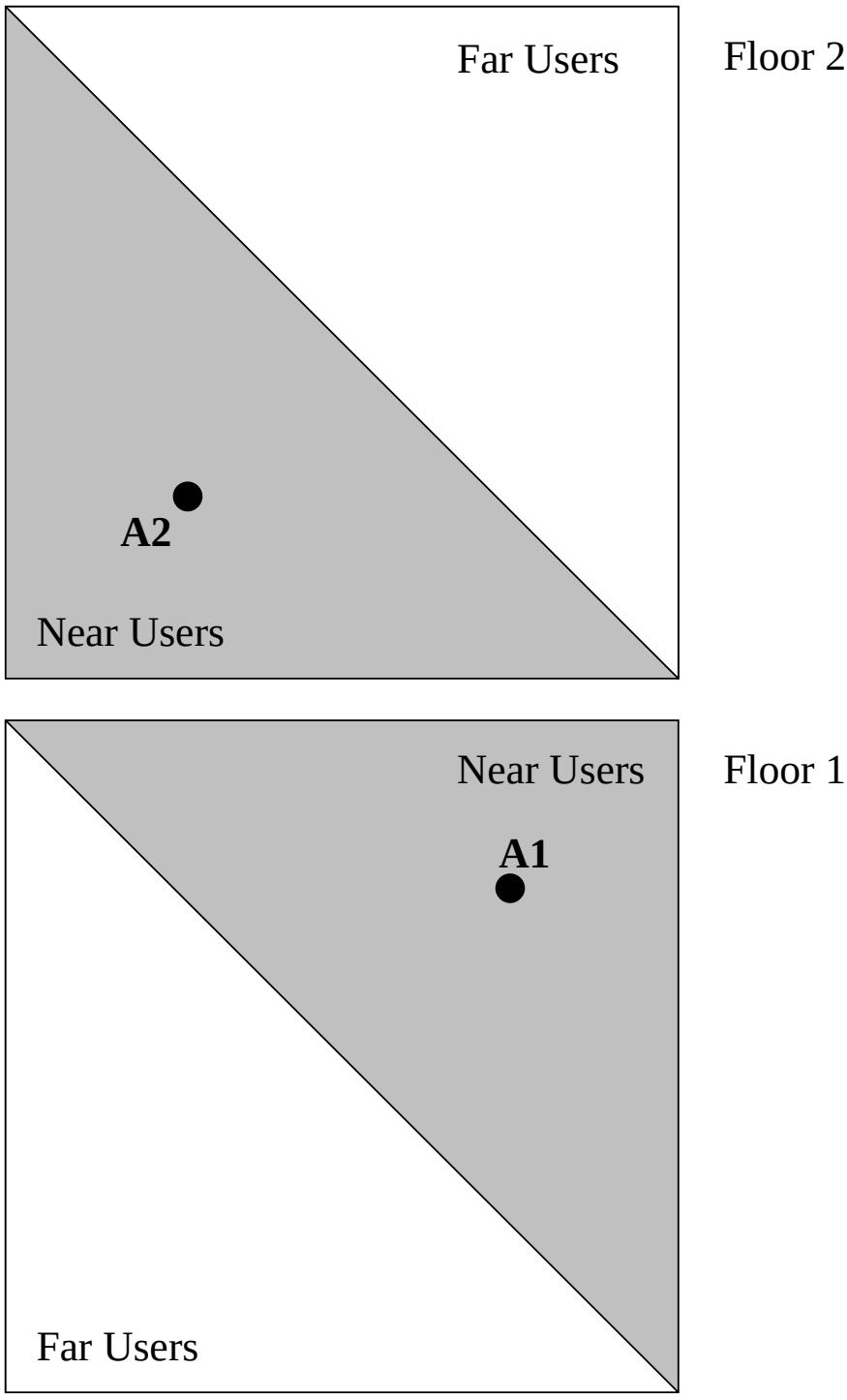

Figure 6.23: Distance sorting for the system shown in Fig. 6.21.

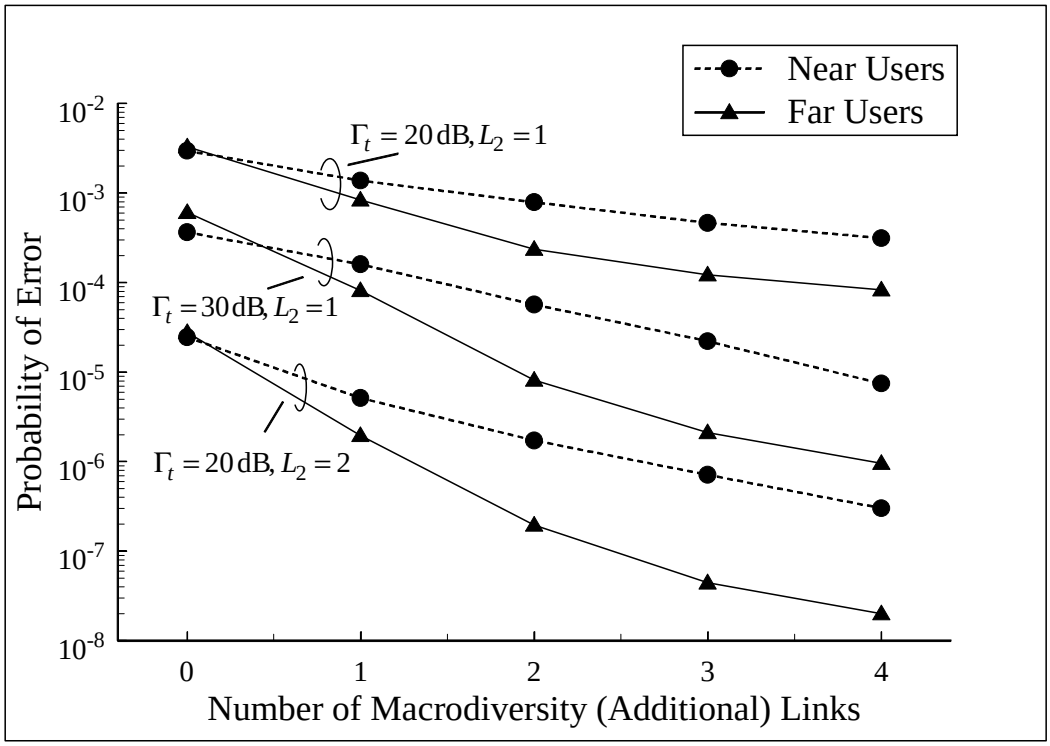

Figure 6.24: Performance of median users segregated by distance for the system shown in Fig. 6.21.

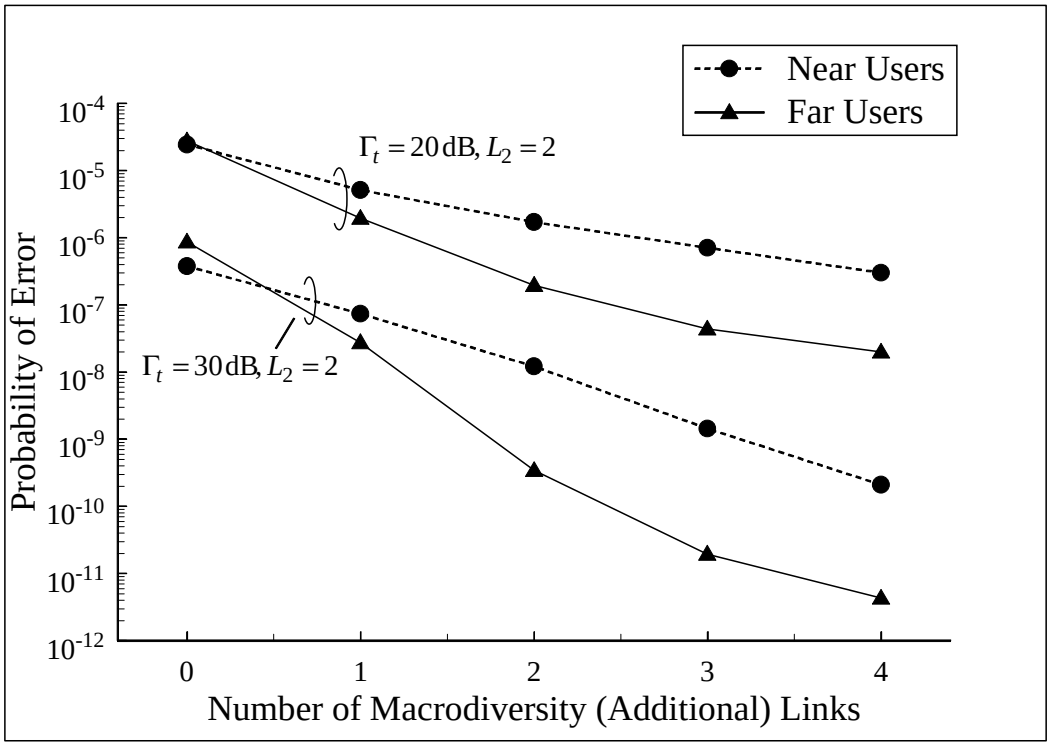

Figure 6.25: Performance of median users segregated by distance for the system shown in Fig. 6.21 operating with $L_2 = 2$.

and increasing Γ_t generally decreases the BER. However, this performance improvement is limited by the fact that the power control algorithm reduces Γ_t if any user is not able to achieve it. In contrast, the addition of microdiversity antennas to the ML-MUMD improves the BER performance without affecting the targeted Γ_t.

Even though the power control algorithm and the link selection technique both focus on the worst case users, all users respond favorably to the ML-MUMD. In an outdoor system, users can expect performance gains of approximately 2 - 3 orders of magnitude with the addition of macrodiversity links to the ML-MUMD. In an indoor system with one antenna array per floor in a two story building, users can expect about 2 - 6 orders of magnitude improvement in their BERs, and in a single story building with two antenna arrays, the gains typically range from about 3 - 6 orders of magnitude. Therefore, the combination of multiuser detection with macrodiversity reception has the capability to improve performance dramatically in both outdoor and indoor communications systems.

The results that are presented in this chapter focus on a limited situation of four users and two macrodiversity antenna arrays in both outdoor and indoor communications systems. It is difficult to generalize these results for increasing numbers of users and base stations. We would expect improved performance due to both diversity reception and interference reduction for base stations which are added to the first tier. However, the effect of adding additional users is still an open issue.

Each time a user is added to the MUMD at an antenna, the computational complexity of the ML-MUMD at that antenna increases exponentially. The computational complexity is kept to a minimum through the use of the CMM algorithm in Chapter 3. However, in practice a full maximum likelihood implementation is unlikely, and it may be more attractive to use approximate tree search algorithms such as the M or T algorithm as described in [71]. According to Moore's Law [72], with binary signalling and exponential growth, we can expect to add one user per cell every year and a half.

Chapter 7

Macrodiversity Applied to the Forward Link

As stated in Chapter 1, macrodiversity on the forward link is equivalent to generating artificial multipath. The artificial multipath is produced by offsetting the PN sequences between the base stations in a mobile's Active Set. In this way, the RAKE receiver at the mobile can isolate and combine these different transmissions as if they were natural multipath produced by the environment. The advantage of this artificial multipath is increased diversity, and the disadvantage is increased interference. Section 1.3.2 outlines previous work in the area of macrodiversity on the forward link. These studies suggest that the increased interference generally neutralizes the added diversity for unsectorized cells when all of the base stations in the Active Set transmit the same power to the mobile unit in soft handoff [21], [26], [27]. This chapter focuses on allowing the macrodiversity antenna transmit powers to differ, and optimizing them by minimizing the average of all users' BERs. The improvement of the optimization algorithm is quantified in terms of forward link capacity gains realized in an indoor DS-CDMA system.

Power allocation among the macrodiversity antennas is not straightforward. For example, as seen in Fig. 7.1, it may seem reasonable for two antennas (A1 and A2) to allocate equal powers to a mobile unit (U1) if the signals are received with equal strength. However, if A2 has a stronger link to another mobile unit (U2), it will be advantageous for A1 to allocate most of the power to U1 in order to reduce interference at U2. The proposed global optimization addresses this kind of situation by minimizing the sum of the individual

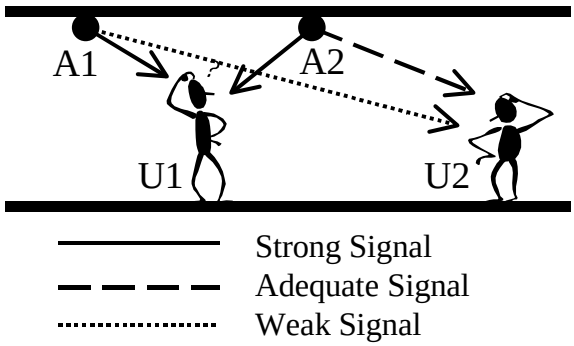

Figure 7.1: A typical indoor wireless propagation scenario.

mobile unit's estimated BERs. The BER at each mobile unit is estimated as a piecewise linear function that is based on the asymptotic behavior of coded diversity reception with unequal SNRs. The optimization is implemented as a steepest descent algorithm operating at the relatively slow shadowing rate.

The forward link performance of a DS-CDMA system will become increasingly important as third generation cellular systems incorporate different kinds of traffic. Services such as voice, image, and video will only be made possible if the network can transmit with a high data rate while achieving an acceptable quality of service. In order to address the issue of utilizing DS-CDMA with a different data rate and a different BER requirement than is normally used for voice communications, the proposed optimization algorithm's performance is compared to that for traditional soft handoff in a number of different situations. In all cases, the optimization algorithm outperforms traditional soft handoff power allocation and significantly increases the forward link capacity.

7.1 System Model

The signal received at mobile i is given as:

$$r_i(t) = \mathbf{c}_i^{\mathrm{T}} \left(\mathbf{S}_i \mathbf{b} + \mathbf{s}_{p_i}\right) + n_i(t) \tag{7.1}$$

where: $\mathbf{c}_i^{\mathrm{T}} = [c_{1i}, ..., c_{li}, ..., c_{Li}]$ is a vector of complex Gaussian channel gains from L macrodiversity antennas to the i^{th}mobile. $\mathbf{b} = [b_1, ..., b_k, ..., b_K]^{\mathrm{T}}$ is a vector of BPSK information bits destined for the K users. $n_i(t)$ is the additive white Gaussian noise (AWGN);

it is a complex Gaussian process with zero mean and a power spectral density of N_o. $\mathbf{s}_{p_i} = A_p \left[s_p(t-\tau_{1i}), ..., s_p(t-\tau_{Li})\right]^{\mathrm{T}}$ where A_p is the amplitude of the pilot signal transmitted from each antenna, and $\mathbf{S}_i$ is a matrix defined as follows:

$$\mathbf{S}_i = \begin{bmatrix} A_{11}s_1(t-\tau_{1i}) & ... & A_{1K}s_K(t-\tau_{1i}) \\ ... & ... & ... \\ A_{L1}s_1(t-\tau_{Li}) & ... & A_{LK}s_K(t-\tau_{Li}) \end{bmatrix}. \tag{7.2}$$

A_{li} is the amplitude of the signal transmitted from the l^{th} antenna to the i^{th} mobile, and τ_{li} is the delay incurred between the l^{th} antenna and the i^{th} mobile. $s_i(t)$ and $s_p(t)$ are the normalized unit-energy waveforms with support $[0, T]$ for user i and the pilot signal respectively. The vector of the normalized matched filter output for the i^{th} user from the l^{th} antenna, sampled at the symbol rate, $1/T$, is

$$\begin{aligned} y_{li} &= \int_{\tau_i}^{T+\tau_i} r_i(t) s_i^*(t-\tau_{li}) dt \\ &= \mathbf{c}_i^{\mathrm{T}} \left(\mathbf{R}_{li}\mathbf{b} + \mathbf{r}_{p_{li}}\right) + e_{li} \end{aligned} \tag{7.3}$$

where $e_{li} = \int_{\tau_i}^{T+\tau_i} s_i^*(t-\tau_{li}) \cdot n_i(t) dt$ is the noise at the matched filter output. $\mathbf{r}_{p_{li}} = \int_{\tau_i}^{T+\tau_i} s_i^*(t-\tau_{li}) \cdot \mathbf{s}_{p_i} dt$ contains the cross-correlations between an intended user's waveform and pilot signal waveforms. $\mathbf{R}_{li} = \int_{\tau_i}^{T+\tau_i} s_i^*(t-\tau_{li}) \cdot \mathbf{S}_i dt$ is the cross-correlation matrix with elements

$$R_{(n,l)(k,i)} = A_{nk} \int_{\tau_i}^{T+\tau_i} s_i^*(t-\tau_{li}) s_k(t-\tau_{ni}). \tag{7.4}$$

In (7.4), if $l \neq n$ and $i = k$, the same, but time shifted, signature waveform is sent to mobile i from two different antennas. If $l = n$ and $i \neq k$, two different signature waveforms intended for two different users are sent from the same antenna. In (7.3) the interfering signals result from correlations with the pilot sequences and from correlations with other user sequences when $l \neq n$ and/or $i \neq k$.

When using DS-CDMA, the information sequence is spread using a pseudo-random code. The interference between users is determined by the actual cross-correlations between the pseudonoise sequences. However, for simplicity, it is assumed that the interfering users are suppressed by the processing gain where $\sigma_s^2 = R/W$, and the following estimate can be

made:

$$\frac{1}{2}E\left[y_{li}^{*}y_{li}\right] \cong \sigma_{c,li}^{2}p_{li} + \sigma_{s}^{2}\left[\sum_{n=1}^{L}\sigma_{c,ni}^{2}\cdot \left(\sum_{k=1}^{K}p_{nk} + p_{p}\right) - \sigma_{c,li}^{2}p_{li}\right] + N_{o} \tag{7.5}$$

where $p_{li} = A_{li}^{2}$ and $p_{p} = A_{p}^{2}$. The energy of the signal in (7.5) is given by $\sigma_{c,li}^{2}p_{li}$, and the rest is the energy of the interference and noise. Therefore, the SINR can be given as

$$\Gamma_{li} = \left[\sigma_{s}^{2}\left(\frac{X_{i}}{x_{lii}} - 1\right)\right]^{-1} \tag{7.6}$$

where:

$$x_{nki} = \sigma_{s}^{2}\sigma_{c,ni}^{2}p_{nk} \tag{7.7}$$

$$X_{i} = \sum_{n=1}^{L}\sum_{k=1}^{K}x_{nki} + \sigma_{s}^{2}p_{p}\sum_{n=1}^{L}\sigma_{c,ni}^{2} + N_{o}. \tag{7.8}$$

In [15] it is shown that the error probability of diversity reception with unequal SNRs can be estimated in the asymptotic region as the branch SNRs become increasingly large. The expression in [15] is modified here to include the effects of the convolutional code used on the forward link of the DS-CDMA system. The theoretical performance of the convolutional code was calculated with a union bound using a similar approach to that proposed in [61] and [63], and the resulting characteristic function was inverted using the new technique presented in Appendix A. The effects of the convolutional code can be included in the error probability estimates for mobile, i, as follows:

$$P_{ei} = \alpha_{i}\prod_{l\in\mathcal{A}_{i}}M\left(\Gamma_{li}\right)\cdot\Gamma_{li}^{-D(\Gamma_{li})} \tag{7.9}$$

where $\mathcal{A}_{i}$ represents user i's Active Set which is composed of L_{i} macrodiversity antennas. $\alpha_{i} = \binom{2L_{i}D_{\infty}-1}{L_{i}D_{\infty}}\left(2\left(1-\rho\right)\right)^{-L_{i}D_{\infty}}$ is a multiplicative factor similar to that found in [15] where $\rho = -1$ for BPSK signals. In order to account for the fact that the system operates in the non-asymptotic region at low SINRs, $M\left(\Gamma_{li}\right)$ and $D\left(\Gamma_{li}\right)$ are both functions of the SINR, and they are determined by performing a piecewise linear curve fit to the theoretical P_{ei}. $M\left(\Gamma_{li}\right)$ is a multiplicative factor, and $D\left(\Gamma_{li}\right)$ is the derivative of $\log(P_{ei})$ with respect to

Γ_{li} in dB. In other words, $D(\Gamma_{li})$ is an equivalent order of diversity. $D_\infty = D(\Gamma_{li})|_{\Gamma_{li}\to\infty}$ is the equivalent order of diversity in the asymptotic region of the BER curve. In this study, perfect interleaving by bit is assumed; therefore, D_∞ is equal to the minimum free distance of the convolutional code. The error probability estimate given in (7.9) can be used in both the traditional soft handoff and optimization algorithms discussed in the following sections.

7.2 Traditional Soft Handoff

Once the Active Set for each user has been determined, each traffic channel is assigned a small and equal portion of the total traffic power. If the probability of error for mobile i, P_{ei}, is greater than a specified threshold, the powers allocated at each antenna for this user are increased by 1 dB. In contrast, if P_{ei} is less than the threshold, the powers transmitted to this mobile station are decremented by 1 dB. If the powers begin to oscillate around the threshold, a "do nothing" command can be sent to keep the powers at a constant level.

If the error probabilities for all mobiles are below the specified threshold, and the total transmitted power at each antenna is within the preset power limit, the soft handoff power allocation has successfully serviced all mobile units. However, if this requirement cannot be met, the forward link powers of the macrodiversity antennas are optimized with the algorithm discussed in the next section.

7.3 Forward Link Power Optimization

In order to achieve a global optimization, the sum of the error probabilities for the individual mobiles is minimized. The objective function to be minimized is

$$P_e = \sum_{i=1}^{K} P_{ei}. \tag{7.10}$$

The optimization is implemented as a steepest descent algorithm. Therefore, the algorithm requires the following partial derivative:

$$\frac{\partial P_e}{\partial p_{nk}} = \sum_{i=1}^{K} \frac{\partial P_{ei}}{\partial p_{nk}} \quad \forall n \& k \tag{7.11}$$

and it can be shown that

$$\left.\frac{\partial P_{ei}}{\partial p_{nk}}\right|_{k\neq i} = \sigma_s^2 \sigma_{c,ni}^2 P_{ei} \sum_{j\in\mathcal{A}_i} \frac{D(\Gamma_{ji})}{X_i - x_{jii}} \tag{7.12}$$

$$\left.\frac{\partial P_{ei}}{\partial p_{nk}}\right|_{k=i} = \sigma_s^2 \sigma_{c,ni}^2 P_{ei} \cdot \left\{ \sum_{j \in \mathcal{A}_i, j \neq n} \frac{D(\Gamma_{ji})}{X_i - x_{jii}} - \frac{D(\Gamma_{ni})}{x_{nii}} \right\}. \quad (7.13)$$

A global optimization strategy is presented that allocates power at the various macrodiversity antennas so that the added diversity outweighs the increased interference and the average of all users' BERs is minimized. The complexity of this global optimization is reduced as can be seen in (7.12) and (7.13) since the summations are only performed over the antennas in each user's Active Set.

By moving in the direction opposite to the gradient, the global minimum is approached. When the algorithm is operating in the asymptotic region of the BER curve, i.e. when $D(\Gamma_{mi}) = D_\infty, \forall m \in \mathcal{A}_i$, it can be proven that this objective function possesses only the one global minimum since the second derivative is always greater than zero. Even though this has not been proven for the non-asymptotic region, the second derivative has never been observed to go below zero in practice.

The power at each antenna is constrained as follows: $\sum_{k=1}^{K} p_{nk} = C$. This is actually a plane in hyperspace. Therefore, if the optimization attempts to exceed the power limit on any antenna, the result is simply projected onto the hyperplane ensuring that the antennas never exceed their power limit.

Minimizing the objective function, $P_e = \sum_{i=1}^{K} P_{ei}$, brings the individual error probabilities closer together. However, it does not eliminate the separation entirely. Therefore, once the sum has been minimized, the optimization algorithm enters a second stage which focuses on equating the individual error probabilities in an attempt to reduce the maximum probability of error, $P_{e\max}$. In the second stage of optimization, if $P_{ei} > P_e/K$, the partial derivative, $\partial P_{ei}/\partial p_{ni}$, is used in the steepest descent algorithm to minimize P_{ei}. In contrast, if $P_{ei} \leq P_e/K$, the partial derivative, $\partial P_{e\max}/\partial p_{ni}$, is used in the steepest descent algorithm to minimize $P_{e\max}$. In this way, the mobile units with high BERs receive more power, while those with low BERs give up a portion of their power. The two stages of optimization can be seen in Fig. 7.2. These results are depicted for 57 users located on 2 floors of a building. The users are serviced by a total of 4 antennas with 2 antennas per floor.

As can be seen from this figure, the first stage of optimization (iterations 1-300) focuses on minimizing the average probability of error, and the second stage of optimization (iterations 300-400) focuses on equating the error probabilities in an attempt to reduce $P_{e\max}$.

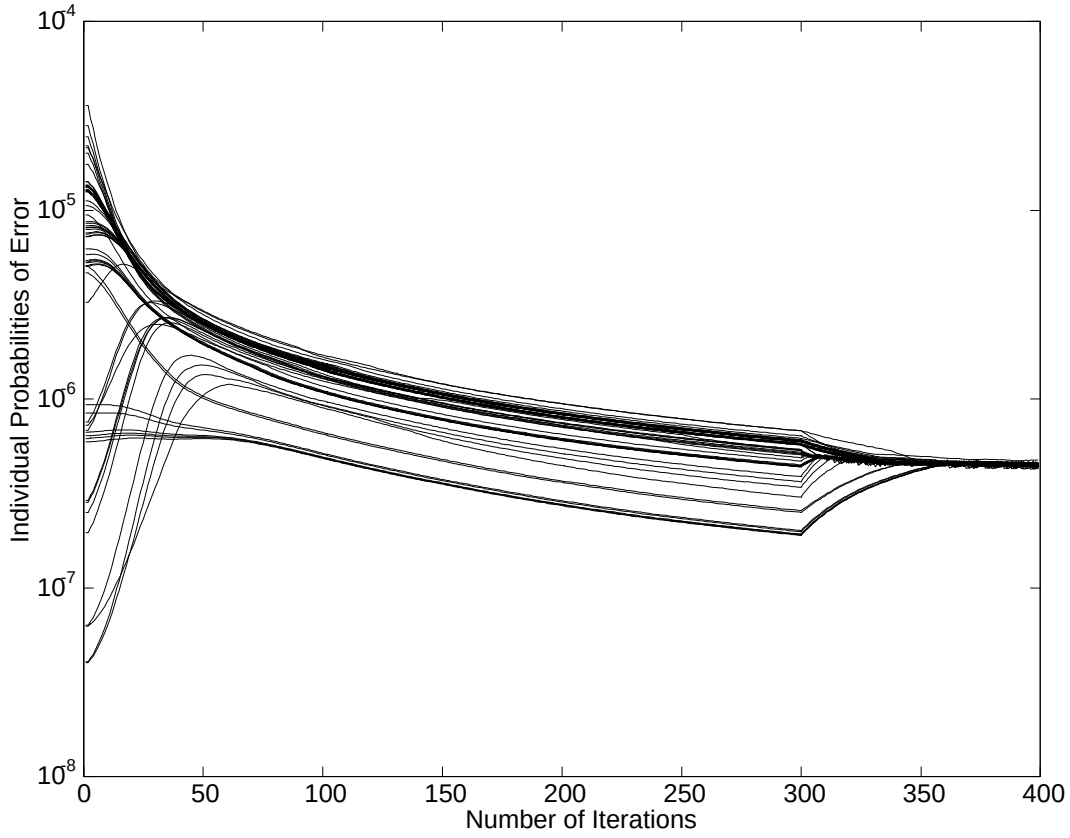

Figure 7.2: The 2 stages of optimization.

Both stages of the optimization are necessary for reducing the maximum BER. The result of eliminating the second stage of optimization is obvious from observing Fig. 7.2. However, eliminating the first stage of optimization causes the individual error probabilities to be simply equated, most often at a higher BER than desired. This optimization routine will now be compared with a typical soft handoff algorithm in the following section.

7.4 Simulations

The simulated system consists of 2 floors in a building with 2 antennas per floor. Each antenna allocates 80% of its power to traffic and 20% of its power to the pilot signal. In the simulations, $N_o = 0$ in order to investigate the interference limited case. The transmitted signals are assumed to undergo path loss, lognormal shadowing, and Rayleigh fading. The parameters for the indoor propagation model are similar to those used in Section 6.3.

The mobiles are initially added to either floor of the building in a random fashion. Each time a mobile is added, its active set is determined by comparing $(E_c/I_o)_{li}$ to a threshold of -14 dB. The E_c in $(E_c/I_o)_{li}$ represents the pilot signal energy received from antenna l, and the I_o represents the total interference and noise measured at mobile i. The simulations begin by performing a traditional soft handoff power allocation for all users each time an additional user is added to a floor. When a single user on either floor cannot be serviced, additional users are added only to the other floor. Once both floors contain a mobile that cannot be serviced by traditional soft handoff power allocation, the optimization algorithm takes over. If the optimization algorithm can service all of the above users, mobiles are added in a similar fashion to that described above.

The simulation results can be seen in Figs. 7.3 and 7.4. These figures depict forward link capacities achieved at different BER requirements for both soft handoff power allocation and optimization of forward link transmit powers. Figs. 7.3 and 7.4 contain forward link capacity estimates for a CDMA system with processing gains of $W/R = 128$ and $W/R = 32$ respectively, and each data point represents an average over 100 independent trials.

As can be seen from these figures, the optimization algorithm consistently outperforms traditional soft handoff power allocation, and the capacity gains typically range between 10-20%. In most cases, use of the optimization algorithm does not affect the capacity estimate's variance. However, in a couple of cases, the optimization algorithm not only outperforms soft handoff, but it also reduces the variance of the capacity estimate, thus making the

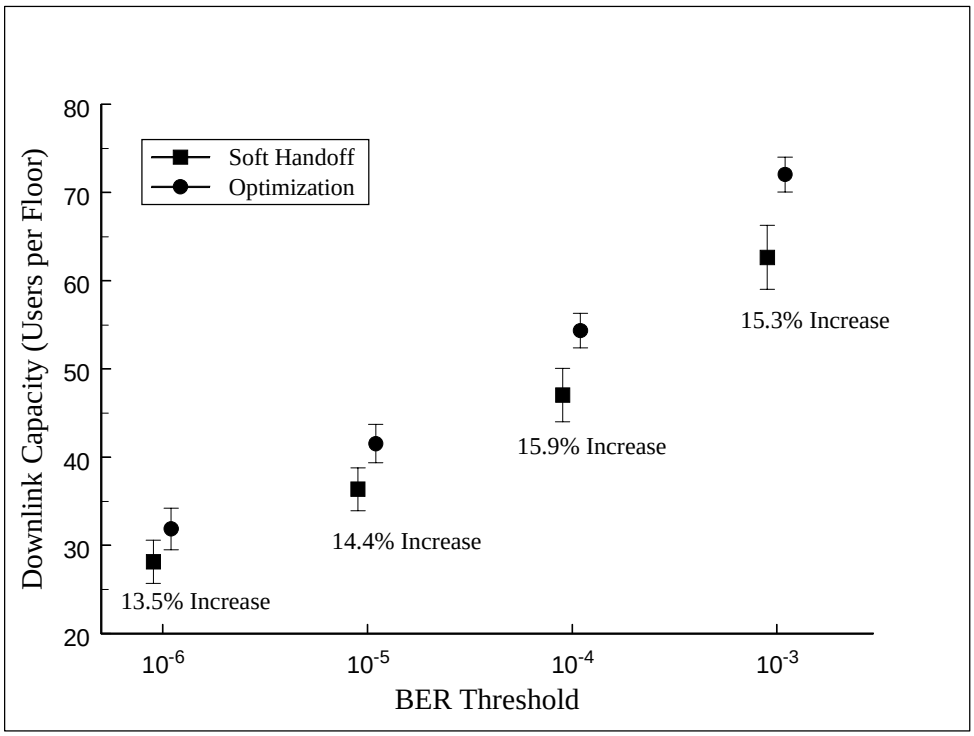

Figure 7.3: Soft handoff and optimization capacities for W/R = 128.

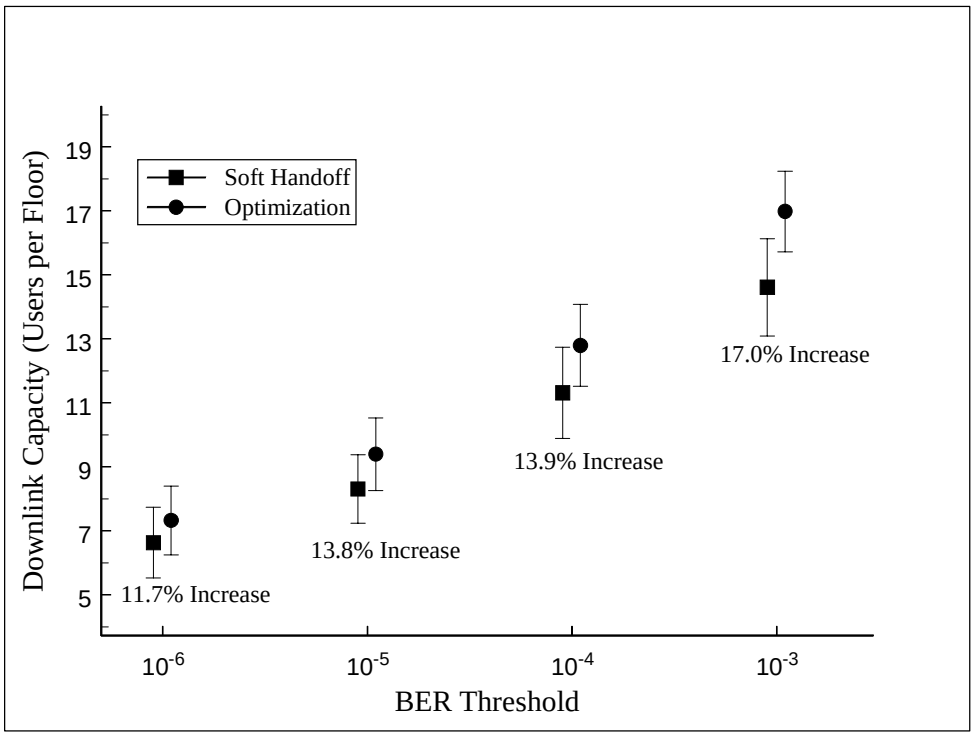

Figure 7.4: Soft handoff and optimization capacities for W/R = 32.

estimate more reliable.

Experiments were also performed which investigated the effect of increased accuracy in the soft handoff power allocation; this accurate allocation involves adjusting the powers transmitted to a mobile by 0.5 dB instead of 1 dB. The simulation results show that the optimization algorithm still outperforms the accurate soft handoff allocation with forward link capacity gains on the order of 10-13%. Therefore, simply decreasing the step size of the soft handoff algorithm can not provide the gains achievable with optimization since soft handoff does not address the issue of allocating different transmit powers among the macrodiversity antennas in a mobile's Active Set.

To conclude, the simulation results show that significant capacity gains can be realized by optimizing the forward link transmit powers of macrodiversity antennas. The forward link capacity gains typically range between 10-20% when compared to traditional soft handoff. Therefore, this study has shown that forward link transmit power optimization in an indoor DS-CDMA system is successful in improving system performance.

Chapter 8

Conclusions

This thesis has focused on the use of macrodiversity in a DS-CDMA system and has shown that the use of macrodiversity has the capability to improve both the forward link and the reverse link of a wireless communications system.

The primary investigation of this thesis focuses on the reverse link where macrodiversity reception is combined with the maximum likelihood (ML) multiuser detector. The resulting ML multiuser-macrodiversity detection (MUMD) is performed at the system controller once each base station has forwarded its signals to this central location.

This thesis is the first to derive the ML multiuser-macrodiversity detector taking into consideration that the multiuser detection at each macrodiversity antenna includes different and often overlapping sets of users. The general structure for the ML multiuser-macrodiversity detector includes interference from past, current, and future data symbols. However, further manipulation reveals that the ML-MUMD metric can be written so that it is composed of sums of terms that depend on only a select few of the past and current data symbols at a time. The resulting metric structure makes the ML multiuser macrodiversity detector well suited for a dynamic programming approach which keeps its computational complexity at a minimum.

The Conditional Metric Merge (CMM) algorithm presented in the thesis is the realization of this dynamic programming approach. The CMM algorithm reduces the computational complexity of the ML multiuser-macrodiversity detector by an enormous factor. It is a spatial extension of the well known Viterbi algorithm. In fact, if all of the users' signals arrived at each macrodiversity antenna with similar relative delays, and the signals were detected by all of the macrodiversity antennas, the CMM algorithm would reduce to the

Viterbi algorithm. However, as this is not typical in practice, the CMM algorithm applies dynamic programming in both space and time.

The performance of the ML multiuser macrodiversity detector is investigated analytically. It is the first analytical treatment of the ML multiuser-macrodiversity detector in Rayleigh fading channels, and it also includes the effects of frequency selective fading, imperfect synchronization, and imperfect channel state information (CSI).

The CSI is obtained through a new MMSE multiuser channel estimation technique which is a CDMA extension of the work in [59]. This channel estimation technique has the ability to track the complex gains of channels subject to frequency selective fading and imperfect code synchronization.

In the analytical treatment of the ML multiuser-macrodiversity detector, each user's BER is upper bounded by applying the union bound to the appropriate pairwise error event probabilities. The results show that this theoretical upper bound corresponds well with error probabilities obtained through simulation.

The performance of the ML multiuser-macrodiversity detector is investigated in both outdoor and indoor wireless communications system. The results show that the addition of just one macrodiversity link has the capability to reduce the BER for many different users. In this thesis, the link selection technique and the power control algorithm both focus on the worst case user, i.e. the user with the highest BER. Even so, the results show that all users benefit from the addition of macrodiversity links to the ML-MUMD. In a typical outdoor system, users can expect between 2 - 3 orders of magnitude improvement in their BERs.

Gains of approximately 2 - 6 orders of magnitude are reported for two different two story indoor systems with one antenna array per floor. By observing distance dependent results, it appears that vertically aligning the antennas between the floors of the building is preferable to offsetting the antennas. Vertically aligned antennas are less distance dependent and thus allow the ML-MUMD system to provide a similar level of performance for all users, regardless of their placement within the building. In a single story system with two antenna arrays placed along the main diagonal of the floor, the gains from ML-MUMD typically range from about 3 - 6 orders of magnitude.

To conclude, the reverse link performance of a wireless DS-CDMA system can be significantly improved through the combination of multiuser detection with macrodiversity reception. The computational load for the ML multiuser-macrodiversity detector is certainly an issue. However, the CMM algorithm organizes the computation in such a way

that the exponent of exponential growth is kept to a minimum. In any case, our results establish bounds and goals for suboptimal multiuser-macrodiversity detection methods.

The thesis also presents a new computational tool for use in general fading channel analyses. Like many published investigations, Chapter 5 required the inversion of a characteristic function having the form of an exponential and several poles. Although the theory of such inversions is classical, it is of little practical use in the case of mixed simple and multiple poles. The solution in Appendix A is numerically stable, eliminates singularities and circumvents the need for differentiation.

The secondary investigation of this thesis focuses on the forward link where the transmit power of macrodiversity antennas is optimized in an indoor DS-CDMA system. A global optimization strategy is presented which minimizes the average of all users' BERs. The weaker links can be removed from the global optimization, thus reducing its complexity. The results show that the forward link capacity is increased by approximately 10 - 20 % when compared to traditional soft handoff.

In conclusion, macrodiversity reception and multiuser detection are indeed high performance tools which can be used to improve the performance of a wireless DS-CDMA system.

Appendix A

Inverting Mixed Characteristic Functions

In wireless communication systems with Rayleigh fading channels, a detection scheme can often be expressed as a comparison of a decision variable with a threshold, where the decision variable is a quadratic form in zero-mean complex Gaussian random variables. Since the system performance measure is the probability that the decision variable is less than the threshold, it implicitly makes use of the cumulative distribution function (cdf) of the decision variable. However, in most cases it is easier to formulate the characteristic function, which is the two-sided Laplace transform of the probability density function (pdf). This characteristic function can be inverted by residues or partial fraction expansion to determine the detector's performance. However, previously there has been no simple way of inverting a characteristic function which consists of both multiple and simple poles. In general, differentiation is required to invert a characteristic function with multiple poles. However, if the multiplicity is high, differentiation by hand becomes too cumbersome, and it has been more desirable to use a mechanical procedure such as a numerical integral. Unfortunately, such integrals have poor numerical stability.

This appendix proposes a simple numerical algorithm which is capable of inverting a characteristic function consisting of both multiple and simple poles. The approach benefits from the inherent symmetry in the residue calculations and uses the well known Vandermonde matrix in order to take advantage of this symmetry. It provides an exact solution for many error probability calculations.

A.1 Introduction

When calculating an error rate or the probability of flagging an erasure in fading channels [73], most thresholding schemes can be reduced to the evaluation of a quadratic form in Gaussian variates. For the special case of Rayleigh fading, the complex Gaussian variates are zero-mean, and the characteristic function of the thresholded variable, f, is given by (A.1) [67].

$$\phi_f(s) = \frac{A}{\prod_{k=0}^{N_L}(s - p_{l_k}) \prod_{m=0}^{N_R}(s - p_{r_m})} \tag{A.1}$$

where $A = \prod_{k=0}^{N_L} p_{l_k} \prod_{m=0}^{N_R} p_{r_m}$, p_{l_k} are the N_L left plane (LP) poles, p_{r_m} are the N_R right plane (RP) poles, and the poles are not necessarily distinct.

In order to calculate the probability of error or the probability of flagging an erasure, we need to take the inverse Laplace transform, (ILT), of $\phi_f(s)/s$, as shown in (A.2), to obtain the cumulative probability density function (pdf) of the random variable, f.

$$P(f < \psi) = \frac{1}{2\pi j} \int_{\sigma - j\infty}^{\sigma + j\infty} \frac{\phi_f(s)}{s} e^{s\psi} ds. \tag{A.2}$$

In (A.2), σ is placed within the region of convergence. Through the use of Cauchy's residue theorem [66], the ILT can be also be determined by calculating the residues at the RP or LP poles as shown in (A.3) [61].

$$P(f < \psi) = \begin{cases} -\sum \text{Residue}\left[e^{s\psi}\phi_f(s)/s\right]_{RPpoles}, \psi \leq 0 \\ +\sum \text{Residue}\left[e^{s\psi}\phi_f(s)/s\right]_{LPpoles}, \psi > 0 \end{cases}. \tag{A.3}$$

It is fairly simple to invert the characteristic function by residues if $\phi_f(s)$ consists of simple poles only. If $\phi_f(s)$ consists of multiple poles in the form, $\phi_f(s) = [p_{l_0} p_{r_0} / ((s - p_{l_0}) \cdot (s - p_{r_0}))]^N$, the ILT can be reduced to a formula which is found in [15, App. 4B]. However, if $\phi_f(s)$ involves both simple and multiple poles, the ILT of $\phi_f(s)/s$ becomes more complex as differentiation is required in order to calculate the residues.

As detection schemes become increasingly complex, the likelihood of $\phi_f(s)$ consisting of both multiple and simple poles also increases. For example, analytical approaches to the performance evaluation of trellis-coded modulation with set partitioning [61], multi-beam antenna arrays [74], and macrodiversity systems all lead to complicated characteristic

functions. Previously, the inversion of these characteristic functions has relied on methods such as numerical integration.

The authors of [75] have investigated the situation where a Laplace transfer function consists of both multiple and simple poles. They have used the generalized inverse Vandermonde matrix in order to invert the Laplace transfer function of a time-invariant system. Their solution is well suited to a system which can be activated by a number of different initial conditions. However, our situation is different from that in [75] in two ways. First, we are dealing with the two-sided Laplace transform as opposed to the one-sided Laplace transform, and second, the poles of our transfer function change with the fading channel statistics. Since differences in the fading channel statistics change the pole locations, we need a simple method for handling the situation where the pole multiplicity can change with the operating conditions.

This appendix presents a simple method for using residues to invert a characteristic function which is composed of both simple and multiple poles. The residue calculation method is based on partial fraction expansion when the characteristic function, $\phi_f(s)$, involves simple poles only. However, symmetry in the residues allows us to use the properties of the Vandermonde matrix to provide explicit cancellation of factors in the numerator and denominator, thereby avoiding the singularities that plague conventional inversion.

A.2 Residue Calculation Method

The ILT of $\phi_f(s)/s$ is calculated in (A.2) and (A.3). Rather than keeping the additional pole at zero separate, $\phi_f(s)$ is modified so that this additional pole is included into the LP poles such that $p_{l_{N_L+1}} = 0$. In order to describe the residue calculation method, it is assumed that $\psi \leq 0$ in (A.3), and the residues will be taken over the RP poles. The modification for the $\psi > 0$ case is straightforward.

Since it is assumed that $\psi \leq 0$, the RP poles are represented as $p_{r_m} = p_r + \delta_m$ and $0 \leq \delta_0 \leq \delta_1 \leq ... \leq \delta_{N_R}$. Note that if $\psi > 0$, the LP poles would be represented as $p_{l_k} = p_l - \delta_k$ and $0 \leq \delta_0 \leq \delta_1 \leq ... \leq \delta_{N_L+1}$. The residues at the RP poles are given by

$$R_n = \frac{Ae^{(p_r+\delta_n)\psi}}{\prod_{k=0}^{N_L+1}(p_r - p_{l_k} + \delta_n)\prod_{\substack{m=0 \\ m\neq n}}^{N_R}(\delta_n - \delta_m)}. \tag{A.4}$$

If the RP poles are distinct, then (A.4) presents no problems. However, if the RP poles

come closer together to become multiple poles, $(\delta_n - \delta_m)$ in (A.4) approaches zero, and some residues will contain singularities. However, we are interested in the sum of the residues, which as shown below, leads to cancellation of all factors of the form $(\delta_n - \delta_m)$, thus eliminating the singularities.

In order to eliminate the terms in the denominator, each residue is multiplied by a common factor, $C = GD$, where

$$G = \prod_{m=0}^{N_R} \prod_{k=0}^{N_L+1} (p_{r_m} - p_{l_k}) \tag{A.5}$$

and

$$D = \prod_{i=0}^{N_R} \prod_{j=i+1}^{N_R} (\delta_j - \delta_i)\,. \tag{A.6}$$

The modified residues are $C_n = R_n C$ and are given by

$$C_n = A e^{p_r \psi} \left(-1^{N_R - n} B_n D_n\right) \tag{A.7}$$

where:

$$B_n = e^{\delta_n \psi} \prod_{\substack{m=0 \\ m \neq n}}^{N_R} \prod_{k=0}^{N_L+1} (p_r - p_{l_k} + \delta_m) \tag{A.8}$$

and

$$D_n = \prod_{\substack{i=0 \\ i \neq n}}^{N_R} \prod_{j=i+d}^{N_R} (\delta_j - \delta_i)\,. \tag{A.9}$$

In (A.9), $d = \begin{cases} 1 \text{ if } i \neq n-1 \\ 2 \text{ if } i = n-1 \end{cases}$. The cdf of f is now given by

$$P\left(f < \psi\right) = \frac{-A e^{p_r \psi}}{C} \sum_{n=0}^{N_R} -1^{N_R - n} B_n D_n. \tag{A.10}$$

It can be shown that D_n is the determinant of a Vandermonde matrix as shown in (A.11)

[76].

$$D_n = \begin{vmatrix} 1 & ... & 1 & 1 & ... & 1 \\ \delta_0 & ... & \delta_{n-1} & \delta_{n+1} & ... & \delta_{N_R} \\ \delta_0^2 & ... & \delta_{n-1}^2 & \delta_{n+1}^2 & ... & \delta_{N_R}^2 \\ ... & ... & ... & ... & ... & ... \\ \delta_0^{N_R-1} & ... & \delta_{n-1}^{N_R-1} & \delta_{n+1}^{N_R-1} & ... & \delta_{N_R}^{N_R-1} \end{vmatrix} \tag{A.11}$$

Therefore, from (A.10) and (A.11), it can be observed that the formulation of $P(f < \psi)$ is equivalent to evaluating the determinant of a matrix through the expansion of minors. In (A.10) D_n is the minor associated with B_n, and the cumulative pdf of f is found in (A.12).

$$P(f < \psi) = \frac{-Ae^{p_r\psi}\det(\mathbf{X})}{C} \tag{A.12}$$

where

$$\mathbf{X} = \begin{bmatrix} 1 & 1 & ... & 1 \\ \delta_0 & \delta_1 & ... & \delta_{N_R} \\ \delta_0^2 & \delta_1^2 & ... & \delta_{N_R}^2 \\ ... & ... & ... & ... \\ \delta_0^{N_R-1} & \delta_1^{N_R-1} & ... & \delta_{N_R}^{N_R-1} \\ B_0 & B_1 & ... & B_{N_R} \end{bmatrix} \tag{A.13}$$

At this point, $C = GD$ is in the divisor of (A.12). The division will cause numerical problems when $\delta_j - \delta_i \cong 0$. Therefore, we would like to factor D out of the determinant so that cancellation occurs. That is, we wish to represent the determinant of $\mathbf{X}$ as $\det(\mathbf{X}) = D\det(\mathbf{H})$ so that

$$P(f < \psi) = \frac{-Ae^{p_r\psi}\det(\mathbf{H})}{G} \tag{A.14}$$

where $\mathbf{H} = [\mathbf{h}_0, \mathbf{h}_1, ..., \mathbf{h}_{N_R}]$. We show below that $\mathbf{H}$ can be calculated in an iterative fashion by exploiting the following properties of determinants: Property #1: To any column of the matrix we can add any multiple of any other column without changing the determinant. Property #2: A common factor of all the elements in a row or a column can be taken outside the determinant.

The procedure to be described may appear to require symbolic manipulations. However, Section A.3 demonstrates that it can be implemented in a purely numerical fashion.

In order to factor D from $\mathbf{X}$ to obtain $\mathbf{H}$, we first set $\mathbf{H}^{(0)} = \mathbf{X}$, where the superscript in brackets on $\mathbf{H}$ refers to the iteration. In the first iteration of this algorithm, $\mathbf{h}_0^{(0)}$ is subtracted from all other columns using property #1. After this subtraction, $\delta_j - \delta_0$ can be factored out of all elements in column j giving $\mathbf{h}_j^{(0)} - \mathbf{h}_0^{(0)} = (\delta_j - \delta_0)\,\mathbf{q}_j^{(0)}$ for $1 \leq j \leq N_R$, where $\mathbf{q}_j^{(0)}$ is the resulting vector after factorization, and proof of divisibility is given below. Then using property #2, $\delta_j - \delta_0$ can be taken outside the determinant. Thus, the columns in $\mathbf{H}^{(1)}$ are now $\mathbf{h}_j^{(1)} = \mathbf{q}_j^{(0)}$ for $1 \leq j \leq N_R$, and the first column is left unchanged, i.e. $\mathbf{h}_0^{(1)} = \mathbf{h}_0^{(0)}$. In the second iteration of this algorithm, $\mathbf{h}_1^{(1)}$ is subtracted from $\mathbf{h}_2^{(1)} ... \mathbf{h}_{N_R}^{(1)}$, and $\delta_j - \delta_1$ is factored from the appropriate terms giving $\mathbf{h}_j^{(1)} - \mathbf{h}_1^{(1)} = (\delta_j - \delta_1)\,\mathbf{q}_j^{(1)}$. Once $\delta_j - \delta_1$ is taken outside the determinant, $\mathbf{h}_j^{(2)} = \mathbf{q}_j^{(1)}$ for $2 \leq j \leq N_R$. This procedure is repeated until $\mathbf{h}_{N_R-1}^{(N_R-1)}$ is subtracted from $\mathbf{h}_{N_R}^{(N_R-1)}$, and $\delta_{N_R} - \delta_{N_R-1}$ is taken outside the determinant leaving $\mathbf{h}_{N_R}^{(N_R)} = \mathbf{q}_{N_R}^{(N_R-1)}$. This procedure results in factoring D out of the determinant so that $\mathbf{H} = \mathbf{H}^{(N_R)}$, and $\det(\mathbf{X}) = D \det(\mathbf{H})$ as desired.

It can be shown that the resulting $\mathbf{H}^{(N_R)}$ is a lower triangular matrix. Therefore $\det(\mathbf{H}^{(N_R)})$ is simply the product of the diagonal elements, and $h_{N_R N_R}^{(N_R)}$ is the only diagonal element that is not equal to 1. Therefore, $\det(\mathbf{H}^{(N_R)}) = h_{N_R N_R}^{(N_R)}$, where $h_{N_R N_R}^{(N_R)}$ is the element in row N_R+1 and column N_R+1 of $\mathbf{H}^{(N_R)}$. Since we are only interested in $h_{N_R N_R}^{(N_R)}$, the above procedure can be performed on the last row of $\mathbf{X}$ only. It is important to note that as $h_{N_R N_R}^{(N_R)}$ is calculated, numerical values are used for ψ, p_r, and p_{l_k} where $0 \leq k \leq N_L$. Initially variables are used to represent the δ_m in $\mathbf{H}^{(0)}$ where $0 \leq m \leq N_R$. However, once $h_{N_R j}^{(i)}$ is substituted with $h_{N_R j}^{(i+1)} = q_{N_R j}^{(i)}$, δ_i can be replaced with its numerical value as it is no longer needed in symbolic form.

Now that the general procedure for obtaining $h_{N_R N_R}^{(N_R)}$ has been discussed, the method for factoring $\delta_j - \delta_i$ from $h_{N_R j}^{(i)} - h_{N_R i}^{(i)}$ to give $h_{N_R j}^{(i)} - h_{N_R i}^{(i)} = (\delta_j - \delta_i)\, q_{N_R j}^{(i)}$ will be described. It can be shown that

$$\delta_j^n \delta_i^m - \delta_i^n \delta_j^m = \begin{cases} (\delta_j - \delta_i)\left(\delta_i^m \delta_j^{n-1} + \delta_i^{m+1}\delta_j^{n-2} + \cdots \delta_i^{n-1}\delta_j^m\right), & \forall n > m \\ -(\delta_j - \delta_i)\left(\delta_i^n \delta_j^{m-1} + \delta_i^{n+1}\delta_j^{m-2} + \cdots \delta_i^{m-1}\delta_j^n\right), & \forall n < m \\ 0, \quad n = m \end{cases} \tag{A.15}$$

Therefore, if $P_1(y)$ denotes a polynomial in y and $P_2(y)$ denotes a different polynomial in

y it can be observed from (A.15) that $\delta_j - \delta_i$ can always be factored from an equation of the form $P_1(\delta_i) P_2(\delta_j) - P_1(\delta_j) P_2(\delta_i)$ to give $(\delta_j - \delta_i) P_{12}(\delta_i, \delta_j)$, where $P_{12}(\delta_i, \delta_j)$ is the resulting polynomial after factorization.

In the first iteration of the procedure for determining $h^{(N_R)}_{N_R N_R}$, $\delta_j - \delta_0$ needs to be factored from $h^{(0)}_{N_R j} - h^{(0)}_{N_R 0}$ for $1 \leq j \leq N_R$.

$$h^{(0)}_{N_R j} - h^{(0)}_{N_R 0} = B_j - B_0 = \prod_{\substack{m=1 \\ m \neq j}}^{N_R} \prod_{k=0}^{N_L+1} (p_r - p_{l_k} + \delta_m) \left\{ P_1(\delta_0) P_2^{(0)}(\delta_j) - P_1(\delta_j) P_2^{(0)}(\delta_0) \right\}. \tag{A.16}$$

In (A.16), $P_1(\delta) = \prod_{k=0}^{N_L+1} (p_r - p_{l_k} + \delta) = \sum_{w=0}^{N_L+1} a_w \delta^w$ where a_w is determined by expanding the polynomial, and $P_2^{(0)}(\delta_j) = e^{\delta_j \psi} = \sum_{w=0}^{\infty} b_w^{(0)} \delta_j^w$ where $b_w^{(0)} = \psi^w / w!$. The Maclaurin series expansion has been used to represent $e^{\delta_j \psi}$, and in practice this series would be truncated. In many error probability calculations for BPSK systems, $\psi = 0$ and $P_2^{(0)}(\delta_j) = 1$; thus the final solution will be exact. In contrast, when $\psi \neq 0$, in either error or erasure flagging situations, $P_2^{(0)}(\delta_j) = \sum_{w=0}^{W} b_w^{(0)} \delta_j^w$, and the final solution can be very precise, but not exact as the Maclaurin series expansion must be truncated at some W.

Since $B_j - B_0$ contains the form $P_1(\delta_0) P_2^{(0)}(\delta_j) - P_1(\delta_j) P_2^{(0)}(\delta_0) = (\delta_j - \delta_0) P_{12}^{(0)}(\delta_0, \delta_j)$, $\delta_j - \delta_0$ can be factored from $h^{(0)}_{N_R j} - h^{(0)}_{N_R 0}$ by using (A.15). Once $\delta_j - \delta_0$ has been factored out of $h^{(0)}_{N_R j} - h^{(0)}_{N_R 0}$, $h^{(1)}_{N_R j} = q^{(0)}_{N_R j}$, and δ_0 may be replaced with its numerical value, thus reducing the dimensionality of the problem by 1.

In the algorithm's second iteration, we wish to factor $\delta_j - \delta_1$ from $h^{(1)}_{N_R j} - h^{(1)}_{N_R 1}$ for $2 \leq j \leq N_R$. The polynomial, $P_2^{(0)}(\delta_j)$, is replaced with $P_2^{(1)}(\delta_j) = P_{12}^{(0)}(\delta_0, \delta_j)\Big|_{\delta_0}$, and $P_1(\delta_1) = \prod_{k=0}^{N_L+1} (p_r - p_{l_k} + \delta_1) = \sum_{w=0}^{N_L+1} a_w \delta_1^w$ similar to $P_1(\delta_0)$ above.

$$h^{(1)}_{N_R j} - h^{(1)}_{N_R 1} = \prod_{\substack{m=2 \\ m \neq j}}^{N_R} \prod_{k=0}^{N_L+1} (p_r - p_{l_k} + \delta_m) \left\{ P_1(\delta_1) P_2^{(1)}(\delta_j) - P_1(\delta_j) P_2^{(1)}(\delta_1) \right\}. \tag{A.17}$$

Since $h^{(1)}_{N_R j} - h^{(1)}_{N_R 1}$ contains the form $P_1(\delta_1) P_2^{(1)}(\delta_j) - P_1(\delta_j) P_2^{(1)}(\delta_1)$, $(\delta_j - \delta_1)$ can be factored from $h^{(1)}_{N_R j} - h^{(1)}_{N_R 1}$ by using (A.15) again. This procedure is continued, reducing the dimensionality of the problem by 1 with each iteration. Once the iterations are complete,

the determinant of $\mathbf{H}^{(N_R)}$ can be evaluated as $\det(\mathbf{H}^{(N_R)}) = h_{N_R N_R}^{(N_R)}\Big|_{\delta_{N_R}}$ and substituted into (A.14) to obtain the final result. The entire procedure requires N_R iterations to invert a characteristic function with $N_R + 1$ right plane poles.

A.3 Implementation

In (A.14), $\det(\mathbf{H})$ is multiplied by $-Ae^{p_r\psi}$ and divided by G to determine the cumulative pdf of the random variable, f. However, G can become large with very high orders of diversity. Therefore, to ensure the numerical stability of this algorithm, $P_1(\delta_i)$ and $P_2^{(i)}(\delta_j)$ are redefined from the above section in order to perform the division in stages with each iteration. The term, $-Ae^{p_r\psi}$, is also included into $P_2^{(0)}(\delta_j)$ in order to eliminate the need for this multiplication after the final iteration. $P_1^{(i)}(\delta_i)$ and $P_2^{(0)}(\delta_j)$ are now defined as follows:

$$P_1^{(i)}(\delta_i) = \prod_{k=0}^{N_L+1} \left(p_r - p_{l_k} + \delta_i\right) / \left(p_{r_i} - p_{l_k}\right) = \sum_{w=0}^{N_L+1} a_w^{(i)} \delta_i^w \tag{A.18}$$

$$P_2^{(0)}(\delta_j) = \frac{-Ae^{p_r\psi}}{\prod_{k=0}^{N_L+1}\left(p_{r_{N_R}} - p_{l_k}\right)} e^{\delta_j\psi} = \sum_{w=0}^{L_b^{(0)}} b_w^{(0)} \delta_j^w \tag{A.19}$$

where $e^{\delta_j\psi}$ is expanded using the Maclaurin series, and it is truncated at $L_b^{(0)}$ terms.

Even though $P_1^{(i)}(\delta_i)$ and $P_2^{(0)}(\delta_j)$ are shown as polynomials, this algorithm can be executed numerically, and a symbolic processor is not required. The algorithm could be implemented directly using (A.15). However, it is possible to implement it in a much faster way by observing patterns in the creation of $P_{12}^{(i)}(\delta_i, \delta_j)\Big|_{\delta_i}$. In order to create $P_{12}^{(i)}(\delta_i, \delta_j)\Big|_{\delta_i}$, $(\delta_j - \delta_i)$ is factored from

$$\begin{aligned} &P_1^{(i)}(\delta_i) P_2^{(i)}(\delta_j) - P_1^{(i)}(\delta_j) P_2^{(i)}(\delta_i) = \\ &\left(a_o^{(i)} + a_1^{(i)}\delta_i + \cdots a_{L_x^{(i)}}\delta_i^{L_x^{(i)}}\right)\left(b_o^{(i)} + b_1^{(i)}\delta_j + \cdots b_{L_x^{(i)}}\delta_j^{L_x^{(i)}}\right) - \\ &\left(a_o^{(i)} + a_1^{(i)}\delta_j + \cdots a_{L_x^{(i)}}\delta_j^{L_x^{(i)}}\right)\left(b_o^{(i)} + b_1^{(i)}\delta_i + \cdots b_{L_x^{(i)}}\delta_i^{L_x^{(i)}}\right) \end{aligned} \tag{A.20}$$

where $L_x^{(i)} = \max(L_b^{(i)}, N_L + 1)$. The coefficients of the polynomial, $P_1^{(i)}(\delta_i)$, in (A.18) are given by $a_w^{(i)}$, and $a_w^{(i)} = 0$ for $N_L + 2 \le w \le L_x^{(i)}$. Similarly, the coefficients of the

polynomial, $P_2^{(i)}(\delta_j)$, are given by $b_w^{(i)}$, and $b_w^{(i)} = 0$ for $L_b^{(i)} + 1 \leq w \leq L_x^{(i)}$. By multiplying and subtracting the polynomials in (A.20), it can be observed that (A.20) can be rewritten as

$$P_1^{(i)}(\delta_i) P_2^{(i)}(\delta_j) - P_1^{(i)}(\delta_j) P_2^{(i)}(\delta_i) = \sum_{n=0}^{L_x^{(i)}} \sum_{m=0}^{L_x^{(i)}} a_m^{(i)} b_n^{(i)} \left(\delta_j^n \delta_i^m - \delta_i^n \delta_j^m\right). \tag{A.21}$$

By using (A.15) to factor $(\delta_j - \delta_i)$ from $P_1^{(i)}(\delta_i) P_2^{(i)}(\delta_j) - P_1^{(i)}(\delta_j) P_2^{(i)}(\delta_i)$, $P_{12}^{(i)}(\delta_i, \delta_j)$ is given as

$$P_{12}^{(i)}(\delta_i, \delta_j) = \sum_{n=0}^{L_x^{(i)}} \sum_{m=0}^{n-1} a_m^{(i)} b_n^{(i)} \left[\delta_i^m \delta_j^{n-1} + \delta_i^{m+1} \delta_j^{n-2} + \cdots \delta_i^{n-1} \delta_j^m\right] - \sum_{n=0}^{L_x^{(i)}} \sum_{m=n+1}^{L_x^{(i)}} a_m^{(i)} b_n^{(i)} \left[\delta_i^n \delta_j^{m-1} + \delta_i^{n+1} \delta_j^{m-2} + \cdots \delta_i^{m-1} \delta_j^n\right] \tag{A.22}$$

Since $P_2^{(i+1)}(\delta_j) = P_{12}^{(i)}(\delta_i, \delta_j)\Big|_{\delta_i}$, (A.22) is used to find the coefficients of the polynomial, $P_2^{(i+1)}(\delta_j)$. From (A.22) it can be observed that the coefficient for $\delta_j^{L_x^{(i)}-k-1}$ in $P_2^{(i+1)}(\delta_j)$ is

$$b_{L_x^{(i)}-k-1}^{(i+1)} = \sum_{n=L_x^{(i)}-k}^{L_x^{(i)}} \sum_{m=0}^{n-1} a_m^{(i)} b_n^{(i)} \delta_i^{m+n+k-L_x^{(i)}} - \sum_{m=L_x^{(i)}-k}^{L_x^{(i)}} \sum_{n=0}^{m-1} a_m^{(i)} b_n^{(i)} \delta_i^{m+n+k-L_x^{(i)}} \tag{A.23}$$

The expression in (A.23) can be simplified by defining the following vectors:

$$\mathbf{a}_{l_k}^{(i)} = \left[a_0^{(i)} \delta_i^0, ..., a_{L_x^{(i)}-k-1}^{(i)} \delta_i^{L_x^{(i)}-k-1}\right]^{\mathrm{T}} \tag{A.24}$$

$$\mathbf{b}_{l_k}^{(i)} = \left[b_0^{(i)} \delta_i^0, ..., b_{L_x^{(i)}-k-1}^{(i)} \delta_i^{L_x^{(i)}-k-1}\right]^{\mathrm{T}} \tag{A.25}$$

$$\mathbf{a}_{u_k}^{(i)} = \left[a_{L_x^{(i)}-k}^{(i)} \delta_i^0, ..., a_{L_x^{(i)}}^{(i)} \delta_i^k\right]^{\mathrm{T}} \tag{A.26}$$

and

$$\mathbf{b}_{u_k}^{(i)} = \left[b_{L_x^{(i)}-k}^{(i)} \delta_i^0, ..., b_{L_x^{(i)}}^{(i)} \delta_i^k \right]^{\mathrm{T}} \tag{A.27}$$

where numerical values are used for δ_i, and the subscripts, l and u, denote lower and upper respectively. Using the above vectors, (A.23) can be rewritten, and the coefficients of $P_2^{(i+1)}(\delta_j)$, $b_w^{(i+1)}$, are calculated as follows:

$$b_{L_x^{(i)}-k-1}^{(i+1)} = \sum_{elements} \left(\mathbf{a}_{l_k}^{(i)} \mathbf{b}_{u_k}^{(i)\mathrm{T}} - \mathbf{b}_{l_k}^{(i)} \mathbf{a}_{u_k}^{(i)\mathrm{T}} \right) \tag{A.28}$$

where $0 \leq k \leq L_x^{(i)} - 1$ and $0 \leq i \leq N_R - 1$. The summation in (A.28) denotes a summation over all of the elements in the resulting matrix. In the final iteration, $i = N_R - 1$, and $b_w^{(N_R)}$ are the coefficients of $P_2^{(N_R)}(\delta_{N_R})$. The cumulative pdf of the random variable, f, is then simply given by $P(f < \psi) = P_2^{(N_R)}(\delta_{N_R})\Big|_{\delta_{N_R}}$.

To conclude, (A.28) provides a simple and efficient way for calculating error and erasure rates when the detection scheme can be expressed as a quadratic form in zero-mean complex Gaussian random variables. This method is very general in the sense that it is capable of inverting a characteristic function which consists of both multiple and simple poles. The characteristic function is inverted without resorting to a numerical integral, and the tedious task of differentiating by hand is avoided.

Appendix B

Characteristic Function Inversion in MATLAB

```
function [cdf] = InvCharacteristic(poles,thr,eps)

    % Description: InvCharacteristic(poles,thr,eps) inverts a general
    %              characteristic function which consists of both simple
    %              and multiple poles.
    %
    % Inputs: poles - A vector containing all poles of the characteristic
    %                 function including both left plane and right plane
    %                 poles. If the cdf of the decision variable is required,
    %                 the pole at zero should be included in the vector.
    %         thr   - The threshold such that the cdf of the decision variable,
    %                 f, is given by P(f<thr).
    %         eps   - This gives the accuracy of an exponential which is represented
    %                 using the Maclaurin series expansion. If eps = [ ], the default
    %                 value of 1e-4 is used. Note that when thr = 0, eps is not used
    %                 in the calculations, and the solution is exact.
    % Outputs: cdf - The is the numerical result for P(f<thr)

    pl=poles(find(poles<=0)); % Left plane (LP) poles
    pr=poles(find(poles>0)); % Right plane (RP) poles
```

```
A = prod(poles(find(poles))); % The multiplication factor.

% If thr>0, the LP and RP poles are swapped since the residues will be
% calculated over the LP poles.
if thr>0
    t=pl;
    pl=pr;
    pr=t;
end
pr=sort(pr);

% If eps = [ ], use the default value of 1e-4
if isempty(eps) == 1
   eps=1e-4;
end

nRPpoles = length(pr); % The number of RP poles
nLPpoles = length(pl); % The number of LP poles

% The RP poles are represented as pr(i) = porg + pdiff(i)
porg=0;
pdiff = pr - porg;

% P1 represents polynomial #1;
P1=1;
for c1=1:nLPpoles
   P1 = conv(P1,[porg-pl(c1),1]);
end
LP1=length(P1); % Length of polynomial #1

% The Maclaurin series expansion is used to create P2, polynomial #2.
% Note that exp(+j) converges faster than exp(-j). Therefore, if
% thr < 0, q is used to shift the exponential so that the
% Maclaurin series expansion is used to represent exp(thr*pdiff(i)+q)
% instead of exp(thr*pdiff(i)). This shift is reversed when P2 is later
```

```
% multiplied by exp(-q).
if thr < 0
   q=abs(max(abs(pdiff))*thr);
else
   q = 0;
end

w=1;
P2=1;
LP2=1;
Ptmp=1;
[th_cmp,thi]=max(q+thr.*pdiff);
if thr~=0
   while ((abs(1 - sum(P2.*pdiff(thi).^[0:LP2-1])/exp(th_cmp)) > eps) | ...
            (w<LP1) | (w<nRPpoles))
      Ptmp = conv(Ptmp,[q/thr,1]);
      P2 = [P2,0] + thr^w/prod(1:w).*Ptmp;
      LP2 = length(P2);
      w=w+1;
   end
end

% Normalize polynomial #2 to ensure numerical stability and reverse
% the shift of exp(q);
P2 = A*prod(1./(pr(nRPpoles)-pl))*exp(porg*thr-q).*P2;

LP2=length(P2); % Length of polynomial #2

% LP is the maximum length of polynomials #1 or #2. The length,
% LP, must be at least nRPpoles since the procedure requires nRPpoles-1
% iterations to invert a characteristic function with nRPpoles RP poles.
LP = max(max(LP1,LP2),nRPpoles);

for cnt=2:length(pdiff)
   % Normalize polynomial #1 to ensure numerical stability.
```

```
    P1t=P1./prod(pr(cnt-1)-pl);

     % Extend polynomials #1 and #2 by the required amount.
    P1t=[P1t,zeros(1,LP-LP1)];
    P2t=[P2,zeros(1,LP-LP2)];

    % The multiplicative factors for the upper and lower vectors.
    Pdt = pdiff(cnt-1).^[0:LP-1];

     % The vector, P3, contains the coefficients for P2 in the following
    % iteration. This uses the upper and lower vectors of P1t and P2t.
    P3=zeros(1,LP-1);
    for c1=LP-1:-1:1
        P3(c1) = sum(sum((((P1t(1:c1).*Pdt(1:c1)).')* ...
                    (P2t(c1+1:LP).*Pdt(1:LP-c1))- ...
                    ((P2t(1:c1).*Pdt(1:c1)).')* ...
                     (P1t(c1+1:LP).*Pdt(1:LP-c1)))));
    end

    P2=P3;
    LP2=length(P2);
    LP = max(LP1,LP2);
end

% The numerical result for P(f<thr)
cdf = abs(sum(P2.*pdiff(length(pdiff)).^[0:LP2-1]));
```

Bibliography

[1] K. S. Gilhousen, et al. "On the capacity of a cellular CDMA system," *IEEE Trans. on Vehicular Technology*, vol. 40, no. 2, pp. 303-312, May 1991.

[2] S. Verdu, "Minimum probability of error for asynchronous Gaussian multiple-access channels," *IEEE Trans. on Information Theory*, vol. IT-32, no. 1, pp. 85-96, Jan. 1986.

[3] J. K. Cavers, *Mobile Channel Characteristics*. Hingham, MA: Kluwer Academic Publishers, 2000.

[4] K. S. Butterworth, "Performance, planning and deployment of DS-CDMA in-building wireless communication systems," Ph.D. Thesis, University of Auckland, March 2000.

[5] K. S. Butterworth, K. W. Sowerby, and A. G. Williamson, "Influence of correlated shadowing on the system capacity of a DS-CDMA in-building wireless communication system," *Proc. Virginia Tech MPRG Symposium on Wireless Personal Communications*, Blacksburg, Virginia, pp. 41-52, June 1997.

[6] A. A. M. Saleh and R. A. Valenzuela, "A statistical model for indoor multipath propagation," *IEEE Journal on Selected Areas in Communications*, vol. SAC-5, no. 2, pp. 128-137, Feb. 1987.

[7] Q. Spencer, M. Rice, B. Jeffs, and M. Jensen, "Indoor wideband time/angle of arrival multipath propagation results," *Proceedings of VTC'97*, Phoenix, USA, pp. 1410-1414, May 1997.

[8] Q. Spencer, M. Rice, B. Jeffs, and M. Jensen, "A statistical model for angle of arrival in indoor multipath propagation," *Proceedings of VTC'97*, Phoenix, USA, pp. 1415-1419, May 1997.

[9] K. S. Butterworth, K. W. Sowerby, and A. G. Williamson, "Influence of correlated shadowing and base station configuration on in-building system capacity," *Proceedings of VTC'98*, Ottawa, Canada, pp. 850-854, May 1998.

[10] A. J. Viterbi, *Principles of Spread Spectrum Communication*. New York: Addison-Wesley Publishing Company, 1995.

[11] P. T. Brady, "A statistical analysis of on-off patterns in 16 conversations," *Bell Syst. Tech. J.* Vol. 47, pp. 73-91, Jan. 1968.

[12] M. B. Pursley and H. F. A. Roefs, "Numerical evaluation of correlation parameters for optimal phases of binary shift-register sequences," *IEEE Trans. on Communications*, vol. COM-27, no. 10, pp. 1597-1604, Oct. 1979.

[13] The CDMA Development Group, "About CDMA Technology," [http://www.cdg.org/tech/a_ross/].

[14] W. C. Y. Lee, *Mobile Communications Engineering*. New York: McGraw-Hill, 1982.

[15] J. G. Proakis, *Digital Communications*. Second Edition, New York: McGraw-Hill Book Company, 1989.

[16] J. H. Winters, "Optimum combining in digital mobile radio with cochannel interference," *IEEE Journal on Selected Areas in Communications*, vol. SAC-2, no. 4, pp. 528-539, July 1984.

[17] R. A. Monzingo and T. W. Miller, *Introduction to Adaptive Arrays*, New York: Wiley, 1980.

[18] S. J. Grant and J. K. Cavers, "Performance enhancement through joint detection of cochannel signals using diversity arrays," *IEEE Trans. on Communications*, vol. 46, pp. 1038-1049, August 1998.

[19] J. H. Winters, J. Salz, and R. D. Gitlin, "The impact of antenna diversity on the capacity of wireless communication systems," *IEEE Trans. on Communications*, vol. 42, no. 2/3/4, pp. 1740-1751, Feb./Mar./Apr. 1994.

[20] J. Salz, and J. H. Winters, "Effect of fading correlation on adaptive arrays in digital mobile radio," *IEEE Trans. on Vehicular Technology*, vol. 43, no. 4 pp. 1049-1057, Nov. 1994.

[21] C. C. Lee and R. Steele, "Effect of soft and softer handoffs on CDMA system capacity," *IEEE Trans. on Vehicular Technology*, vol. 47, no. 3, pp. 830-841, Aug. 1998.

[22] A. Salmasi and K. S. Gilhousen, "On the system design aspects of code division multiple access (CDMA) applied to digital cellular and personal communications networks," *Proceedings of VTC'91*, St. Louis, USA, pp. 57-62, May 1991.

[23] A. J. Viterbi, A. M. Viterbi, K. S. Gilhousen, and E. Zehavi, "Soft handoff extends CDMA cell coverage and increases reverse link capacity," *IEEE Journal on Selected Areas in Communications*, vol. 12, no. 8, pp. 1281-1288, Oct. 1994.

[24] Z. J. Haas and C. P. Li, "The multiply-detected macrodiversity scheme for wireless cellular systems," *IEEE Trans. on Vehicular Technology*, vol. 47, no. 2, pp. 506-530, May 1998.

[25] S. V. Hanly, "Capacity and power control in spread spectrum macrodiversity radio networks," *IEEE Trans. on Communications*, vol. 44, no. 2, pp. 247-256, Feb. 1996.

[26] J. L. Gorricho and J. Paradells, "Evaluation of the soft handover benefits on CDMA systems," *Proceedings of ICUPC'96*, Cambridge, MA, vol. 1, pp. 305-309, Sept. 29 - Oct. 2, 1996.

[27] R. Stuetzle and A. Paulraj, "Modeling of forward link performance in IS-95 CDMA networks," *Proceedings of ISSSTA'95*, Mainz, Germany, vol. 3, pp. 1058-1062, Sept. 22-25, 1996.

[28] A. Daraiseh and M. Landolsi, "Optimized CDMA forward link power allocation during soft handoff," *Proceedings of VTC'98*, Ottawa, Canada, pp. 1548-1552, May 1998.

[29] T. Heikkinen and A. Hottinen, "On downlink power control and capacity with multi-antenna transmission," *Proceedings of VTC'98*, Ottawa, Canada, pp. 475-479, May 1998.

[30] R. Lupas and S. Verdu, "Near-far resistance of multiuser detectors in asynchronous channels," *IEEE Trans. on Communications*, vol. 38, no. 4, pp. 496-508, April 1990.

[31] Z. Xie, R. T. Short, and C. K. Rushforth, "A family of suboptimum detectors for coherent multiuser communications," *IEEE Journal on Selected Areas in Communications*, vol. 8, no. 4, pp. 683-690, May 1990.

[32] U. Madhow and M. L. Honig, "MMSE interference suppression for direct-sequence spread-spectrum CDMA," *IEEE Trans. on Communications*, vol. 42, no. 12, pp. 3178-3188, Dec. 1994.

[33] M. J. Juntti and B. Aazhang, "Finite memory-length linear multiuser detection for asynchronous CDMA communications," *IEEE Trans. on Communications*, vol. 45, no. 5, pp. 611-622, May 1997.

[34] Z. Zvonar and D. Brady, "Multiuser detection in single-path fading channels," *IEEE Trans. on Communications*, vol. 42, no. 2/3/4, pp. 1729-1739, Feb./Mar./April 1994.

[35] Z. Zvonar, "Combined multiuser detection and diversity reception for wireless CDMA systems," *IEEE Trans. on Vehicular Technology*, vol. 45, no. 1, pp. 205-211, Feb. 1996.

[36] M. J. Juntti and J. O. Lilleberg, "Comparative analysis of conventional and multiuser detectors in multisensor receivers," *Proceedings of IEEE Military Communications Conference (MILCOM'97)*, Monterey, CA, pp. 318-323, 1997.

[37] J. Lilleberg and W. Haifeng, "Multiuser receiver with multiple sensors in asynchronous CDMA systems," *Proceedings of Wireless Communications and Networking Conference (WCNC'99),* New Orleans, LA, vol. 3, pp. 1475-1478, Sept. 1999.

[38] S. Ulukus and R. D. Yates, "Adaptive power control with MMSE multiuser detectors," *Proceedings of ICC'97*, Montreal, Quebec, Canada, pp. 361-365, June 1997.

[39] A. Yener, R. D. Yates, and S. Ulukus, "Joint power control, multiuser detection and beamforming for CDMA systems," *Proceedings of VTC'99*, Houston, TX, pp. 1032-1036, May 1999.

[40] M. K. Varanasi and B. Aazhang, "Multistage detection in asynchronous code-division multiple-access communications," *IEEE Trans. on Communications*, vol. 38, no. 4, pp. 509-519, April 1990.

[41] P. Patel and J. Holtzman, "Analysis of a simple successive interference cancellations scheme in a DS/CDMA system," *IEEE Journal on Selected Areas in Communications*," vol. 12, no. 5, pp. 796-807, June 1994.

[42] O. Nesper, "Pilot symbol assisted successive interference cancelling receiver for direct sequence/code division multiple access systems," M.A.Sc. Thesis, Simon Fraser University, Sept. 1996.

[43] P. Jung, B. Steiner, and B. Stilling, "Exploitation of intracell macrodiversity in mobile radio systems by deployment of remote antennas," *Proceedings of International Symposium on Spread Spectrum Techniques and Applications (ISSSTA'95)*, Mainz, Germany, vol. 1, pp. 302-307, Sept. 1995.

[44] M. C. Valenti and B. D. Woerner, "Multiuser detection with base station diversity," *Proceedings of ICUPC'98*, Florence, Italy, vol. 2, pp. 1189-1193, Oct. 1998.

[45] S. Kandala and E. S. Sousa, "Multi-user multi-sensor detectors for CDMA networks," *IEEE Trans. on Communications*, vol. 43, no. 2/3/4, pp. 946-957, Feb./Mar./April 1995.

[46] S. D. Gray, M. Kocic, and D. Brady, "Multiuser detection in mismatched multiple-access channels," *IEEE. Trans. on Communications*, vol. 43, no. 12, pp. 3080-3089, Dec. 1995.

[47] L. K. Rasmussen, S. Sum, T. J. Lim, and H. Sugimoto, "Impact of estimation errors on multiuser detection in CDMA," *Proceedings of VTC'98*, Ottawa, Canada, pp. 1844-1848, May 1998.

[48] F. Zheng and S. K. Barton, "On the performance of near-far resistant CDMA detectors in the presence of synchronization errors," *IEEE Trans. on Communications*, vol. 43, no. 12, pp. 3037-3045, Dec. 1995.

[49] S. Verdu, "Optimum multiuser asymptotic efficiency," *IEEE Trans. on Communications*, vol. COM-34, no. 9, pp. 890-897, Sept. 1986.

[50] Z. Xie, C. K. Rushforth, R. T. Short, and T. K. Moon, "Joint signal detection and parameter estimation in multiuser communications," *IEEE Trans. on Communications*, vol. 41, no. 7, pp. 1208-1215, Aug. 1993.

[51] T. K. Moon, Z. Xie, C. K. Rushforth, and R. T. Short, "Parameter estimation in a multi-user communication system," *IEEE Trans. on Communications*, vol. 42, no. 8, pp. 2553-2560, Aug. 1994.

[52] S. E. Bensley and B. Aazhang, "Subspace-based channel estimation for code division multiple access communication systems," *IEEE Trans. on Communications*, vol. 44, no. 8, pp. 1009-1020, Aug. 1996.

[53] E. G. Strom and S. Parkvall, "Joint parameter estimation and detection of DS-CDMA signals in fading channels," *Proceedings of IEEE Global Telecommunications Conference (Globecom'95)*, Singapore, pp. 1109-1113, Nov. 1995.

[54] S. E. Bensley and B. Aazhang, "Maximum-likelihood synchronization of a single user for code-division multiple-access communication systems," *IEEE Trans. on Communications*, vol. 46, no. 3, pp. 392-399, March 1998.

[55] E. G. Strom and F. Malmsten, "Maximum likelihood synchronization of DS-CDMA signals transmitted over multipath channels," *Proc. IEEE International Conference on Communications (ICC'98)*, Atlanta, Georgia, pp. 1546-1550, June 1998.

[56] C. Sengupta, A. Hottinen, J. R. Cavallaro, and B. Aazhang, "Maximum likelihood multipath channel parameter estimation in CDMA systems," *Proceedings of the Conference on Information Sciences and Systems*, Princeton, NJ, vol. 1, pp. 6-11, March 1998.

[57] E. Ertin, U. Mitra, and S. Siwamogsatham, "Maximum-likelihood based multipath channel estimation for code-division multiple-access systems," accepted for publication in *IEEE Trans. on Communications*.

[58] J. K. Cavers, "An analysis of pilot symbol assisted modulation for Rayleigh fading channels," *IEEE Trans. on Vehicular Technology*, vol. 40, no. 4, pp. 686-693, Nov. 1991.

[59] S. J. Grant and J. K. Cavers, "Multiuser channel estimation for detection of cochannel signals," *Proceedings of ICC'99*, Vancouver, Canada, June 1999.

[60] K. S. Butterworth, K. W. Sowerby, and A. G. Williamson, "Correlated shadowing in an in-building propagation environment," *Electronics Letters*, vol. 33, no. 5, pp. 420-421, Feb. 1997.

[61] J. K. Cavers and P. Ho, "Analysis of the error performance of trellis-coded modulations in Rayleigh-fading channels," *IEEE Trans. on Communications*, vol. 40, no. 1, pp. 74-83, Jan. 1992.

[62] G. D. Forney, "Maximum-likelihood sequence estimation of digital sequences in the presence of intersymbol interference," *IEEE Trans. on Information Theory*, vol. IT-18, no. 3, pp. 363-378, May 1972.

[63] J. K. Cavers, J. H. Kim, and P. Ho, "Exact calculation of the union bound on performance of trellis-coded modulation in fading channels," *IEEE Trans. on Communications*, vol. 46, no. 5, pp. 576-579, May 1998.

[64] T. H. Cormen, C. E. Leiserson, and R. L. Rivest, *Introduction to Algorithms*. New York: McGraw-Hill, 1990.

[65] R. P. Grimaldi, *Discrete and Combinatorial Mathematics, An Applied Introduction* 3rd Edition. Reading, Massachusetts, Addison-Wesley Publishing Company, 1994.

[66] S. Haykin, *Adaptive Filter Theory* 3rd Edition, Upper Saddle River, NJ: Prentice-Hall, 1996.

[67] M. Schwartz, W. Bennett, and S. Stein, *Communication Systems and Techniques*. New York: McGraw-Hill, 1966.

[68] H. H. Xia, "CDMA system design and deployment," Tutorial 3 IEEE VTC 98, Ottawa, Canada, May 18-21, 1998.

[69] Digital by QUALCOMM "Power Control," IS-95A: The cdmaOne Standard, Oct. 18, 1997.

[70] H. Hashemi, D. Tholl, G. Morrison, "Statistical modeling of the indoor radio propagation channel - Part I," *Proceedings of the Vehicular Technology Society 42nd VTS Conference*, Denver, Colorado, vol. 1, pp. 338-342, May 1992.

[71] L. Wei, L. K. Rasmussen, and R. Wyrwas, "Near optimum tree-search detection schemes for bit-synchronous multiuser CDMA systems over Gaussian and two-path Rayleigh-fading channels," *IEEE Trans. on Communications*, vol. 45, no. 6, pp. 691-700, June 1997.

[72] G. E. Moore, "Cramming more components into integrated circuits," *Electronics*, vol. 38, no. 8, pp. 114-117, April 19, 1965.

[73] L. R. Welburn and J. K. Cavers, "Pilot signals improve the performance of a Reed-Solomon errors and erasures decoder in Rayleigh fading channels" *IEEE Trans. on Communications*, vol. 47, no. 5, pp. 689-696, May 1999.

[74] B. Hagerman, K. J. Molnar, and B. D. Molnar, "Evaluation of novel multi-beam antenna configurations for TDMA (IS-136) systems," in *Proc. IEEE Veh. Tech. Conf.*, Houston, TX, May 1999.

[75] K. S. Hwang and F. C. Chang, "A numerical method for solving time-invariant system by the generalized inverse Vandermonde matrix," *Journal of Information Science and Engineering*, vol. 15, pp. 321-327, 1999.

[76] E. Kreyszig, *Advanced Engineering Mathematics*, 6th edition, New York: John Wiley, 1988.